

ABSTRACT

Title of Dissertation: A MICROFLUIDIC PROGRAMMABLE
ARRAY FOR LABEL-FREE DETECTION OF
BIOMOLECULES

Peter Hume Dykstra, Doctor of Philosophy, 2011

Directed By: Professor Reza Ghodssi, Department of
Electrical and Computer Engineering

One of the most promising ways to improve clinical diagnostic tools is to use microfluidic Lab-on-a-chip devices. Such devices can provide a dense array of fluidic components and sensors at the micro-scale which drastically reduce the necessary sample volumes and testing time. This dissertation develops a unique electrochemical sensor array in a microfluidic device for high-throughput, label-free detection of both DNA hybridization and protein adsorption experiments.

The device consists of a patterned 3 x 3 grid of electrodes which can be individually addressed and microfluidic channels molded using the elastomer PDMS. The channels are bonded over the patterned electrodes on a silicon or glass substrate. The electrodes are designed to provide a row-column addressing format to reduce the number of contact pads required and to drastically reduce the complexity involved in scaling the device to include larger arrays. The device includes straight channels of 100 μm height which can be manually rotated to provide either horizontal or vertical fluid flow over the patterned sensors. To enhance the design of the arrayed device, a

series of microvalves were integrated with the platform. This integrated system requires rounded microfluidic channels of 32 μm height and a second layer of channels which act as pneumatic valves to pinch off selected areas of the microfluidic channel. With the valves, the fluid flow direction can be controlled autonomously without moving the bonded PDMS layer. Changes to the mechanism of detection and diffusion properties of the system were examined after the integration of the microvalve network.

Protein adhesion studies of three different proteins to three functionalized surfaces were performed. The electrochemical characterization data could be used to help identify adhesion properties for surface coatings used in biomedical devices or for passivating sensor surfaces. DNA hybridization experiments were performed and confirmed both arrayed and sensitive detection. Hybridization experiments performed in the valved device demonstrated an altered diffusion regime which directly affected the detection mechanism. On average, successful hybridization yielded a signal increase 8x higher than two separate control experiments. The detection limit of the sensor was calculated to be 8 nM.

**A MICROFLUIDIC PROGRAMMABLE ARRAY FOR LABEL-FREE
DETECTION OF BIOMOLECULES**

By

Peter Hume Dykstra

Dissertation submitted to the Faculty of the Graduate School of the
University of Maryland, College Park, in partial fulfillment
of the requirements for the degree of
Doctor of Philosophy
2011

Advisory Committee:

Professor Reza Ghodssi, Chair
Professor William Bentley
Professor Gregory Payne
Professor Martin Peckerar
Professor Gary Rubloff

© Copyright by
Peter Hume Dykstra
2011

Dedication

To my wife Laura for all her love and support.

Acknowledgments

I would first and foremost like to thank my advisor, Prof. Reza Ghodssi, for all of his support and guidance over the past five years. I also thank my dissertation committee, Prof. William Bentley, Prof. Gregory Payne, Prof. Martin Peckerar and Prof. Gary Rubloff. This work would not have been possible without the gracious funding from the R. W. Deutsch Foundation and the National Science Foundation. There are many individuals who helped me greatly during the course of this research. I especially want to thank Varnika Roy for all of her time spent helping me and training me to work with the biomolecules. I also want to thank both Christopher Byrd and James Sumner from the Army Research Laboratory for their helpful and insightful discussions. I wish to thank all of my colleagues at the MEMS Sensors and Actuators Lab (MSAL) for providing both intellectual and emotional support throughout the years. I especially want to thank Mariana Meyer, Nathan Siwak and Hadar Ben-Yoav for reviewing this manuscript. I greatly appreciate the support from the members of the Fablab staff at the University of Maryland. Last but not least, I want to thank my wife, Laura, for always brightening my spirits during tough times and my family and friends for helping to carry me through.

Peter Dykstra,

July, 2011

Table of Contents

Dedication.....	ii
Acknowledgments.....	iii
Table of Contents.....	iv
List of Tables.....	vii
List of Figures.....	viii
1 Introduction.....	1
1.1 Motivation.....	1
1.2 Summary of Accomplishments.....	3
1.2.1 Fabrication and testing of an arrayed label-free sensing platform.....	3
1.2.2 Study of protein adhesion to various functionalized surfaces.....	4
1.2.3 DNA hybridization study throughout all stages of device design.....	4
1.3 Literature Review.....	5
1.3.1 Conventional drug discovery and screening techniques.....	5
1.3.2 Microfluidic sensors.....	14
1.3.3 Characterization of protein adsorption.....	21
1.3.4 Electrochemical sensors for DNA hybridization.....	23
1.4 Literature Summary.....	27
1.5 Structure of Dissertation.....	27
2 Device Operation and Design.....	29
2.1 Introduction.....	29
2.2 Interactions between biomolecules.....	29
2.2.1 Protein Adsorption.....	30
2.2.2 DNA hybridization.....	31
2.3 Device Overview.....	32
2.4 Electrochemical Detection Concept.....	34
2.4.1 The Three Electrode System.....	34
2.4.2 Detection Mechanism.....	35
2.4.3 Cyclic Voltammetry.....	37
2.4.4 Impedance Spectroscopy.....	42
2.5 Electrode Configuration and Design.....	47
2.5.1 Electrode Materials.....	47
2.5.2 Electrode Geometry and Placement.....	49
2.6 Microchannel design.....	52
2.6.1 Valved Microfluidic Channel Design.....	54
2.6.2 Pneumatic Valve Channels.....	58
2.7 Summary.....	59

3	Device Fabrication	60
3.1	Introduction	60
3.2	Chip Fabrication	60
3.2.1	Metal Patterning	61
3.2.2	SU-8 5 Patterning	66
3.3	PDMS Processing	67
3.3.1	SU-8 50 Mold Fabrication	68
3.3.2	AZ9260 Mold Fabrication	70
3.3.3	PDMS processing parameters	74
3.4	Bonding and Packaging	78
3.4.1	Plasma Bonding Procedure	78
3.4.2	Fluidic connections	81
3.5	Summary	82
4	Testing and Characterization	84
4.1	Introduction	84
4.2	Preliminary Electrochemical Tests	84
4.2.1	Beaker Experiments	84
4.2.2	Droplet Testing	85
4.3	Microfluidic Device Testing	87
4.3.1	Testing and Operation	88
4.3.2	Sensor Uniformity	89
4.3.3	Sensor Cleanliness	90
4.4	Valved Microfluidic Device	91
4.4.1	Testing and Operation	92
4.4.2	Pneumatic vs. Hydraulic Actuation	93
4.4.3	Sensor Uniformity	94
4.4.4	Sensor cleanliness	96
4.4.5	Diffusion Limitation of Valve Integration	97
4.5	Summary	100
5	Protein Adsorption Study	101
5.1	Introduction	101
5.2	Materials Used	101
5.3	Surface Preparation	104
5.4	Protein Adsorption Data	105
5.4.1	Adsorption to MCH	105
5.4.2	Adsorption to BSA	106
5.4.3	Adsorption to PEG	107
5.5	Data Discussion	108
5.6	Sensor Reusability	115
5.7	Summary	116
6	DNA Hybridization Study	117
6.1	Introduction	117
6.2	DNA Sequences and Buffers	117

6.3	Hybridization Testing Procedure	119
6.3.1	DNA probe immobilization	119
6.3.2	MCH backfilling	122
6.3.3	Hybridization Reaction	123
6.4	Macroscale DNA Hybridization Results	126
6.5	Microfluidic DNA Hybridization Results	130
6.5.1	Non-valved Microfluidic Device	130
6.5.2	Valved Microfluidic Device	135
6.6	Summary	139
7	Conclusion	141
7.1	Summary	141
7.1.1	Protein Adhesion Study	142
7.1.2	DNA Hybridization Study	143
7.2	Future Work	144
7.2.1	Microfluidic Design Improvements	144
7.2.2	Use of Chitosan	148
7.2.3	Other Assays and Studies	149
7.3	Conclusion	152
	Appendix A	153
	Appendix B	155
	References	166

List of Tables

Table 2.1: List of commonly used aqueous reference electrodes and their potential vs. the standard hydrogen electrode at room temperature.	48
Table 3.1: Process flow of metal patterning steps for all design stages.	61
Table 3.2: Parameters used for sputtering Cr/Au onto the wafer.	63
Table 3.3: Table of processing steps and parameters for patterning the Cr/Au electrodes.	63
Table 3.4: Processing parameters for AZ5214 photoresist.	65
Table 3.5: Processing parameters for SU-8 5.	66
Table 3.6: Processing parameters used for SU-8 50 on silicon.	69
Table 3.7: Processing parameters for AZ9260 lithography and rounding.	71
Table 3.8: Bond strength of PDMS to silicon dioxide for various RIE machine parameters.	80
Table 5.1: Values for the charge transfer resistance (R_{ct}) and double layer capacitance (C_d) for each protein and surface investigated. Values are extracted from the impedance data displayed in Figures 5.2 – 5.4.	109

List of Figures

Figure 1.1: (a) photograph of a typical 96 well plate and (b) a more dense 1536 well plate. Images reproduced from [46].	6
Figure 1.2: Design of the coupling of the microdevice with attached CE and MS components to the vertically mounted microwell plate. Reproduced from [49].	8
Figure 1.3: Results from DNA tagged with a radioactive label migrating through an acrylic gel with various protein concentrations added to each lane (in nM). The arrow indicates the band which corresponds to the shift of DNA with no bound protein. Reproduced from [61].	10
Figure 1.4: Schematic displaying how flow cytometry works. The scattering of the laser light coupled with the fluorescence emission provide data for each cell passing through the beam. Reproduced from [69].	12
Figure 1.5: Schematic of the portable flow cytometry and impedance detection system. A DC voltage is applied across the microfluidic channel while fluorescence detection is performed using free space optics positioned beneath the channel. Reproduced from [71].	13
Figure 1.6: Schematic of SPR microfluidic device. The incorporation of so many components in a small footprint demonstrate an advantage leveraged by microfluidic design. Reproduced from [81].	16
Figure 1.7: Device schematic and photograph demonstrating the packaging of a microfluidic channel over a SAW sensing chip. Reproduced from [89].	18
Figure 1.8: Photograph and schematic of microfluidic device containing integrated electrodes for both sensing and fluid control. Reproduced from [99].	19
Figure 1.9: Photograph of microfluidic device for DNA hybridization. The main chamber has three sensing electrodes (S1-3), one reference electrode (R) and one counter electrode (C). Reproduced from [30].	26
Figure 2.1: Structure of the thiol modification conjugated to the 5' end of the ssDNA.	32
Figure 2.2: (a) The PDMS channels are aligned to expose columns of working electrodes to be functionalized by different compounds. (b) After functionalization, the PDMS channels are lifted, rotated, and placed back down to align counter and reference electrodes within separate rows of working electrodes.	33
Figure 2.3: Structure for the ferri/ferrocyanide redox couple.	35

Figure 2.4: Schematic demonstrating the increased negative charge due to DNA hybridization on the electrode surface. A decrease in the measured current results from further repulsion of the charged redox compound.	37
Figure 2.5: Example of a cyclic voltammogram taken on a bare gold electrode surface.	38
Figure 2.6: MATLAB simulation of CV results for an electrode surface covered with ssDNA and dsDNA.	41
Figure 2.7: Randles equivalent circuit model for the complex impedance of the three electrode system in an ionic solution.	43
Figure 2.8: EIS simulations performed by varying the charge transfer resistance (R_{ct}).	45
Figure 2.9: Simulated EIS results from a varying double layer capacitance (C).	46
Figure 2.10: Circuit model for the current flow between the working and counter electrodes.	50
Figure 2.11: Top-down schematic of the electrode configuration in the microfluidic device containing 9 total sensors. The blue areas correspond to bonded PDMS with the substrate. Both channel orientations are overlaid to show both vertical and horizontal paths.	51
Figure 2.12: Schematic demonstrating valve actuation using pneumatic channel to pinch off the microfluidic channel below.	53
Figure 2.13: Overhead layout of microfluidic channels (blue) and pneumatic valve channels (green). In (a) pressure is applied to the top valve inlet and valves are closed to create vertical fluid channels. In (b) the pressure is applied to the bottom inlet and three horizontal fluid channels are created.	53
Figure 2.14: Geometry used for calculating the area of the rounded microfluidic channels.	55
Figure 2.15: Microscope images showing channel alignment over the patterned electrodes. Both good alignment (a) and bad alignment (b) were observed in the same device. The new channel cross section design is shown in (c) to provide more alignment tolerance. All scale bars are 100 μm	56
Figure 2.16: Fluid flow through the older (a) and updated (b) microfluidic channel design when using valves. The liquid-air interface is moved further away from the electrode in (b) which reduces problems with evaporation.	57

Figure 3.1: Photograph of patterned macroscale chips. Left two chips are counter electrodes while right two are working electrodes.	64
Figure 3.2: Photographs of completed chips for the microfluidic design without valves on silicon dioxide (a), and the design with valves on both silicon dioxide (b) and glass (c).	66
Figure 3.3: Photograph of chips used for droplet tests.	67
Figure 3.4: Microscope image of droplet sensor chip containing 4 working electrodes, 1 counter electrode and 1 reference electrode patterned within a ring of SU-8.	67
Figure 3.5: Completed SU-8 molds for (a) straight microfluidic channels and (b) valve channel network.	69
Figure 3.6: (a) microscope images and (b) profilometer scans of AZ9260 photoresist before and after the rounding procedure. Notice the increase in height of the resist from 23.6 μm to 32.8 μm after rounding.	72
Figure 3.7: Photograph of the completed AZ9260 mold wafer.	74
Figure 3.8: PDMS thickness vs. spin speed curve. Speeds higher than 1500 RPM display little change to the thickness.	75
Figure 3.9: Dual layer PDMS fabrication process including a spun layer to form microfluidic channels (a) and a thicker layer to form valve channels (b). The thicker layer is cut into smaller portions and aligned over the spun PDMS as shown in (c). After curing together, the entire stack is cut out and peeled away from the mold as shown in (d).	77
Figure 3.10: Photograph of the two layers of PDMS bonded to one another over the AZ9260 mold wafer. Individual pieces from the top valve layer are aligned over the fluidic channel network. The entire stack is bonded by placing it back into the box furnace.	77
Figure 3.11: Photograph of completed valved microfluidic device containing microfluidic network (green) and valve channel networks (red, blue).	81
Figure 3.12: Plastic connectors used to interface tubing with the microfluidic device. Two sizes of tubing are used to create a leak-proof seal.	82
Figure 4.1: Photograph of testing set-up used for all beaker experiments.	85
Figure 4.2: Photograph of droplet chip under test. A droplet of electroactive solution is placed over the electrodes in the center of the chip.	86

Figure 4.3: CV scans using the droplet chip of two electrodes on different days. The redox peaks occur at nearly the same value which demonstrates the stable nature of platinum as a reference electrode.....	86
Figure 4.4: Repeated scans of same electrode using droplet sensor. Increasing current attributed to constant evaporation of the droplet.	87
Figure 4.5: Photograph of the microfluidic device design without valves under test.	88
Figure 4.6: Cyclic voltammetry plots from the nine sensors in the microfluidic device arranged in a 3 x 3 grid. The peak heights and peak separation are all very similar for each plot demonstrating excellent reproducibility among the patterned sensors.	90
Figure 4.7: Cyclic voltammograms with increasing scan rates from 25 – 800 mV/sec. (inset) Linear relationship observed between the reduction current peak amplitude and the square root of the scan rate.	91
Figure 4.8: Photograph of testing set-up utilized for the valved microfluidic device.	92
Figure 4.9: (a) vertical channels created in device by applying pressure to top inlet and (b) horizontal channels created by applying pressure to the bottom right inlet. ..	93
Figure 4.10: CV scans for each of the nine clean working electrodes in the valved microfluidic device. The graphs are displayed in the same 3 x 3 grid as the physical sensor layout.	95
Figure 4.11: CV scans of an electrode in the valved microfluidic system at increasing scan rates. The inset graph displays the linear correlation between the peak amplitude and the square root of the scan rate.....	96
Figure 4.12: Total charge passed through sensor for both the non-valved and valved design. The valved device takes longer to form the diffusion gradient.	98
Figure 5.1: Gel shift assay confirming CRP activity. Only lanes 7 and 8 display shifting due to the binding of the CRP to the DNA sequence in the presence of cAMP.	104
Figure 5.2: Impedance spectroscopy data for electrodes passivated with MCH followed by incubation for 15 minutes with (a) TNF α , (b) TNF β and (c) CRP.....	106
Figure 5.3: Impedance spectroscopy data for electrodes passivated with BSA followed by incubation for 15 minutes with (a) TNF α , (b) TNF β and (c) CRP.....	107
Figure 5.4: Impedance spectroscopy data for electrodes passivated with PEG followed by incubation for 15 minutes with (a) TNF α , (b) TNF β and (c) CRP.....	108

Figure 5.5: Percent change in R_{ct} for adsorption of each protein to both MCH and BSA. Clear trends can be determined including the large impedance increase for TNF α on MCH and impedance decrease for CRP on MCH. All three proteins display roughly the same impedance change for a surface coated with BSA. Error bars designate one standard deviation, $n = 3$ 110

Figure 5.6: Modification of the Randles circuit to more closely model the collected impedance data. The same solution resistance (R_s), double layer capacitance (C_d) and Warburg impedance (W) from Figure 2.7 are used, but the resistance contribution from R_{ct} has now been split amongst R_1 and R_2 113

Figure 5.7: Impedance spectra for an electrode passivated with BSA including the fitted curve for two circuit models. The solid line displays the fit using the Randles circuit from Scheme 1 while the dotted line displays the fit using the improved circuit from Scheme 2. The improved fit results in a 4x reduction of the fitting error. 114

Figure 5.8: Cyclic voltammetry measurements of a blank electrode (solid), the response after incubation with PEG (dotted), and the final response after applying a high switching potential (0.8 to -0.8 volts) to the electrode (dashed)..... 115

Figure 6.1: Surface density and separation of thiol-DNA probe molecules for a given concentration during incubation over a gold electrode for 1 hour. Reproduced from [139]. 120

Figure 6.2: EIS results of a blank macroscale electrode (●) after either adsorbed DNA (○) or thiol-terminated DNA (▲). 121

Figure 6.3: Fluorescent microscope image of TEX615-labeled DNA assembled on gold electrodes outlined in white. 124

Figure 6.4: (a) CV results and (b) EIS data for a blank electrode (●), after ssDNA probe and MCH immobilization (○), after incubation with a non-matching sequence (▲) and after incubation with a matching sequence (△). The binding event is more clearly observed using EIS. 127

Figure 6.5: EIS data for three electrodes immobilized with (a) ssDNA1_T, (b) ssDNA2_T and (c) ssDNA3_T. Each sensor is incubated in both mis-matching sequences and the final matching sequence. 128

Figure 6.6: Bar graph displaying % change in R_{ct} following each target DNA incubation for each probe sequence. Hybridization events are clearly observed for matching target-probe sequences. 129

Figure 6.7: EIS plots for each electrode surface before (●) and after (▲) incubation with the target ssDNA sequence. Each column of sensors is immobilized with a

different probe sequence while each row is incubated with a different target ssDNA sequence..... 131

Figure 6.8: Bar graph showing % change in R_{ct} after incubation with each target ssDNA sequence for each probe sequence. 132

Figure 6.9: EIS data of a single working electrode in the non-valved microfluidic device. Incubation with increasing concentrations of the complementary target ssDNA causes increasing impedance until saturation at 10 μ M..... 133

Figure 6.10: (a) Values of charge transfer resistance for each concentration which includes a zero concentration data point corresponding to incubation with a non-complementary target. (b) Logarithmic dependence of the charge transfer resistance on the target concentration observed via high linear correlation on the log scale.... 134

Figure 6.11: (a) EIS data displaying three scans each for two non-matching DNA incubations and the matching DNA incubation. The lowest frequency points are highlighted. (b) The percent change in the fitted R_{ct} value after each incubation. ... 135

Figure 6.12: Bode plot displaying phase change vs. applied frequency after each incubation with three target DNA sequences. The matching DNA2 sequence causes a greater phase change between the frequencies of 100 - 1000 Hz indicating an increased capacitance..... 137

Figure 6.13: The percent change in R_{ct} for two different sensors in the same channel after incubation with 3 target ssDNA sequences. Each sensor displayed a clear decrease in R_{ct} after incubation with the matching DNA sequence..... 138

Figure 6.14: Schematic example of how DNA hybridization can cause probes to stand upright and allow more ions to interact with the electrode. Reproduced from [169]. 139

Figure 7.1: Cross section layer structure of the microfluidic device with a patterned silicon dioxide layer used to expose sensor areas. Picture is not drawn to scale..... 145

Figure 7.2: Depth profiles along a pit patterned in glass directly after the ICP etch (a) and after dipping the wafer into HF for 15 seconds (b). The depth is around 5 microns with deeper notches observed around the inner edge. 147

Figure 7.3: Biosynthetic pathway for the production of AI-2 converted from the substrate SAH via the enzymes Pfs and LuxS. 149

1 Introduction

1.1 Motivation

Clinical diagnostic tools have been utilized for decades to help identify disease within patients and to discover new drugs for battling a myriad of bacterial and viral infections. These tools rely on the ability to provide data for a large array of samples with minimal effort required by the technician. On average, the development of a new drug costs approximately \$400 million and takes 15 years [1]. One factor inhibiting the progress of drug discovery or disease identification using these tools is the cost of not only the tool itself but also of the reagents required for any given test [2, 3]. Furthermore, highly trained scientists are needed to both use and interpret the output of these tools correctly which limits where screenings can take place. Thus, there has been an interest recently by researchers to improve these diagnostic tools by decreasing their cost while making them easier to use all without sacrificing sensitivity.

One of the more promising ways to improve diagnostic tools is through the use of lab-on-a-chip devices [4-9]. These devices utilize microfluidic channels to control fluid flow to portions of the chip where a variety of procedures can take place including reagent mixing, affinity based binding, signal transduction and cell culturing [10-13]. Microfluidics provides many advantages over conventional clinical diagnostic tools such as the microwell plate reader or electrophoretic gel shift assays. Microfluidic devices require 2 to 3 orders of magnitude less reagents to perform similar assay experiments (nanoliters as opposed to microliters.) Also, these devices can increase the speed by which some biological events occur due to the smaller

confinement of the species within the channels [14, 15]. Thirdly, sensors can be integrated within microfluidic devices using lithography and etching techniques which can provide label-free detection (this will be explained in further detail in section 1.3). Lastly, these devices are inexpensive to produce and require little work on the part of the technician to operate.

This dissertation covers the design, fabrication and testing of an arrayed microfluidic device with integrated sensors for the detection of various biological compounds. The compounds of interest to be detected are proteins and various DNA sequences. The proteins are involved in a study on their adhesion to various surfaces while the DNA sequences are detected via hybridization to their complementary target.

The work done with the proteins is influenced by a collaboration our laboratory has with other bioengineering and biology labs at the University of Maryland. The goal of the collaboration is to develop in-vitro diagnostic tools to discover drugs that can combat bacterial biofilm formation. Biofilm formation in the body can cause severe infection which may require invasive surgery to remove the infection [16, 17]. Specific proteins have been identified from common bacterial species such as *E. coli* that are vital in the production of the biofilm [18-21]. The detection of these proteins *in vitro* provides a platform that can be used to screen for drugs that inhibit the production or activity of the proteins thus disrupting the creation of the biofilm.

DNA hybridization detection is used extensively to diagnose genetic disorders [22-24] and various forms of cancer [25-27]. Every year, multiple strains of influenza are identified in patients using results from DNA hybridization techniques [28-30]. In

fact, 36,000 people die each year in the United States alone from the influenza virus [31]. All of these situations could benefit from a bench-top microfluidic device that can perform the same assay techniques as a plate reader or gel shift assay at a fraction of the cost without sacrificing sensitivity or specificity. Examples of sensitive microfluidic devices can be found in section 1.3.2.

1.2 Summary of Accomplishments

1.2.1 Fabrication and testing of an arrayed label-free sensing platform

The primary focus of this dissertation is the fabrication and testing of a prototype device to perform arrayed detection of affinity based binding events. The device includes a series of elastomer microfluidic channels with a matrix of individually addressable sensors and measurement electrodes. The direction of the fluid flow across the sensor matrix can be changed by rotating the channel layer to provide either horizontal or vertical channels. Each sensor provides the ability to use electrochemical techniques to probe for any binding reactions occurring on the surface. Controlling the fluid flow through the device allows the user to pattern multiple sensor sites while minimizing any cross-contamination. A unique electrode design allows for many sensors to be addressed by only a few peripheral contact pads as discussed further in section 2.4.2. Further details about the device are explained in chapter 2 of the dissertation.

To further the study of the microfluidic array platform, microvalves were integrated to enhance the fluid control. This integration involved a design change of the microfluidic channels themselves and more complicated fabrication procedures.

The effects that the valve integration had on the diffusion of the system as well as the impedance sensing mechanism concerning DNA hybridization were explored.

1.2.2 Study of protein adhesion to various functionalized surfaces

As discussed above, detecting the presence of particular proteins is of great interest to the drug screening community and was one of the leading factors that lead to this research. A common gene regulator protein in *E. coli*, the cAMP receptor protein (CRP), was chosen to focus the protein detection study [32-34]. During the course of this study, it was found that CRP displayed adhesion affinity to many different types of surfaces. This observation led to the use of the arrayed device to analyze adsorption of proteins to various passivated surfaces. To our knowledge, this is the first example of a microfluidic device employing electrochemical detection for the purpose of characterizing protein adhesion.

To validate the arrayed capability of the device, two other proteins were purchased, tumor necrosis factor α (TNF α) and tumor necrosis factor β (TNF β). Each protein is a commonly known cancer marker and both are widely studied [35-37]. Further details regarding how the device was used for this study and what was learned from the data can be found in chapter 5.

1.2.3 DNA hybridization study throughout all stages of device design

Electrochemical analysis was used to observe various DNA oligomers successfully hybridizing to their complementary target sequence. This work began by performing the detection with the large scale electrodes and continued with the microfluidic device, and finally, was demonstrated within the device integrated with valves to control the fluid flow direction.

The key novelty with this accomplishment is the ability to perform the arrayed detection of multiple hybridization events in a single device without the need for labeling either of the DNA strands. Typically, experiments require a fluorescent or enzymatic label on the target strand in order to receive an output signal [38, 39]. The method discussed in this dissertation can detect the DNA hybridization through the use of a free redox compound and can do so in an easily arrayed format.

1.3 Literature Review

This section covers a breadth of published work that is related to this dissertation. It is meant to help highlight the novel aspects of this work and how it contributes to the field of clinical diagnostics and drug screening. The first section covers established techniques used for drug discovery and drug screening as well as other examples of recent technology being utilized for this purpose. The next section provides an overview of how microfluidic devices specifically have been used for diagnostic testing. The final section summarizes the array of literature on electrochemical sensing both at the macroscale and at the microscale.

1.3.1 Conventional drug discovery and screening techniques

There are numerous established techniques for performing drug analysis in the laboratory. These include the use of microplate readers, gel shift assays and flow cytometers. These instruments provide multivariate analysis for a high number of loaded samples. Each of these instruments will be briefly reviewed here including any drawbacks that can be addressed by the work presented in this dissertation.

1.3.1.1 Microplate readers

Microplate readers are the most common tools utilized in labs around the world for high throughput drug screening. These devices contain an optical detection system that can scan multiple solution wells of varying sizes and report absorbance or fluorescence data. By using the plate reader, different tests can be performed within the solution wells including cell growth assays [40, 41], immunoassays [42, 43] or DNA hybridization [44, 45].

Microwell plates can be purchased in a variety of shapes and sizes. One of the most commonly used sizes is the 96-well plate with each well able to hold about 500 μl of liquid. However, plates exist which can contain over 1000 individual wells with each well holding less than 10 μl of fluid. These plates range in price from hundreds to thousands of dollars per plate depending on the quality of the plate material and the size [46]. Figure 1.1 below displays pictures for both a common 96-well plate and a 1536-well plate.

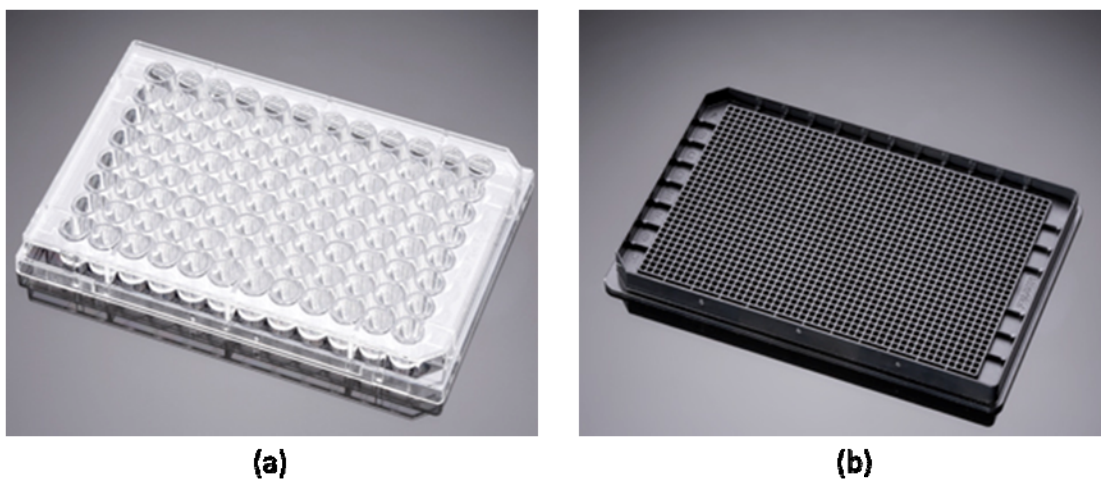


Figure 1.1: (a) photograph of a typical 96 well plate and (b) a more dense 1536 well plate. Images reproduced from [46].

Of the various uses of the microplate reader, one of the most common tests performed is known as the enzyme-linked immunosorbent assay or ELISA [47, 48].

ELISA is a technique which binds either enzyme-linked antibodies or fluorescently tagged antibodies to particular antigens immobilized in the well. A substrate is further added that is then converted by the enzyme linked to the antibody into an optical, typically fluorescence, signal. This substrate can also cause a color change in the liquid which can be quantified via absorbance measurements at a particular wavelength. Although ELISA is one of the leading analysis methods for analyte detection, it requires numerous time-consuming incubation and flushing steps and is wholly dependent on the activity and availability of the fluorescent label for a particular antigen.

Due to the popularity of plate readers in the lab setting, many groups have researched new devices that work in conjunction with the plate reader to improve the performance and sampling rate. An example of this is an automated sampling microdevice with integrated capillary electrophoresis (CE) and mass spectrometry (MS) developed by Zhang et al. [49]. The microdevice contained chemically etched channels in glass and was sandwiched between machined polycarbonate containing platinum electrodes for CE separation of the sample and pressure inlets for driving the fluid flow. A 200 μm inner diameter capillary was fixed to one end of the etched fluid channel and an electrospray tip of 25 μm inner diameter was fixed to the output end of the fluid channel. A schematic displaying how the device interfaces with the microwell plate is seen in Figure 1.2. Pressure was used to draw 500 nL of liquid out of a microwell through the capillary, while a high voltage applied to the platinum electrodes separated the particles for MS analysis at the output end. A mixture of various proteins was used and the presence of each one was detected using the device.

The motivation behind this published work was to reduce the sample volume required for analysis while quickening the sample preparation pace.

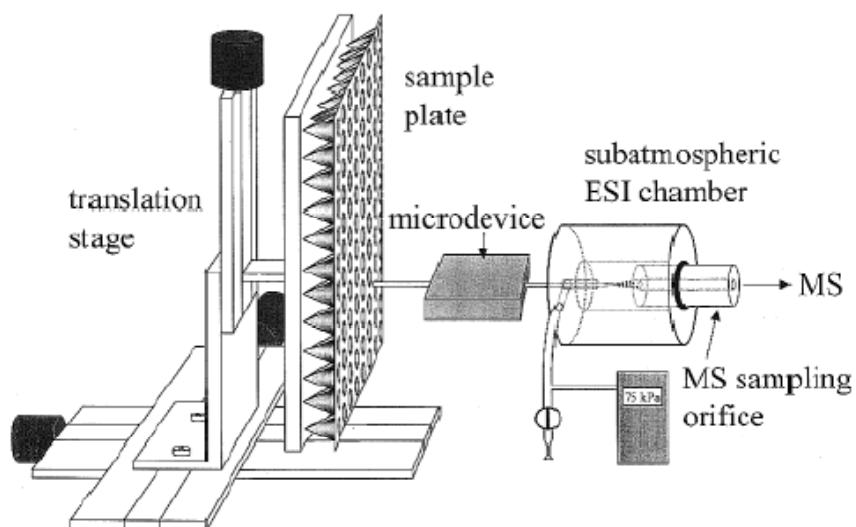


Figure 1.2: Design of the coupling of the microdevice with attached CE and MS components to the vertically mounted microwell plate. Reproduced from [49].

For certain cell culturing studies, the use of a microwell plate may have specific advantages over micro-patterned templates. A recent study by Sakai et al. compared the growth of mouse embryonic stem cells cultured in the wells of a microwell plate to those cultured in either microfabricated wells or over printed gelatin spots [50]. The microfabricated wells were milled to be 600 μm deep and 600 μm wide and were covered with polyethylene glycol to reduce cell adsorption. The gelatin spots of 200 μm diameter were fabricated via microcontact printing with the surrounding surface passivated with polyethylene glycol. The results demonstrated a higher cell growth rate and larger embryonic bodies (clusters of embryonic stem cells) with the 96 well plate vs. both micropatterned techniques. Although the stem cells would grow and proliferate for all of the cases studied, the environment of the 96 well plate proved to be more ideal for stem cell research. Although the work described in this dissertation does not involve the use of living cells, it is still

important to note that such microfluidic devices may not be ideal for all facets of clinical research.

Microwell plate readers have proven to be valuable tools for diagnostic research but there are some drawbacks when performing binding affinity assays. Due to the external optical measurement equipment required for data collection, a fluorescent or enzymatic label on one of the compounds is necessary. This labeling procedure requires extra sample preparation steps and in some cases can compromise the integrity of the compound being labeled [51]. The microfluidic device presented in this dissertation contains integrated sensors to provide label-free analysis of various binding events.

1.3.1.2 Gel Shift Assays

An electrophoretic mobility shift assay, or gel shift assay, is a common technique employed primarily to determine protein binding to either DNA [52-54] or RNA [55, 56]. The results are based upon the migration of the nucleic acid sequence through a polyacrylamide or agarose gel due to an applied electric field. The DNA/RNA migrates through the gel towards the positive terminal since it is negatively charged. If protein is bound to the DNA/RNA, this migration will be slowed. The DNA/RNA is typically tagged with either a fluorescent [53] or radioactive [52, 54] marker to determine its location in the gel after a set amount of time exposed to the electric field. This concept for a DNA-protein or RNA-protein affinity assay was developed in the early 1980's and has been used extensively ever since [57, 58]. This method can also be used to separate molecules based on their size

and charge in a process commonly known as gel electrophoresis [59, 60]. The results from a typical gel shift assay are shown below in Figure 1.3.

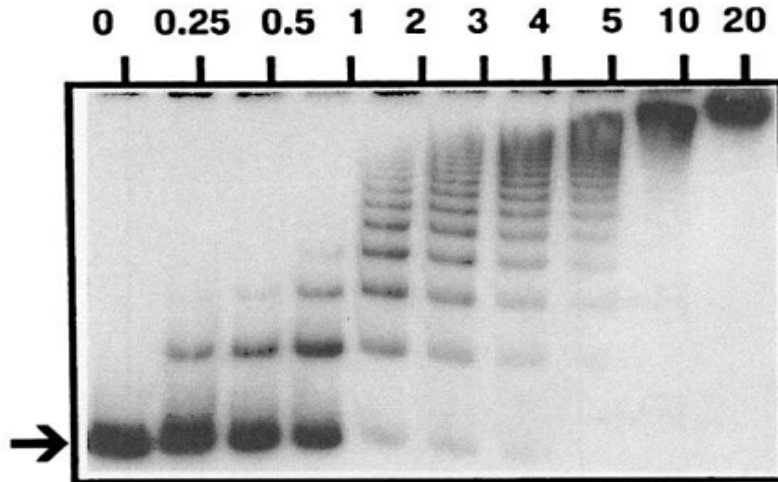


Figure 1.3: Results from DNA tagged with a radioactive label migrating through an acrylic gel with various protein concentrations added to each lane (in nM). The arrow indicates the band which corresponds to the shift of DNA with no bound protein. Reproduced from [61].

The image result shown in Figure 1.3 displays the distance that the DNA was able to travel through the gel in each lane. The first lane on the left contained only DNA while each additional lane included increasing protein concentrations with the amount shown above the lane in nM. Increased binding of protein to the DNA at higher concentrations slows the migration of the complex through the gel, resulting in bands appearing in the lanes well before that of the lane with only DNA added.

The binding properties between specific gene sequences and proteins give useful information regarding the effectiveness or creation of new drugs. As such, gel shift assays provide a useful tool for this purpose, but improvements can be made. Like the microwell plate reader described earlier, gel shift assays require labeling to provide a signal. Furthermore, these assays rely heavily on the quality of the gel used and the results can be greatly affected by gels of varying pore sizes.

1.3.1.3 Flow Cytometry

Flow cytometry is a high throughput analysis technique that is capable of analyzing up to thousands of particles every second. The analytes to be studied are suspended within a sheath fluid via hydrodynamic focusing [62]. A laser beam is focused to intersect the fluid flow and a series of photodetectors are arranged to collect both the forward scattered and side scattered light from interaction of each analyte in solution as it passes through the beam. Analytes can also be tagged with various fluorescent labels with the photodetectors used to collect the emitted light. The combination of the collected scattered light plus the fluorescent emission give researchers information about the presence of various biomolecules such as DNA [63, 64], proteins [65-67], and cells [68-70]. Early flow cytometers used impedance measurements and the coulter counting principle to make accurate counts of the number of different types of cells that were present in a solution [62]. Eventually, the use of advanced optics allowed for more data than just the count to be collected from the sample.

A schematic of how flow cytometry works is shown in Figure 1.4. The creation of the sheath fluid around the sample fluid is made possible due to laminar flow as the channel dimensions reduce to the sub-millimeter scale. The focusing of the fluid allows for only a single cell to pass the laser beam at any given time. Carefully aligned mirrors and dichroic filters guide the scattered and emitted light to each photodetector.

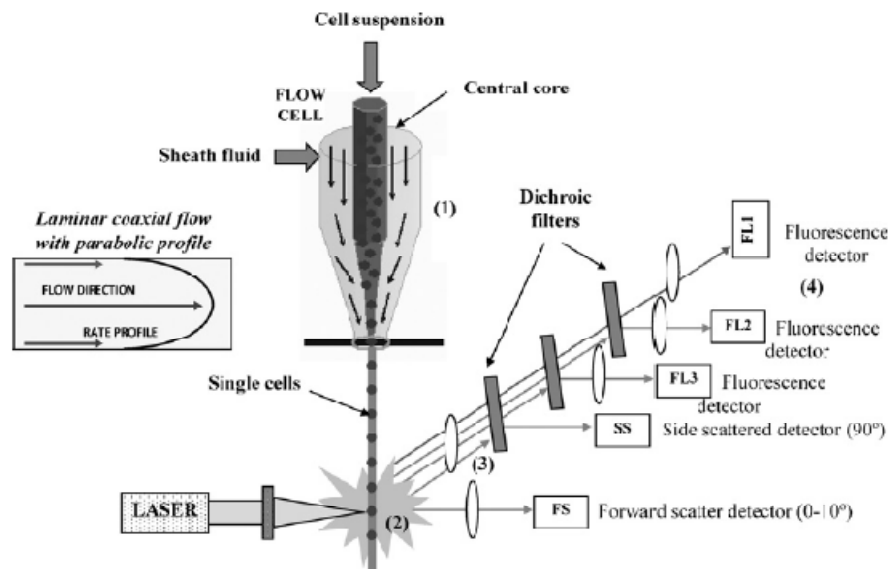


Figure 1.4: Schematic displaying how flow cytometry works. The scattering of the laser light coupled with the fluorescence emission provide data for each cell passing through the beam. Reproduced from [69].

Recent advances in the field of flow cytometry have attempted to scale down the system in order to speed up the sample introduction rate and to reduce the cost. A microfluidic chip designed by Sakamoto et al. was recently used for this very purpose [70]. Two microfluidic channels in a cross configuration were formed in molded polydimethylsiloxane (PDMS) and bonded to a glass substrate using oxygen plasma. Samples of various *E. coli* cell populations were flown between a sheath fluid of PBS introduced into the perpendicular channel. The fluorescently stained cells were then counted through the use of a fluorescent microscope aimed down at the channel at high magnification. The cell counts achieved by the authors for various populations showed excellent correlation with conventional counting techniques.

An even more recent example of a portable flow cytometry system is described by Joo et al. [71]. The system includes both impedance and fluorescence detection of particles. Channels were etched in glass and two electrodes facing one another in the channel were fabricated using polyelectrolyte gel. A constant DC voltage of 0.4 V was applied across the electrodes to observe impedance changes over

time as the analytes passed between the electrode pair. Fluorescence measurements were carried out with a blue LED for excitation, a dichroic mirror, and a silicon photomultiplier tube for the detection of the emitted light. A schematic of the entire system is shown in Figure 1.5.

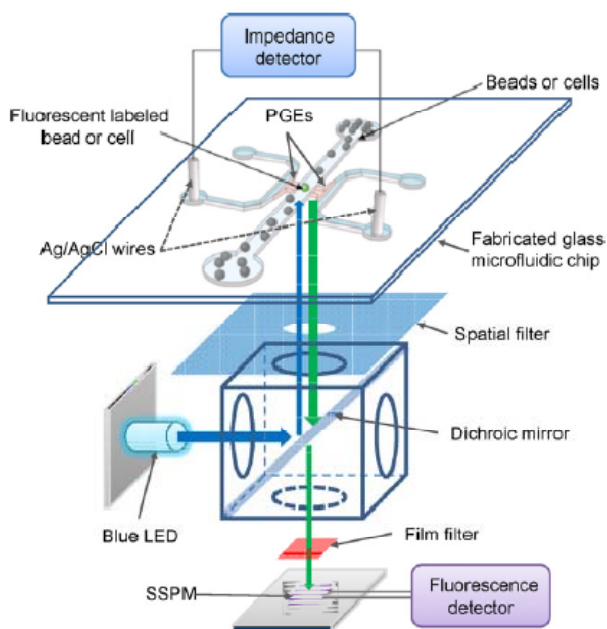


Figure 1.5: Schematic of the portable flow cytometry and impedance detection system. A DC voltage is applied across the microfluidic channel while fluorescence detection is performed using free space optics positioned beneath the channel. Reproduced from [71].

Collected impedance values were correlated to the size of various beads passed through the device while optical data was collected for fluorescently tagged beads. Live cells transfected with GFP (green fluorescent protein) were used and the emitted light was detected. This published work highlights the recent drive to miniaturize conventional laboratory equipment to greatly reduce the cost of not only the system but of the required reagents.

All three conventional laboratory tools and techniques discussed here (microwell plate readers, gel shift assays, and flow cytometry) have the ability to perform high-throughput screening for the clinical diagnostic community. However,

the need for the sample in all three tools to have some sort of label to be detected is a major drawback. This labeling procedure adds extra steps to the sample preparation process and can also damage some labile biomolecules [51, 72]. Furthermore, the high cost of these systems and the amount of reagents they require to operate can be prohibitive to research being performed at lower funded institutions. The unique microfluidic device described in this dissertation aims to provide a high-throughput drug screening platform without the need of labeling and with drastically reduced sample volumes compared to these conventional tools.

1.3.2 Microfluidic sensors

As discussed in the motivation section of this chapter, microfluidic total analysis systems (microTAS) provide numerous advantages in the clinical diagnostic field. The inclusion of integrated sensors allows for label-free detection of various biomolecules and drastically reduces the reagent volumes required for an experiment. This section highlights some of the recent published research involving microfluidic devices with integrated optical, mechanical and electrical sensors for the detection of biomolecules.

1.3.2.1 Optical sensors in microfluidics

The abundance of optical detection techniques for conventional laboratory equipment has understandably led to the integration of optical components within microfluidic devices. These devices can contain integrated photodiodes and light sources [73-75] or can be packaged with optical fibers to couple light from external optical sources and detectors [76-80]. Specific examples of such devices are explained further in this section.

Balslev *et al.* fabricated a lab-on-a-chip device which integrates microfluidic and active optical components [73]. The device consists of a silicon substrate with a top 3 μm layer of silicon dioxide. A 10 μm thick film of SU-8 is patterned to define fluidic channels, waveguides, and the Bragg grating for a dye laser. Rhodamine 6G in solution was excited to produce a narrow emission at 576 nm through each of the waveguides. Embedded photodiodes in the doped silicon substrate collect the light that passes through the on-chip cuvette. The device also contains a passive mixer for the input solutions before they are delivered to the cuvette. A thin layer of PMMA sandwiched between the top of the device and a glass plate provided leak-proof sealing. The authors demonstrated the operation of the dye laser and the ability to measure its output using the photodiodes. Providing such dense integration of multiple laboratory components onto a single chip is illustrative of the benefits microfluidics provide for drug screening devices, even though this particular work did not demonstrate particular sensing capabilities.

Another recent work by Lee *et al.* demonstrates an arrayed microfluidic chamber for surface plasmon resonance (SPR) detection of bound species to the sensor [81]. The device also incorporates on-chip valves, pumps and heaters. A schematic of the device is shown below in Figure 1.6. The heaters and temperature sensors were both fabricated by patterning platinum on the substrate while the valves and pumps were molded in PDMS.

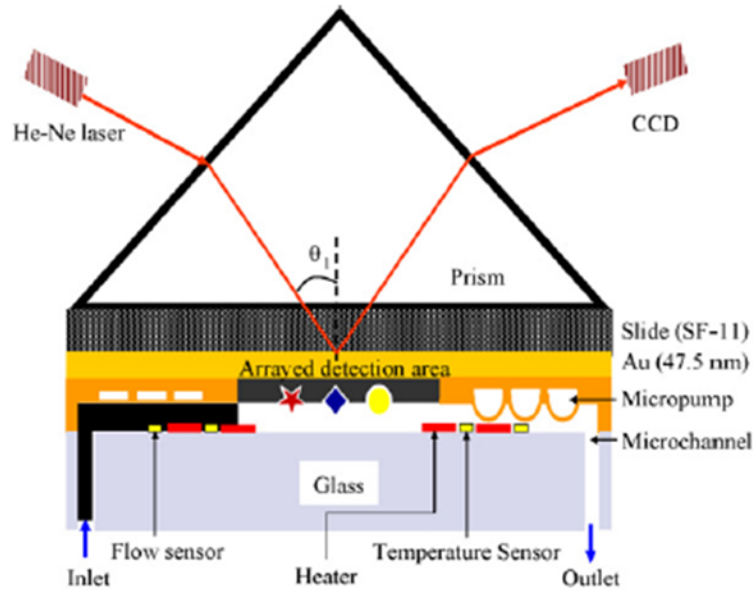


Figure 1.6: Schematic of SPR microfluidic device. The incorporation of so many components in a small footprint demonstrate an advantage leveraged by microfluidic design. Reproduced from [81].

Surface plasmon resonance is an optical technique in which Plasmon waves are excited along a metal surface by directing the light at a particular angle through a prism. The binding of biomolecules to the surface changes the critical coupling angle. Since SPR detection is sensitive to temperature changes in the environment, heaters were incorporated to help stabilize the measurements. An immunoassay involving IgG antibodies was carried out in the device and the binding was detected through a phase shift in the collected light. The limit of detection was found to be 0.67 nM. The dense collection of various elements within the device including heaters, pumps, valves and sensors highlight the versatility of lab-on-a-chip systems. However, the free space optics required for performing label-free SPR detection are bulky and greatly complicate testing due to the alignment sensitivity of each component.

1.3.2.2 Mechanical sensors in microfluidics

The use of mechanical based sensing within microfluidics is less common than using either optical or electrical means. Difficulties with the integration include

damping of the mechanical structure when in liquid as well as stiction to the substrate of any hanging structures during the evaporation phase of the liquid [82, 83]. Nevertheless, the high sensitivity afforded by mechanical sensors has still led to research performed in this area. Microscale cantilevers [84-86] and bulk piezoelectric materials [87-89] have been demonstrated to function with high sensitivity in fluid environments. A few recent examples are explained further here.

An excellent example of cantilever sensors fabricated within microfluidic channels is demonstrated by Koev et al. [85]. The cantilevers were fabricated from thin ($\sim 2.2 \mu\text{m}$) SU-8 and included a layer of gold ($\sim 15 \text{ nm}$) on the top surface. The stress gradient through the SU-8 polymer caused the cantilevers to bend up off of the substrate by $1\text{-}2 \mu\text{m}$ once released. The transparency of the cantilever and the thin gold layer allows for interferometric measurements to be taken using a simple microscope to determine how far the cantilever bends due to binding of biomolecules to the gold surface. Microfluidic channels were molded in PDMS to deliver liquid samples containing various concentrations of homocysteine to each fabricated cantilever. Homocysteine can bind to the gold surface via its thiol group and cause the cantilever to bend further away from the substrate due to the added surface stress. The cantilevers also displayed high bending sensitivity to the pH of the solution and could double as a pH sensor. The problem of stiction was still a factor in this work, however, and the cantilevers had to be immersed in aqueous solution at all times after being released from the substrate.

Lange et al. demonstrated a single microfluidic channel aligned over a surface acoustic wave (SAW) sensor [89]. Two sets of interdigitated electrodes are

patterned over a piezoelectric substrate across from one another. A bulk acoustic wave is generated through the piezoelectric material via an AC potential applied to one set of electrodes and the wave is transduced back into an AC electrical signal at the second set of electrodes. The resonant frequency and velocity of the generated wave are highly sensitive to mass loading and viscosity changes at the surface. The authors create a microfluidic channel in a UV photopolymer and align it over the SAW sensor active area. The completed device is shown in Figure 1.7. The piezoelectric material used for generating the SAW is lithium tantalate (LiTaO_3). The authors demonstrated resonant frequency shifts of 23 kHz over a time period of 6 minutes when injecting a sample containing 4 mg/ml bovine serum albumin. The protein adsorbed to the surface and the mass loading caused the resonant frequency of the wave to decrease. Although successful integration of the various components was shown, consistency between different SAW sensors was difficult to achieve due to variable contact pressure on each of the sensor surfaces.

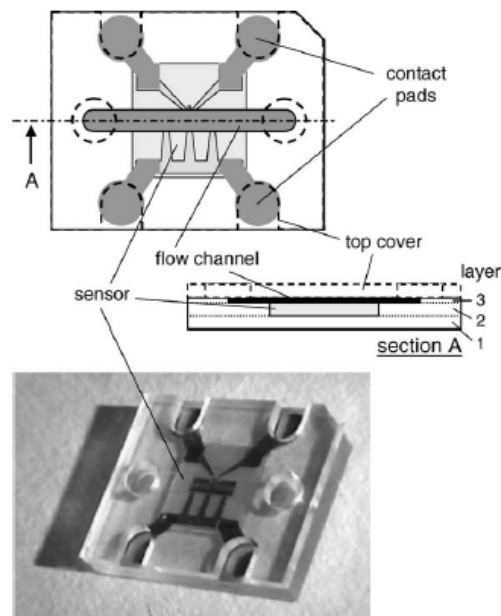


Figure 1.7: Device schematic and photograph demonstrating the packaging of a microfluidic channel over a SAW sensing chip. Reproduced from [89].

1.3.2.3 Electrical sensors in microfluidics

There are many advantages to using electrical signals to perform biological and chemical detection in microfluidic systems. The fabrication is inherently less complicated since these sensors typically only require patterned electrodes to operate. In addition, electrical signals can be directly interfaced with most measurement equipment while other signal modalities may require a transducer to convert the signal. Electrical sensors commonly measure changes in impedance [90-92], capacitance [93-95], or the redox activity of enzymes [96-98]. Some recently published examples of electrical sensing in microfluidics are discussed here.

Nashida et al. have designed a microfluidic device with sequential injection and flushing functions for conducting immunoassay studies using amperometry [99]. Solution moves through the hydrophilic channel due to capillary action, but stops at patterned hydrophobic electrodes. By applying a negative potential, the electrode surface becomes hydrophilic and the liquid continues on. The channels were formed by patterning a dry film photoresist on a glass substrate with a PDMS layer to seal the device. The completed device is shown in Figure 1.8.

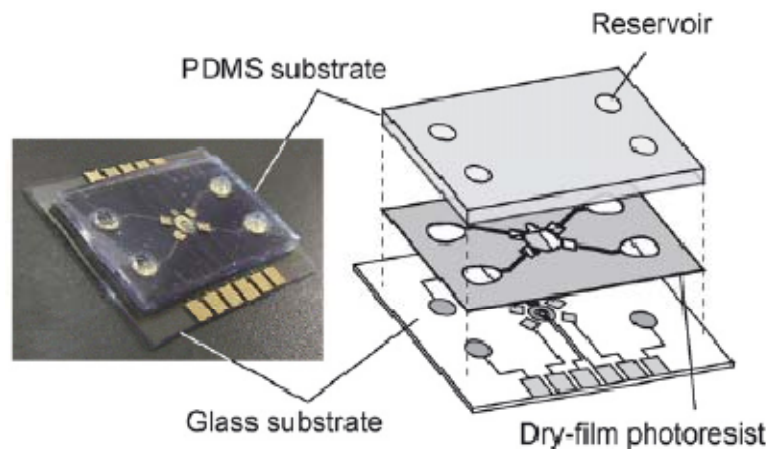


Figure 1.8: Photograph and schematic of microfluidic device containing integrated electrodes for both sensing and fluid control. Reproduced from [99].

An ELISA based study was performed using this device by immobilizing either particular antigens or antibodies to a platinum working electrode. An enzyme-linked secondary antibody is bound to the complex and produces a current when voltage is applied. This work demonstrates the use of integrated electrical sensors in microfluidics for drug based analysis. It also contains the novel inclusion of electrical components to act as valves by creating a hydrophobic surface to impede fluid flow, however, the device only contains a single sensor precluding high-throughout analysis.

A second excellent example of utilizing the advantages of working in the microfluidic regime to create a sensor is demonstrated by Frey *et al.* [100] The device contains an input sample reservoir and a buffer reservoir which flows beneath the sample channel. Due to laminar flow in the channel, by adjusting the two flow rates the authors demonstrate the ability to linearly control the sample concentration downstream in the channel. Three sensing electrodes are patterned at the far end of the channel with each electrode functionalized individually via a second network of smaller microfluidic channels. Redox activity from enzymes patterned on each of the electrodes allowed for the detection of various concentrations of glucose and lactate in the sample solution. By using the laminar flow control, concentrations as high as 15 mM could be detected within the linear range vs. only 4 mM in the linear range if no additional buffer flow was used. By taking advantage of the laminar flow regime in microfluidics, the authors present a unique solution to increase the linear range of electrical based sensing for enzymatic catalysis. One drawback to this technique is that the minimum level of detection was very high (0.2 mM).

Optical, electrical and mechanical sensors have all been integrated with microfluidics with success. Of the three, however, electrical sensors are easier to fabricate and rely less on the inclusion of labels for analyte detection. Furthermore, optical sensors typically require additional, bulky light coupling equipment and mechanical sensors suffer from problems of both stiction and damping in liquid. For these reasons, electrical sensors have been chosen to use for the device presented in this dissertation. Specifically, both cyclic voltammetry (CV) and impedance spectroscopy (EIS) will be utilized for biomolecule detection and is discussed more in depth in section 2.3.

1.3.3 Characterization of protein adsorption

One of the targeted applications for the designed microfluidic device is to provide an arrayed platform for characterizing protein adhesion to a variety of functionalized surfaces. Non-specific binding of various biological compounds is a hindrance to producing a selective sensor surface. Typically, the surface is passivated with various chemical or biological compounds to help reduce adsorption of unwanted proteins or other biomolecules that may be present in the sample. In order to characterize many of these adsorption interactions, researchers have used quartz crystal microbalance (QCM), electrochemical sensing, atomic force microscopy (AFM), and surface plasmon resonance (SPR). This section provides a brief summary of each of these techniques.

The most common technique for measuring protein adsorption to a surface with electrical measurements is to use a quartz crystal microbalance (QCM) [101-104]. Adsorption of proteins to the functionalized surface of the resonator can be

detected with very high precision from the change in resonant frequency. Although this technique is very sensitive, it uses a single store-bought resonator for one measurement making an array of tests a difficult and time-consuming task. Other electrical techniques commonly employed are cyclic voltammetry [105] and impedance-based methods [106, 107]. However, these techniques typically utilize a single enclosed fixture during the experiment, which complicates high throughput analysis.

Direct contact measurements from an AFM probe tip have been demonstrated to provide data regarding the adsorption kinetics of various proteins [108, 109]. Extremely fine tips are raster scanned over a sample producing an image which can portray not only the density of the adsorbed protein, but morphology data as well. Although AFM measurements can give nano-scale precision for mapping adsorption phenomena, it is a very slow and inherently serial process.

Optical techniques such as surface plasmon resonance (SPR) have also been employed to detect protein adsorption [106, 110, 111]. With this technique, minor changes in surface dielectric properties on an electrode change the angle at which surface plasmon waves are generated from an incident beam of light. SPR has been used for many years for detecting binding and adsorption of various compounds, however, it requires expensive free-space optical equipment and difficult alignment of all the components. Other optical techniques such as total internal reflection fluorescence (TIRF) has been reported for protein adhesion characterization, but it requires labeling of the proteins with a fluorescent dye [112].

None of the methods so far discussed in literature for characterizing protein adsorption have attempted to do so in an arrayed, microfluidic format. The device presented in this dissertation successfully performs this arrayed characterization which can drastically reduce the time necessary to screen a large library of proteins versus numerous passivation surfaces. Furthermore, the use of electrical measurements reduces the fabrication complexity and eliminates the use of bulky external measuring equipment as seen with AFM or most optical techniques.

1.3.4 Electrochemical sensors for DNA hybridization

Beyond characterizing protein adhesion, another goal of this research was to detect DNA hybridization by using electrochemical measurements. Electrochemical sensors have been used extensively over the past decade to analyze the affinity of specific DNA sequences to one another. This section gives a brief overview of some of the published literature on using electrochemistry for DNA hybridization in both macro-scale and micro-scale studies.

1.3.4.1 DNA Hybridization – Macroelectrodes

Due to the many advantages of label-free electrochemical sensing, it has been used extensively for detection of DNA hybridization events [113-117]. Macro-scale electrodes in the millimeter range in conjunction with beakers of solution can be used to provide very sensitive data regarding the binding kinetics of single stranded DNA sequences to their matching complement. Selected research on this topic is presented in further detail here.

Kukul et al. immobilized single DNA strands onto a store-bought gold electrode for detection of influenza virus gene sequences [29]. The gold working

electrode was 1 mm in diameter and functionalized with DNA single stranded probes of 23 base pairs in length. The DNA formed a self assembled monolayer via an affixed thiol group. Electrochemical impedance spectroscopy measurements were carried out in a beaker of electrolyte containing a dissolved redox compound before and after hybridization to complementary and non-complementary DNA targets. The results showed clear impedance increases only in the cases when complementary DNA virus sequences were incubated with the DNA probes. A detection limit as low as 200 fmol of target DNA was reported. The extremely high sensitivity afforded by electrochemical detection is displayed prominently in this work.

DNA can also be self assembled onto an electrode without the need to add any functional groups to the DNA strand itself. Ma *et al.* demonstrates a procedure of assembling a chemical network of *p*-aminothiophenol first on the electrode, followed by SiO₂ nanoparticle assembly and finally the unmodified DNA target which shows strong binding affinity to the SiO₂ nanoparticles [115]. Impedance measurements were carried out in the same way as described previously in the work by Kukol *et al.* A DNA gene sequence specific to transgenically modified plants was detected at concentrations as low as 100 nM. The sensor also demonstrated the ability to detect single base-pair mismatches amongst the gene sequences. A reduction of 59% and 24% of the hybridization signal occurred for both a single and double base-pair mismatch in the sequence.

Although DNA hybridization has reliably been demonstrated at the macro-scale, there are drawbacks when the screening of many samples is considered. Each electrochemical cell must be prepared individually for the measurement making it a

very time consuming process if many samples are to be tested. Furthermore, the amount of sample required scales proportionally with the size and spacing of the electrodes. A microfluidic testing environment can array numerous sensors over a small footprint and the spacing of the micro-sized electrodes in the channels drastically reduces the sample volumes necessary for detection.

1.3.4.2 DNA hybridization – Microfluidics

Recently, there have been a few advances in incorporating electrochemical sensing in microfluidics for DNA hybridization. Studies have been performed on the hybridization kinetics in microfluidic channels [118-120] and on the integration of sensors for detection [121-123]. Further details regarding some of these investigations are presented here.

Pavlovic *et al.* fabricated a microfluidic flow cell containing more than one working electrode for the detection of multiple target DNA sequences related to different strains of influenza [30]. The device contains a single channel molded in PDMS and bonded over a glass substrate that includes three distinct gold working electrodes, a gold counter electrode and a platinum reference electrode. An image of the completed device is shown in Figure 1.9. Various DNA probe sequences specific to the influenza targets are sequentially bound to the working electrodes by selectively applying high voltages to particular electrodes to remove any bound biomolecules. Each oligonucleotide also contains a redox intercalator, methylene blue (MB), at the opposite end of the thiol group. Upon hybridization, the DNA unwinds completely and the MB moves further away from the electrode surface, thus reducing the electrochemical signal.

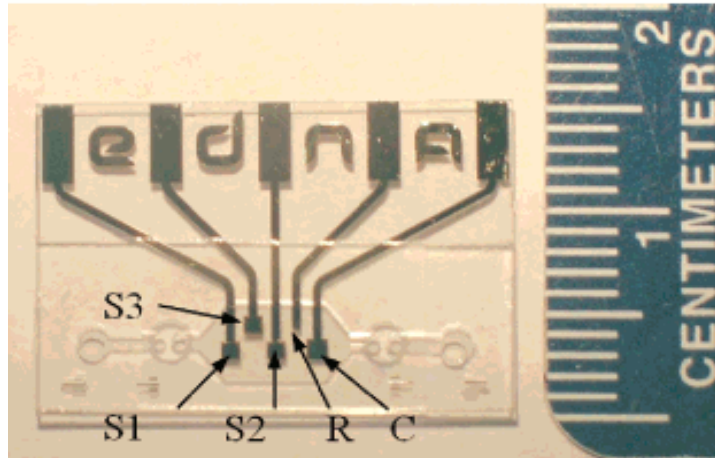


Figure 1.9: Photograph of microfluidic device for DNA hybridization. The main chamber has three sensing electrodes (S1-3), one reference electrode (R) and one counter electrode (C). Reproduced from [30].

The hybridization of the different influenza targets could be determined using AC voltammetry and the sensor surface could be regenerated by flushing DI water down the channel. This work presents an excellent example of how microfluidic devices can allow for dense integration of DNA based sensors. Although three separate sensors are included in the device, only one reaction chamber is present which makes the process of functionalizing each sensor separately very time consuming.

Goral et al. incorporated an interdigitated electrode finger array in a single microfluidic channel for DNA hybridization detection with a dynamic range of 1 – 50 fmol [124]. Briefly, liposomes containing a redox compound were conjugated with a capture probe for synthetic Dengue virus gene sequence and magnetic beads were also conjugated with a probe for the same sequence. Upon mixing the three compounds, the virus sequence bound to both the liposomes and magnetic beads. The entire complex was introduced into the microfluidic channel and a magnet was used to capture the bound gene sequence upstream of the electrical sensor. The liposomes could then be lysed releasing the redox compound which created a detectable current

across the interdigitated electrodes biased at a DC potential of 400 mV. This ultra-sensitive approach of performing hybridization detection in a microfluidic channel does contain the drawback of time intensive sample preparation steps and the single channel requires that each assay be performed one at a time.

For all the techniques described in this section for DNA hybridization detection, there still exists a need for an arrayed microfluidic device that can perform these tasks quicker. The device presented in this dissertation provides a platform that allows for multiple interactions to be screened in parallel and without complicated sample preparation steps.

1.4 Literature Summary

The described techniques and research in this section were presented to convey the breadth of work in this field and to highlight the unique aspects of the presented device. The drawbacks of conventional diagnostic tools were highlighted to explain why there is a growing need for smaller, less expensive lab-on-a-chip devices which can perform the same high-throughput assays. Optical, mechanical and electrical sensing modalities in microfluidic devices were discussed to justify the choice of using electrical based detection based on its relative fabrication ease. Finally, literature regarding both protein adsorption and DNA hybridization using electrical detection were described to further clarify what the presented research adds to this field.

1.5 Structure of Dissertation

Chapter 1 has introduced the motivation behind this work as well as the specific accomplishments of this research and a literature review. Chapter 2 will

cover the design and operation of the devices used including specifics regarding the electrochemical sensing aspect. Chapter 3 describes the fabrication procedure for the devices. Chapter 4 contains all the testing and characterization information for each of the device designs. Chapter 5 includes all the data and analysis regarding the protein adhesion study to various functionalized surfaces. Chapter 6 covers all of the DNA hybridization research performed. Finally, chapter 7 concludes the dissertation with a summary and a section on future work that can be used to improve the research further.

2 Device Operation and Design

2.1 Introduction

This chapter will cover the specific design elements of the microfluidic device used in this work for both protein adhesion characterization and DNA hybridization. The initial section gives a brief overview of both affinity based binding and adsorption with proceeding sections covering the electrochemical detection concept, design of the microfluidic channels, and the electrode configuration. The chapter also contains the design parameters for the integration of the microvalve network.

2.2 Interactions between biomolecules

Nearly all reported biosensors take advantage of the binding affinity between various types of biomarkers and their specific targets. These biomarkers are used as probes to confer selectivity to a sensor. Commonly used probes include antibodies, aptamers, and single or double stranded DNA. Antibodies can be engineered to bind selectively to other antibodies and proteins. Aptamers are specially designed oligonucleotides for binding a specific protein. Single stranded DNA can be used to probe for hybridization with the complementary DNA sequence while double stranded DNA can probe for protein attachment. The binding of the target to the immobilized probe on the sensor produces a signal alerting the user to the presence and even the concentration of a particular target.

Non-affinity based adsorption of a compound to a particular surface is governed primarily by hydrophobic-hydrophilic interactions and van der Waals forces. These interactions occur often in nature and prove to be a challenge when

designing a biosensor since any non-specific adsorption of material can produce a false signal or degrade the activity of the probes.

The microfluidic devices designed in this work include immobilized single stranded DNA probes to hybridize a complementary target. The devices are also used as a characterization platform for protein adsorption to various surfaces. Further details regarding both protein adsorption and DNA hybridization are explained in the following subsections.

2.2.1 Protein Adsorption

The many mechanisms that control the adsorption kinetics of proteins make the situation difficult to predict. Some of the parameters to consider include hydrophobic-hydrophilic interactions, thermodynamic forces containing both entropic and enthalpic effects, electrostatic interactions, pH of the solution and steric repulsion of the protein due to compression of the peptide or carbon chains. Positive entropic contributions are the dehydration and adsorption of the protein to the surface while a negative enthalpic contribution arises when proteins interact directly with a solid surface [125]. It has been demonstrated that protein adsorption is at a maximum at the isoelectric point (the pH at which the protein carries no net charge). Some affinity binding can be observed from proteins interacting with surfaces expressing functional head groups such as hydroxyl (-OH), carboxyl (-COOH) or amine (-NH₂).

Most groups use external measurement equipment and a trial-and-error methodology to understand what surfaces best resist or enhance the adsorption of specific biomolecules like protein. The study on protein adsorption described in this work aims to screen for these various interactions in a high-throughput manner to aid

researchers in discovering the optimal surface functionalization to resist adhesion for a particular protein.

2.2.2 DNA hybridization

A single DNA strand consists of a specific sequence of nucleic acid bases linked together with a negatively charged phosphate backbone. The nucleic acids include adenine, thymine, guanine and cytosine. Adenine binds selectively to thymine while guanine binds selectively to cytosine with hydrogen bonds. In this way, two strands of DNA each coded with a sequence of bases can exhibit binding affinity to one another if the base pairs match. The match does not have to be perfect in order for hybridization to occur, but the degree of hybridization among a population will depend on the percentage of matching pairs. If the sequence of a target DNA strand is known, a probe DNA strand can be engineered as its complement and used in a sensor to screen for the target's presence in a sample. Single stranded DNA is commonly abbreviated ssDNA while the hybridized double stranded DNA helix is abbreviated dsDNA. These abbreviations will be used from this point on in the dissertation.

Most DNA hybridization sensors immobilize ssDNA probes onto a sensor surface. One common technique is to add a functional thiol (-SH) group at one end of the ssDNA. The two ends of ssDNA are labeled the 3' and 5' end. The thiol is added to the 5' end of the ssDNA probe as a disulfide bond at the end of a chain of six methyl groups as shown below in Figure 2.1. Gold is used to pattern the sensing electrodes for the microfluidic devices and thiols form strong covalent bonds with gold surfaces.

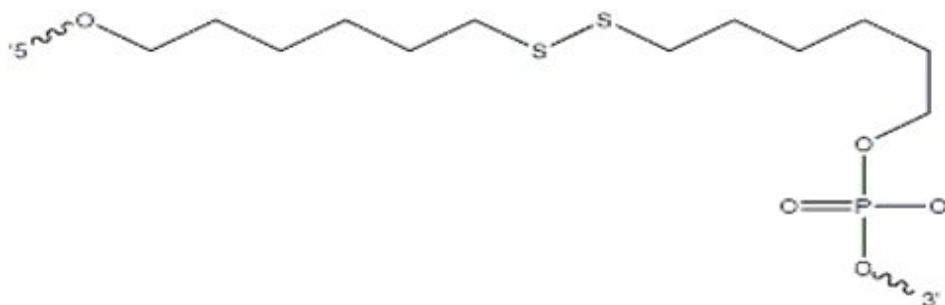


Figure 2.1: Structure of the thiol modification conjugated to the 5' end of the ssDNA.

The S-S disulfide bond protects the free thiol group from oxidation until it is ready to use. Once the disulfide is reduced, the free thiol (-SH) is left to bond the DNA to a gold surface. The spacer that is created by the 6 methyl (CH₂) groups between the thiol and the nucleotide sequence is very important. It acts like a hinge which allows the DNA to bend freely in the solution as it stands up off of the electrode surface. Without this spacer, the movement of the DNA strands would be severely restricted which would disrupt the uniform assembly of DNA on the surface and make it more difficult to hybridize the target sequence.

2.3 Device Overview

The arrayed microfluidic device contains 9 individually addressable sensors patterned within a series of microfluidic channels. The sensors themselves are thin-film electrodes patterned onto either a glass or silicon dioxide substrate. The channels are designed to form either 3 horizontal channels or three vertical channels depending on the orientation of the channel layer. In this way, sensor columns can be functionalized separately from each other while sensor rows can be used for introducing different samples and for impedance testing as displayed schematically in Figure 2.2.

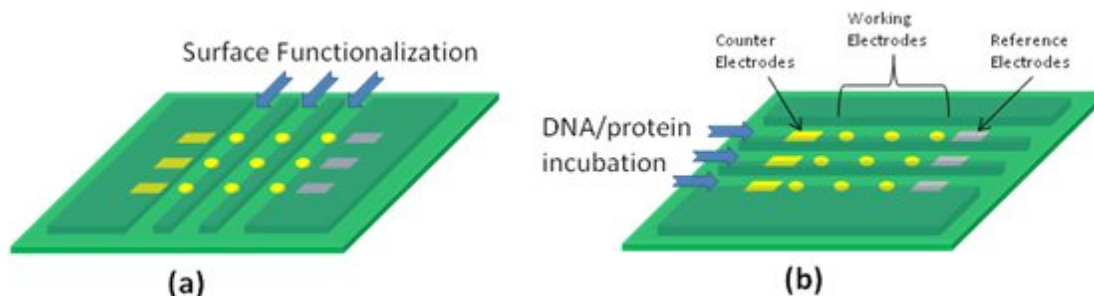


Figure 2.2: (a) The PDMS channels are aligned to expose columns of working electrodes to be functionalized by different compounds. (b) After functionalization, the PDMS channels are lifted, rotated, and placed back down to align counter and reference electrodes within separate rows of working electrodes.

Note that this figure is not drawn to scale. Each row contains three separately functionalized working electrodes and a unique reference and counter electrode for impedance measurements. As an example experiment with this platform, each sensor column can be functionalized with a different ssDNA probe sequence which will self-assemble onto each electrode surface in the channel. Afterwards, the PDMS channels can be rotated to form channel rows and solutions containing complementary target ssDNA sequences are flown in each horizontal channel to interact with each probe sequence. Only those sensors containing the correct probe-target pair will register a change in impedance. Electrochemical measurements are taken before and after target incubation for each sensor for comparison.

After performing both protein adhesion and DNA hybridization experiments using this device, a network of microvalves was integrated with the sensor array to provide autonomous control of the fluid flow direction. The valves are used to close off areas of the chip to provide either three horizontal or three vertical channels over the grid of sensors. The procedure for fabricating these valves including data demonstrating how the integration directly affects the measurement results is explained in more detail in Chapters 3 and 4.

2.4 Electrochemical Detection Concept

This section describes how electrochemical sensing works in the traditional sense and how it will be applied to a microfluidic device. The detection mechanism due to DNA hybridization or protein adsorption will be explained along with the specific techniques that were utilized for this work.

2.4.1 The Three Electrode System

Electrochemistry is based on the ability to cause chemical reactions to occur in solution through the application of voltage. One can apply an external potential to two electrodes immersed in an electrolyte solution and force both oxidation and reduction reactions to occur. At the anode, electrons are pulled away from the anions in solution. At the cathode, electrons are donated to the cations in solution from the electrode. Current can be measured from this movement of electrons based on the applied voltage. This relationship can be used to determine the activity or presence of electroactive species in the solution as well as yield information regarding any assembly of molecules on the electrode surface.

Because the interest is in the reaction that is created by the applied potential in electrochemistry, the reduction of factors that influence the measurement but are not related to the reaction is important. One substantial parasitic influence is the potential drop that exists from applying voltage and measuring current through the same electrodes. The addition of a third “counter” electrode is the answer to this problem. By applying the potential between the working and reference electrode and measuring current between the working and counter electrodes, the potential drop is greatly

reduced since no current flows into the reference electrode. This three electrode system is the most commonly used configuration in electrochemistry.

2.4.2 Detection Mechanism

The interaction of an electroactive species dissolved in an electrolyte solution with the electrode surface gives rise to the measured current. A layer of added biomolecules to the surface of the electrode will alter the current due to both changes in the diffusion rate and any electrostatic interactions.

The electroactive compound should be a redox species that can be easily oxidized and reduced at low applied potentials. The most common redox compounds contain an iron atom at their core which is either in its oxidized state, Fe(III), or its reduced state, Fe(II), such as ferrocene dimethanol [126, 127] and the ferri/ferrocyanide couple [116, 128, 129]. The ferri-ferrocyanide couple is more widely used for detecting DNA hybridization on the electrode surface. This is attributed to the net negative charge of the redox couple which shows strong interaction with the anionic DNA. Characterization experiments with both compounds are discussed further in Chapter 4. Equal concentrations of dissolved ferricyanide and ferrocyanide are used for all experiments in this work. The structure for both the oxidized and reduced forms of the compound is shown in Figure 2.3.

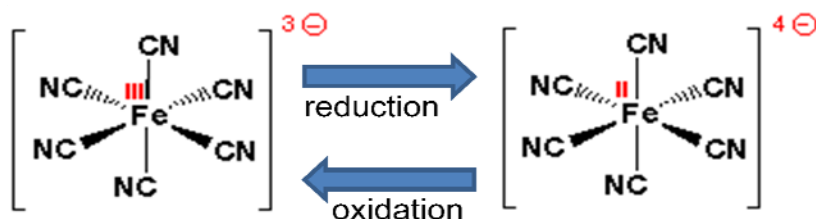


Figure 2.3: Structure for the ferri/ferrocyanide redox couple.

The electrolyte that is used during the experiment can have an important impact on the results as well. The electrolyte is a concentrated salt solution to allow for highly conductive transport of charge. It is typical that the electrolyte has a high concentration between 10 to 100 times higher than that of the redox compound. This is done for two reasons. The first is to reduce the resistance of the charge as it flows between the redox compound and the electrodes. The second is to minimize mass transport through migration (this is explained further in section 3.2.1). The most commonly employed electrolytes include potassium chloride [39, 130], potassium nitrate [131, 132] and phosphate buffered saline (PBS) [116, 133, 134]. For this work, the DNA and proteins are all suspended in solutions containing phosphate buffered saline. Therefore, in order to keep the solution environment consistent, PBS at a concentration of 10 mM is chosen as the electrolyte to use for all experiments.

Hybridization of DNA will cause the net negative charge on the electrode to increase. This in turn will create an electrostatic repulsion force on the charged ferri/ferrocyanide redox couple and hinder its diffusion towards the surface. The decrease in the redox concentration close to the electrode surface will decrease the measured current which can also be observed as an increase in the impedance of the system. This process is shown schematically in Figure 2.4. Equations and simulations which are used to predict the electrical changes in the system are found in the following sections for both electrochemical techniques utilized in this work.

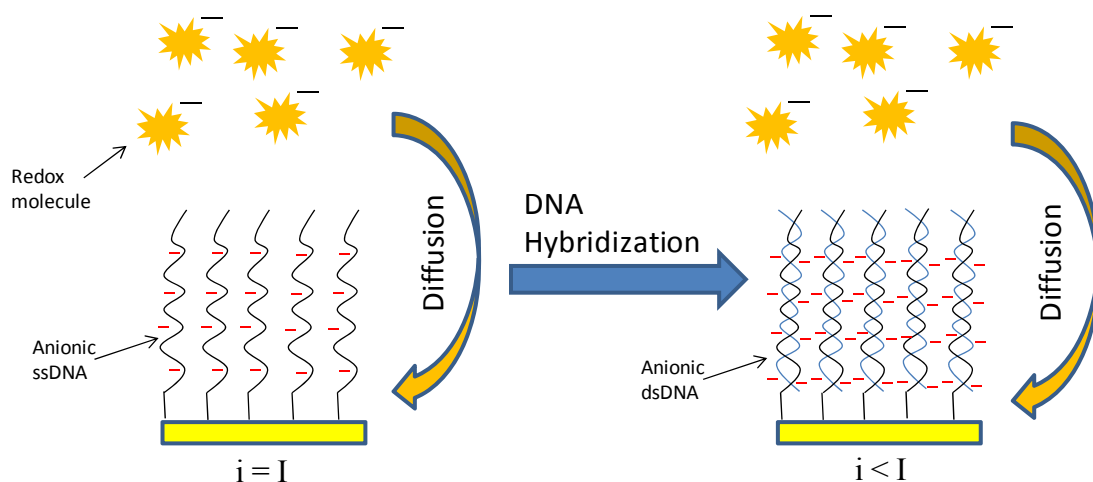


Figure 2.4: Schematic demonstrating the increased negative charge due to DNA hybridization on the electrode surface. A decrease in the measured current results from further repulsion of the charged redox compound.

Protein adhesion to the surface is expected to interact with the redox compound in a similar fashion as the immobilized DNA. Any net charge expressed on the outer amino acid molecules of the protein will have an electrostatic effect on the redox compound. One new variable to consider is the size of the proteins being adsorbed to the surface. Larger proteins are more capable of creating a physical barrier to the diffusion of the redox species close to the electrode surface. More details on the protein adhesion study are found in Chapter 5 of the dissertation.

2.4.3 Cyclic Voltammetry

Cyclic voltammetry (CV) is one of the most commonly used electrochemical techniques to probe the activity of an electroactive species. It provides information relating to the oxidation and reduction potentials for a given reaction at the working electrode surface. Based on the values of those potentials, one can use CV to identify compounds or look for changes in how the compound is interacting with the surface. CV measurements are used primarily in this research to evaluate reversibility of the redox reaction which is related to the cleanliness of the electrodes. They are also used

to perform DNA hybridization experiments with macro-scale electrodes in the millimeter range. The micro-scale electrodes patterned in the microfluidic devices display a much greater response when using impedance spectroscopy (explained further in the next section).

A CV experiment is performed by varying an applied DC voltage between the working and reference electrodes while the current is measured between the working and counter electrodes. The voltage ramps up from an initial value, E_i , to a final value, E_f , and then reverses direction back to E_i . Plotting the current vs. the applied voltage provides a graph similar to the one shown in Figure 2.5. Two distinct current peaks are observed which correspond to the oxidation and reduction potentials for the ferri/ferrocyanide redox couple. E_{pc} is the potential corresponding to the cathodic or reduction peak while E_{pa} is the potential associated with the anodic or oxidation peak. The concentrations of the reduced form of the compound compared to its oxidized form at the electrode surface can be calculated based on the applied potential by using the Nernst equation in equation 2.1[132].

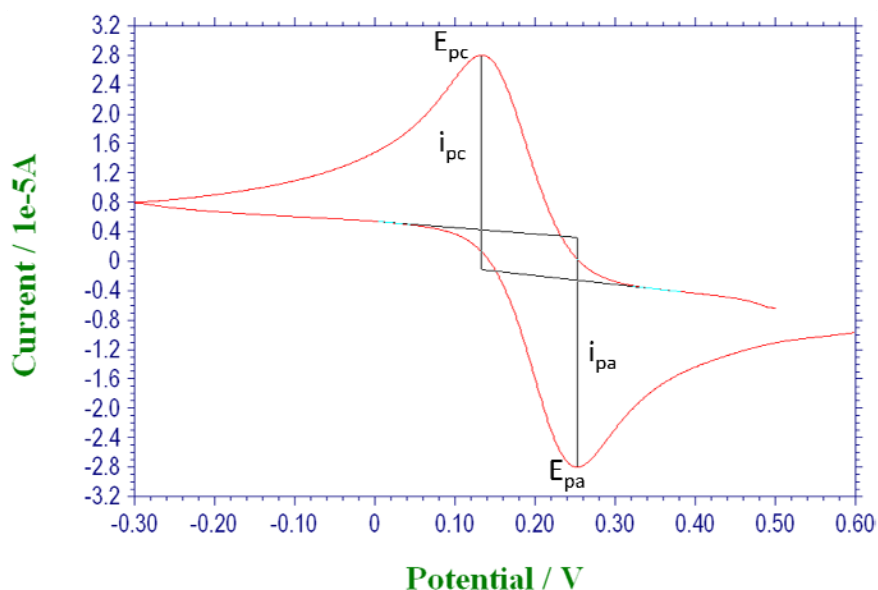


Figure 2.5: Example of a cyclic voltammogram taken on a bare gold electrode surface.

$$E = E_o + \frac{RT}{nF} \ln \frac{[a_o]}{[a_r]} \quad (2.1)$$

Where R is the universal gas constant, F is the faraday constant, n is the number of electrons transferred per ion, a_o is the concentration of the oxidized form of the redox compound while a_r is the concentration of the reduced form. E_o is the formal reduction potential and is given by equation 2.2.

$$E_o = \frac{E_{pa} + E_{pc}}{2} \quad (2.2)$$

This equation only remains valid if the reaction is reversible. A reaction is considered reversible if the total analyte that is oxidized/reduced on the forward scan equals the total analyte that is reduced/oxidized on the reverse scan. From the graph, reversibility is observed if $i_{pa} = i_{pc}$.

The reaction at the electrode surface is limited almost entirely by the diffusion of the redox couple from the bulk solution to the surface. Other forms of mass transport including migration and convection have little effect on the movement of the species in solution due to the high electrolyte concentration and short distances between the electrodes. Thus, this diffusion creates a concentration gradient of both the oxidized and reduced form of the redox couple as one moves away from the electrode surface.

The magnitude of the current for a given applied potential does not depend on the magnitude of the analyte concentration at the electrode surface but rather the concentration gradient as shown in equation 2.3 [132].

$$i = nFAD \left(\frac{\partial C}{\partial x} \right)_{x=0} \quad (2.3)$$

where A is the area of the electrode (cm^2), D is the diffusion coefficient (cm^2/s), C is the concentration (mol/cm^3) and x is the distance from the electrode surface (cm). From this equation, it is observed that the current will reach its highest magnitude when the slope of the concentration gradient is at a maximum. Equation 2.3 is derived from the more complex Butler-Volmer equation for measuring current from the redox reaction given below [135].

$$i = nFAk_o \left[[a_o] e^{\frac{-\alpha nF}{RT}(E-E_o)} - [a_r] e^{\frac{(1-\alpha)nF}{RT}(E-E_o)} \right] \quad (2.4)$$

Where k_o is the heterogeneous rate constant and α is the transfer coefficient (which is 0.5 for a reversible reaction). The peak current of the forward scan can be used to determine variables related to the reaction as described by the Randles-Sevcik equation below

$$i_p = (2.69 \times 10^5) n^{3/2} A D^{1/2} C v^{1/2} \quad (2.5)$$

where v is the scan rate of the experiment (V/s). The Randles-Sevcik equation is often used to calculate the active surface area of the working electrode. Due to surface roughness, it can be difficult to know exactly what surface area is interacting with the solution. By performing a CV experiment using a known redox compound concentration and scan rate, the area can be estimated using Equation 2.5 with a standard diffusion coefficient of 1×10^{-5} for small molecules [136].

Cyclic voltammograms were simulated using MATLAB to provide insight into how DNA hybridization on the electrode surface might affect the plots. CV

measurements were not used to detect protein adhesion. The code utilizes the Butler-Volmer equation (2.4) as well as discretized forms of Fick's diffusion laws in order to calculate the current due to the changing concentrations at the electrode surface for a given applied potential. The code was adapted from [136] and can be found in full in Appendix A.

The simulation was prepared for the redox compound that will be used for all measurements, the ferri/ferrocyanide couple. The redox couple has a well accepted standard reduction potential of about 0.2 V vs. Ag/AgCl reference electrode [25, 90]. The simulation was run three times. The first run assumed a blank electrode. The second run included a monolayer of ssDNA coverage. The third run assumes hybridization resulting in dsDNA immobilized on the electrode. The results of the simulation are shown below in Figure 2.6.

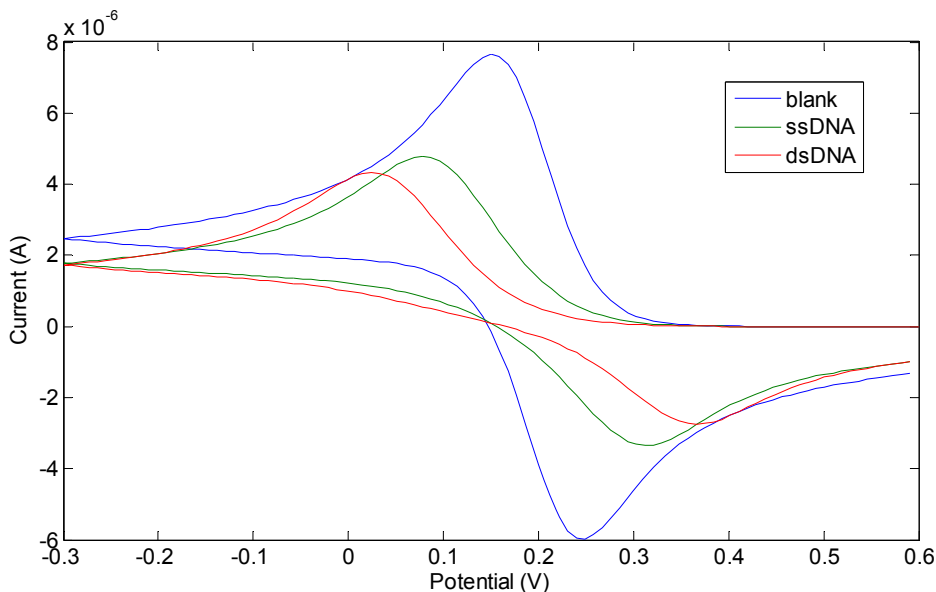


Figure 2.6: MATLAB simulation of CV results for an electrode surface covered with ssDNA and dsDNA.

The reduction of the peak heights is more pronounced between the blank electrode and the ssDNA as compared to the ssDNA and the dsDNA. This is due to

the drastic reduction of the exposed electrode surface to the redox compound following the assembly of the monolayer of ssDNA. The peak heights only decrease slightly following hybridization to dsDNA since the addition of DNA strands to the already assembled monolayer will not greatly decrease the exposed electrode area further. However, the separation of the peaks for each case is clear. Peak separation occurs due to a reduction of the heterogeneous rate constant. This constant represents the rate of charge transfer and is directly affected by the electrostatic interactions occurring between the assembled DNA and the redox compound. The added negative charge from the dsDNA produces a noticeable peak separation from the ssDNA result in the CV simulation.

2.4.4 Impedance Spectroscopy

Impedance Spectroscopy is a commonly used electrochemical technique to probe for binding events that occur at the working electrode surface. The same three electrode system comprising of a working, reference and counter electrode are utilized for the impedance spectroscopy (EIS) experiment. An EIS scan involves applying an AC potential between the working and reference electrodes while the AC current is measured between the working and counter electrodes. The frequency of the applied potential is varied and a Nyquist plot of the impedance is made.

The measured impedance of the system can be modeled using an electrical circuit. The impedance consists of the electron transfer resistance between the redox compound and the electrode surface, the capacitance between the electrode and the charged ions in the solution, the solution resistance between the electrodes and the

impedance due to the rate of diffusion of the redox compound to the electrode. These elements are arranged in the circuit shown in Figure 2.7 [137].

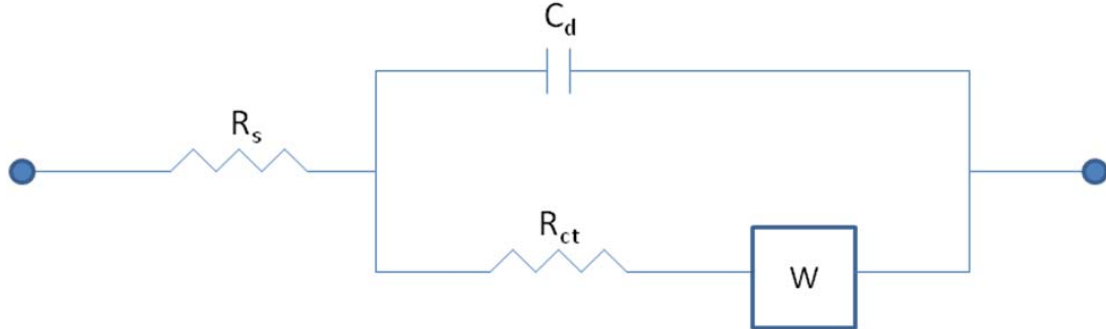


Figure 2.7: Randles equivalent circuit model for the complex impedance of the three electrode system in an ionic solution.

Here, R_s is the solution resistance between the electrodes which is typically much smaller than the other components. R_{ct} is the charge transfer resistance which accounts for the ability of the redox compound to interact with the electrode surface via electron transport. C is the capacitance between the electrode and the charged ions in solution. This capacitance is known as the double layer capacitance which exists between any metal placed in an electrolyte solution. W is an element called the Warburg impedance which accounts for the effects of diffusion in the system. The Warburg impedance itself has both a real and imaginary component and is frequency dependent.

One can calculate the total impedance of this circuit with respect to the values of the components and the frequency as shown in equation 2.6.

$$Z = \left(R_s + \frac{R_{ct} + W}{1 + (R_{ct} + W)^2 \omega^2 C^2} \right) - j \left(\frac{(R_{ct} + W)^2 \omega C}{1 + (R_{ct} + W)^2 \omega^2 C^2} \right) \quad (2.6)$$

Equation 2.6 has been written in the form shown to clearly separate the real and imaginary components of the total impedance. The Warburg impedance W is further given by equations 2.7 and 2.8

$$W = \frac{\sigma}{\sqrt{\omega}}(1 - j) \quad (2.7)$$

$$\sigma = \frac{RT}{n^2 F^2 A \sqrt{2}} \left(\frac{1}{\sqrt{D_{ox} C_{ox}}} + \frac{1}{\sqrt{D_{red} C_{red}}} \right) \quad (2.8)$$

where C_{ox} and C_{red} are the bulk concentrations for the oxidized and reduced forms of the compound respectively and D_{ox} and D_{red} are the diffusion coefficients for the oxidized and reduced forms of the compound respectively. The Warburg impedance has the same magnitude for both of its real and imaginary components, so it constitutes a 45 degree phase shift in the Nyquist plot as will be seen in the simulations. The most critical component in the system is the charge transfer resistance R_{ct} . This value is very sensitive to the addition of biomolecules onto the surface of the electrode as they disrupt the charge transport between the redox compound in solution and the metal. The sensitivity of R_{ct} to the conditions on the electrode surface makes impedance spectroscopy one of the best methods to use for detection of binding events on the surface of the working electrode.

Simulations were performed using the software that came with the CHI660 potentiostat from CH Instruments (Austin, TX). The software allows the user to build an equivalent circuit then plot the Nyquist diagram for a range of applied frequencies.

The circuit in Figure 2.7 was built in the simulation software and the values for R_{ct} and C were varied to observe the change in the Nyquist plot. The value of R_s was set to be 100 Ohms based on measuring the resistance through the phosphate buffer electrolyte using the potentiostat. The Warburg impedance was set to a value of 0.0001 which was also determined through testing based on the use of the

ferro/ferricyanide couple in phosphate buffer electrolyte. Figure 2.8 below displays the Nyquist results for varying the resistor value R_{ct} .

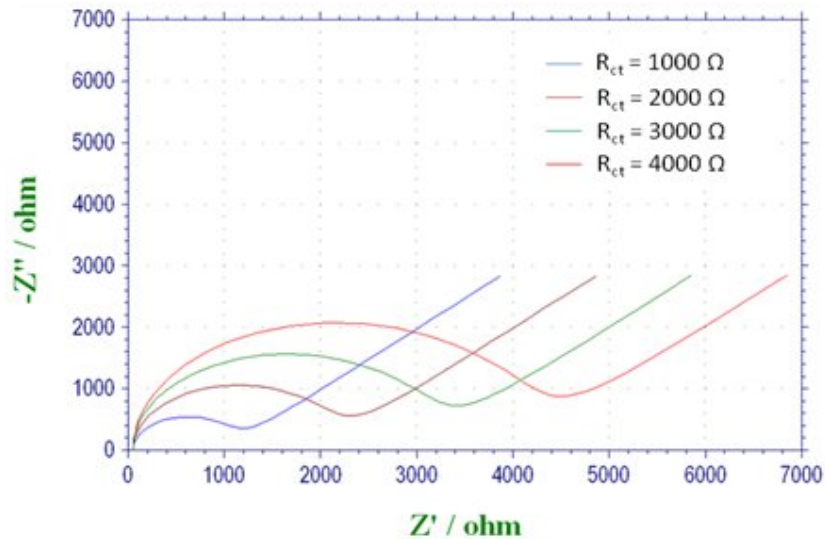


Figure 2.8: EIS simulations performed by varying the charge transfer resistance (R_{ct}).

The capacitance value was set at 100 nF and the frequency sweep was performed from 100000 Hz down to 1 Hz. There are two noticeable regions that exist in the Nyquist plot in Figure 2.8. The first is the semicircle region at high frequencies followed by a linear region at lower frequencies. The semicircle is formed from the effects of the capacitance and the electron transfer resistance while the linear region is due to the Warburg impedance. It is clear from Figure 2.8 that increasing the electron transfer resistance will respectively increase the diameter of the semi-circle. Also, the linear region due to the Warburg impedance becomes smaller as the electron transfer resistance increases. This implies that as the resistance at the electrode surface becomes very large, due to accumulation of biomolecules as an example, the impedance component due to diffusion becomes negligible and the linear portion of the plot at lower frequencies will begin to disappear. The presence of the Warburg impedance still stretches the semicircle further along the real impedance axis for any

simulated value of R_{ct} . If the Warburg impedance were to be neglected completely, then the semicircle arc would have a diameter of exactly R_{ct} .

The capacitance was also varied while the electron transfer resistance remained set at 3000 Ohms with the results shown in Figure 2.9. The frequency for each scan was once again swept from 100000 Hz to 1 Hz. As the capacitance increases, the semicircle becomes lost since more frequencies are able to pass through the larger capacitor which contributes to greater imaginary impedance. As lower frequency signals become blocked by the capacitor, the Warburg impedance begins to dominate and the plot trends upward in a linear fashion at a 45 degree phase angle.

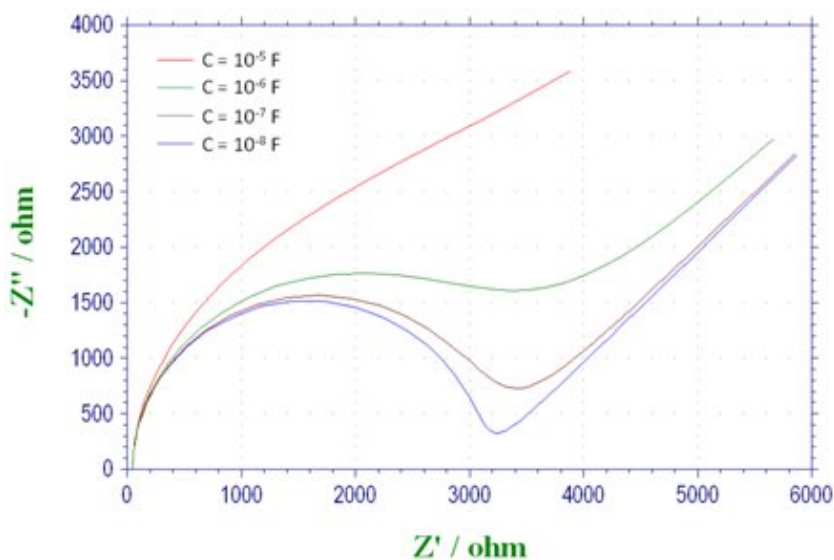


Figure 2.9: Simulated EIS results from a varying double layer capacitance (C).

Lower values of capacitance tend to tighten the semicircle closer to a diameter that exactly matches the electron transfer resistance. Changes to the capacitance are not expected to be as dramatic as changes to the charge transfer resistance when performing both the DNA hybridization and protein adsorption studies. The double layer capacitance is dominated by both the electrode geometry and the ionic strength

of the electrolyte, neither of which should change during the hybridization or adsorption experiments.

2.5 Electrode Configuration and Design

The electrodes of the device perform more than one important function. They act as sites for the specific functionalization of probe molecules and chemical compounds. They are also used to perform the detection itself via electrochemical measurements. This section describes the materials used for the electrodes, their geometry and their arrangement within the microfluidic device.

2.5.1 Electrode Materials

When designing an electrochemistry experiment, the choice of materials for each of the three electrodes can have a significant impact on the results. Both the impact on the measurement itself as well as the compatibility of the material with microfabrication techniques for use in the microfluidic device must be considered.

The working and counter electrodes must be fabricated from an inert metal with high conductivity. Both gold and platinum are the best candidates for these electrodes due to their high conductivity, compatibility with microfabrication techniques, and their high resistance to corrosion. Of the two, gold is chosen to use for this work because it has been reported that the thiols from the DNA will self assemble more readily onto a gold surface [116, 138-140]. Gold also has a relatively high oxidation potential of +1.52 V in comparison to the voltages applied during typical electrochemistry experiments (in the range of -0.5 to 0.5 V). This indicates that the gold will not be oxidized or reduced during the course of the experiment.

The reference electrode is unique in that it must be able to retain its potential regardless of the reaction taking place or the pH of the solution. A list of the most commonly used aqueous reference electrodes is given in Table 2.1. The electrode potentials are given at room temperature and in reference to the standard hydrogen electrode (SHE). The silver/silver chloride electrode is chosen to use for all experiments performed in a beaker for this research due to its low cost and lack of mercury. The reaction between the silver and silver chloride using KCl as an electrolyte keeps the potential of the electrode extremely stable at about +0.223 V.

Table 2.1: List of commonly used aqueous reference electrodes and their potential vs. the standard hydrogen electrode at room temperature.

Name	Formula	Electrode Potential
Silver/Silver Chloride	Ag/AgCl	0.223 V
Saturated Calomel Electrode	Hg/Hg ₂ Cl ₂	0.268 V
Copper/Copper Sulfate Electrode	Cu/CuSO ₄	0.314 V
Silver/Silver Sulfate	Ag/Ag ₂ SO ₄	0.710 V
Mercury/Mercury Oxide	Hg/HgO	0.098 V

The aqueous reference electrodes are very difficult to integrate with a microfluidic device. Each electrode given in Table 2.1 contains a specific liquid electrolyte concentration surrounding the metal in order to maintain a stable electrode potential. Some researchers have reported creating a solid Ag/AgCl quasi-reference electrode for microscale devices by depositing silver and electrodepositing a layer of silver chloride over it [98, 99, 141]. This quasi-reference electrode will have a slightly different standard potential than the aqueous Ag/AgCl electrode and it will not remain stable for nearly as long. Another approach is to deposit a film of platinum to use as a reference electrode. Platinum has a relatively stable potential of +1.188 V and, like

gold, is highly resistant to corrosion [4]. Although platinum's potential can vary over time, the measurements performed in this work will take place within minutes of one another. The variation in platinum's potential does not change significantly in that time. Due to the greater ease of fabrication, platinum is chosen as the reference electrode for the microfluidic devices.

2.5.2 Electrode Geometry and Placement

The placement and size of the three electrodes is an important factor to consider when designing an electrochemistry experiment. Ideally, no current should be flowing through the reference electrode, but in practice a very small parasitic current will exist, so it is best to minimize the potential drop between the working and reference electrodes. This is achieved by placing the reference close to the working electrode to minimize the solution resistance between them. For the experiments performed in the microfluidic channels, the distances between the reference electrode and the various working electrodes has a very minimal effect on the measurement since they are all small to begin with (on the order of millimeters).

More important than the spacing of the electrodes is the size of the counter electrode compared to the working electrode. The counter electrode should have an exposed surface area larger than that of the working electrode. This is done to minimize the impedance contributions of the counter electrode. The system through which current flows between the counter and working electrodes can be roughly modeled using the circuit shown in Figure 2.10.

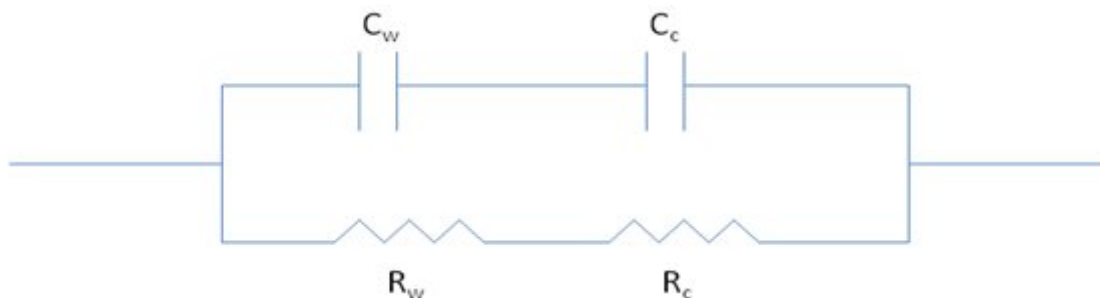


Figure 2.10: Circuit model for the current flow between the working and counter electrodes.

The components R_w and R_c are the resistance of the working and counter electrodes respectively. The components C_w and C_c are the capacitance of the working and counter electrodes respectively. This schematic is not taking into account any solution resistance and the effects of diffusion which were modeled in Figure 2.7. Since the reaction of interest is only occurring at the working electrode, only the resistance and capacitance of the working electrode are relevant. The resistance of the counter electrode is reduced by increasing its area thus maximizing the contribution of the working electrode to the total resistance. Conversely, the capacitance of the counter electrode is increased by increasing the area. Since capacitors in series add like resistors in parallel, the smallest capacitor dominates the total capacitance, which in this case, will be from the working electrode. The larger counter electrode increases the sensitivity of the electrical measurement being performed at the working electrode. The size of the reference electrode does not impact any of these values and is typically not considered.

For the microfluidic device, the gold counter electrode will fill a portion of the channel while the working electrode is disk shaped. After the integration with microvalves, the working electrodes each lie at the intersection between perpendicular channels. The working electrode uses a circular shape in order to avoid

sharp corners. These corners can cause fringing effects which intensify the strength of the electric field near them and will cause a non-uniform concentration gradient of the redox compound above the whole electrode surface. The working electrodes are spaced out to provide surfaces for functionalization of probes or other compounds in one flow direction and incubation with different target biomolecules in the other flow direction. The reference electrode is placed at the end of the channel. The configuration for a device containing 9 sensors in a 3 x 3 grid is shown in Figure 2.11. Note that in this diagram, the light blue layer is the elastomer PDMS and both channel orientations (horizontal and vertical) are displayed.

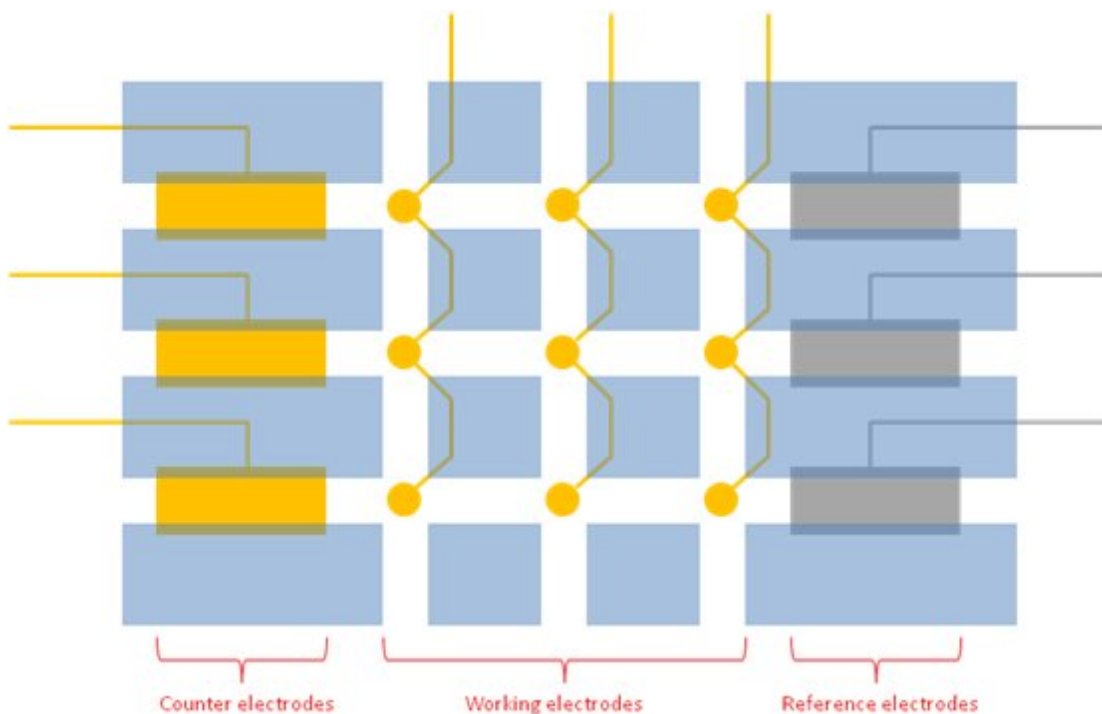


Figure 2.11: Top-down schematic of the electrode configuration in the microfluidic device containing 9 total sensors. The blue areas correspond to bonded PDMS with the substrate. Both channel orientations are overlaid to show both vertical and horizontal paths.

From the figure, it can be seen how the working electrodes are linked in a column to reduce the number of contact pads needed. The number of contacts needed to measure from each sensor is reduced from 9 to 3. The linking of the electrodes

reduces the number of necessary contacts by a factor of N for a sensor array of $N \times N$. This design becomes especially important for scaling the device up for future iterations to include a higher number of sensors. The configuration will be effective as long as the redox compound is only present in one channel at a time.

Each working electrode has a radius of 100 μm . This size is determined based on the designed size for the microfluidic channels discussed in the next section. The electrodes could be designed smaller to increase the sensitivity to binding affinity; however, this also increases the noise and reduces the magnitude of the current output. Smaller sizes of electrodes were not explored in this research since the goal was not to obtain the most sensitive result but to demonstrate arrayed sensing using electrochemical techniques.

2.6 Microchannel design

The microfluidic channels are designed to provide three parallel flow paths over the sensor array. The cross sectional dimensions of the channels are 500 microns wide by 100 microns tall and are chosen to align easily by eye over the electrodes. Much greater design considerations must be made when integrating valves with the system since the integration requires new channel geometries to function properly. The rest of this section will focus on the design of the two-layer valving integration.

The microfluidic and valve channels are designed to work in conjunction with one another. Using two layers of PDMS to create microfluidic channels and pneumatic valves has been previously reported by many groups and was pioneered by Quake *et al.* [142, 143]. Briefly, microfluidic channels are patterned in a thin layer of PDMS while a second set of pneumatic channels are patterned in a thicker layer of

PDMS and aligned over the microfluidic channels. The stack of two PDMS layers are cured together and bonded to a substrate. Each intersection between the two channel layers acts as a valve when pressure is applied as shown in the Figure 2.12 schematic.

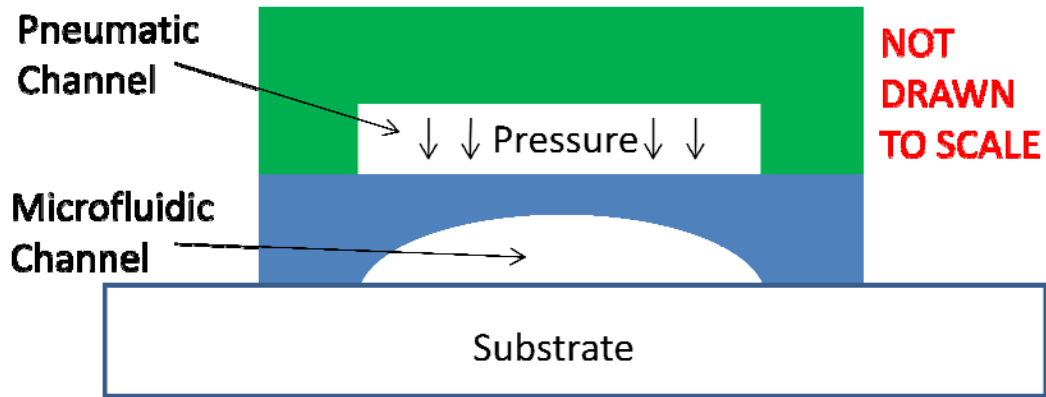


Figure 2.12: Schematic demonstrating valve actuation using pneumatic channel to pinch off the microfluidic channel below.

The microfluidic channels contain 3 vertical and 3 horizontal channels crossing in a tic-tac-toe pattern. The valve channels are designed to align over the microfluidic channels to shut off sections that form either the three horizontal or the three vertical channels with no leakage between them. This concept is displayed below in Figure 2.13.

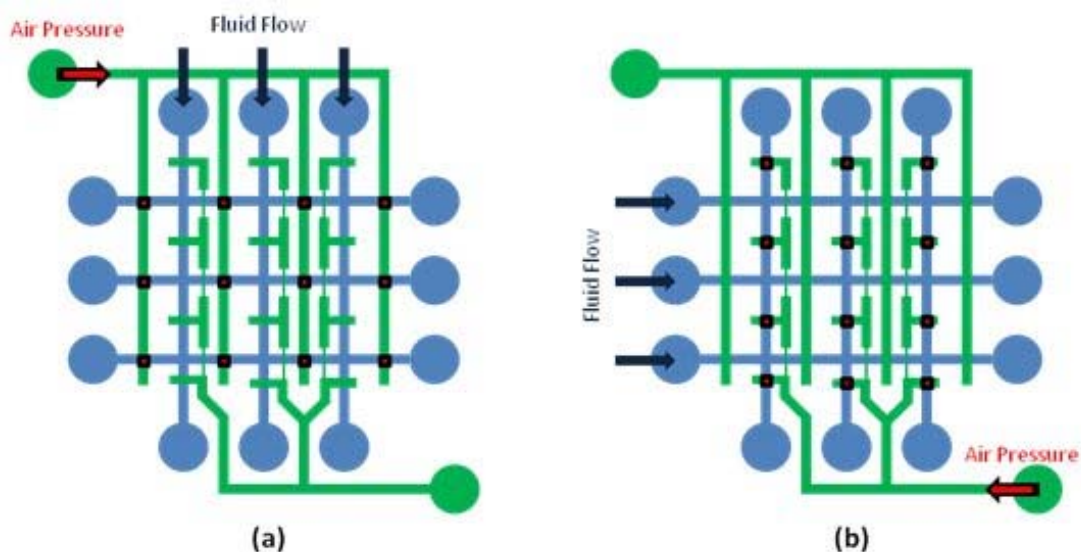


Figure 2.13: Overhead layout of microfluidic channels (blue) and pneumatic valve channels (green). In (a) pressure is applied to the top valve inlet and valves are closed to create vertical fluid channels. In (b) the pressure is applied to the bottom inlet and three horizontal fluid channels are created.

The pneumatic channel layer is designed to be able to close multiple valves with only two pressure inlets, one for controlling each fluid flow direction. The width of the pneumatic channel is made much thinner than the width of the microfluidic channel in certain areas to allow crossing of the two channels without closing off the bottom microfluidic channel. The details on the fabrication for each PDMS layer can be found in Chapter 3. The following subsections focus on the design aspects for both channel layers although many of the dimensions chosen are not critical to the operation of the device.

2.6.1 Valved Microfluidic Channel Design

The dimensions of the microfluidic channels in the device will have an effect on the valve sealing efficiency and the pressure in the channel. Each of these aspects is considered in choosing the width, height and overall shape of the channel.

Sufficient sealing from the PDMS membrane above the channel has been commonly reported in literature for heights under $\sim 35 \mu\text{m}$ [143, 144]. More important than the height is the shape of the channel. Rectangular channels do not seal effectively as the sharp corners make it difficult for the PDMS to press tightly along all parts of the channel walls. Rounded channels have been demonstrated to be highly effective in forming a tight seal even at fairly low actuation pressures of 40 kPa [143]. Rounded channel molds can be formed by first patterning a photoresist to create rectangular shapes, then subjecting the mold to a high temperature in order to reflow the photoresist and round the edges. Specific fabrication details are found in Chapter 3.

The pressure in the channel is directly proportional to the cross-sectional area, with smaller areas resulting in higher channel pressures. If the channel pressure is too high, it may cause the PDMS to de-bond from the substrate. The pressure for a given length in a channel is given by Poiseuille's Law in Equation 2.9.

$$\Delta P/L = \frac{128\nu Q}{\pi d^4}, \quad d = \frac{4A}{U} \quad (2.9)$$

Where ν is the fluid viscosity, Q is the volumetric flow rate and the term d is given by the cross sectional area of the channel, A , and its perimeter, U , for a non-circular area. From the equation, it is clear that the area of the channel has a dramatic impact on the pressure differential along its length. Higher flow rates will also increase the pressure.

To calculate the area of the rounded microfluidic channel, it is treated as a circular segment as shown below in Figure 2.14 with the accompanying equations for determining the area.

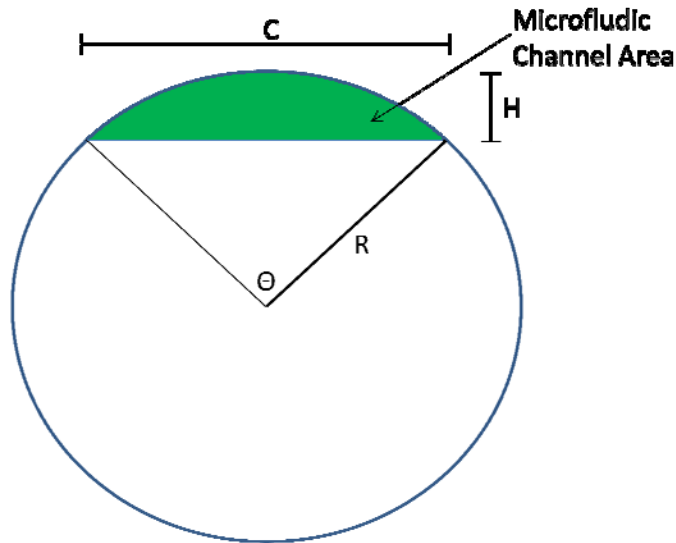


Figure 2.14: Geometry used for calculating the area of the rounded microfluidic channels.

$$A = \frac{R^2}{2} (\theta - \sin\theta) \quad (2.10)$$

$$R = \frac{H}{2} + \frac{C^2}{8H} \quad (2.11)$$

Channels were chosen with a width of 300 μm and a height of 32 μm . The width was chosen based on intuition to allow adequate alignment over patterned electrodes on the substrate by eye and the height is chosen based on fabrication parameters discussed further in Chapter 3. With these dimensions, equations 2.10 and 2.11 are used to determine the cross sectional area of the channel to be 6458 μm^2 . Assuming the viscosity of water and a flow rate of 200 $\mu\text{l/hr}$ (a commonly used flow rate for microfluidic applications), equation 2.9 is used to determine that the pressure along the channel is 0.705 Pa/ μm . For a given device channel length of 2 cm, the pressure difference along the channel is calculated to be 14.1 kPa. This pressure is well below the bond strength of PDMS to a glass substrate which ranges from 200 to 500 kPa or to silicon dioxide which was found to be about 70 kPa [145].

The microfluidic channels are aligned over the electrode network so that an electrode lies in each intersection as mentioned previously. Although 300 μm is an adequate channel width for aligning a single electrode with a radius of 100 μm , it proved almost impossible in practice to align all 9 electrodes simultaneously. Figure 2.15a and 2.15b illustrate the problem with microscope images taken from two electrodes in the same device after bonding the channels.

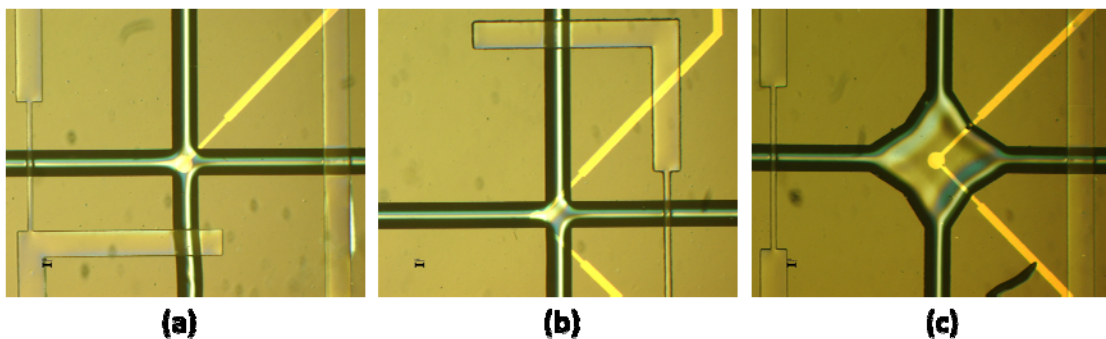


Figure 2.15: Microscope images showing channel alignment over the patterned electrodes. Both good alignment (a) and bad alignment (b) were observed in the same device. The new channel cross section design is shown in (c) to provide more alignment tolerance. All scale bars are 100 μm .

Further widening of the channels would cause a larger valve surface area which could droop low enough to touch the substrate and permanently close the valve upon bonding. The misalignment of the electrodes is caused by both the inherent elasticity in the PDMS itself and the translational misalignment that occurs in the printed transparency masks used to create the patterns. This problem was solved by creating a larger fluidic chamber at each intersection to reduce the effect of electrode misalignment as shown in Figure 2.15c.

This larger chamber at each intersection serves another important purpose as well. It was found during fluid flow testing in these channels that the stream moving in one direction would rarely fill the perpendicular channels when the valves were closed. This creates a liquid-air boundary that is prone to evaporation. The boundary is displayed graphically in Figure 2.16 below.

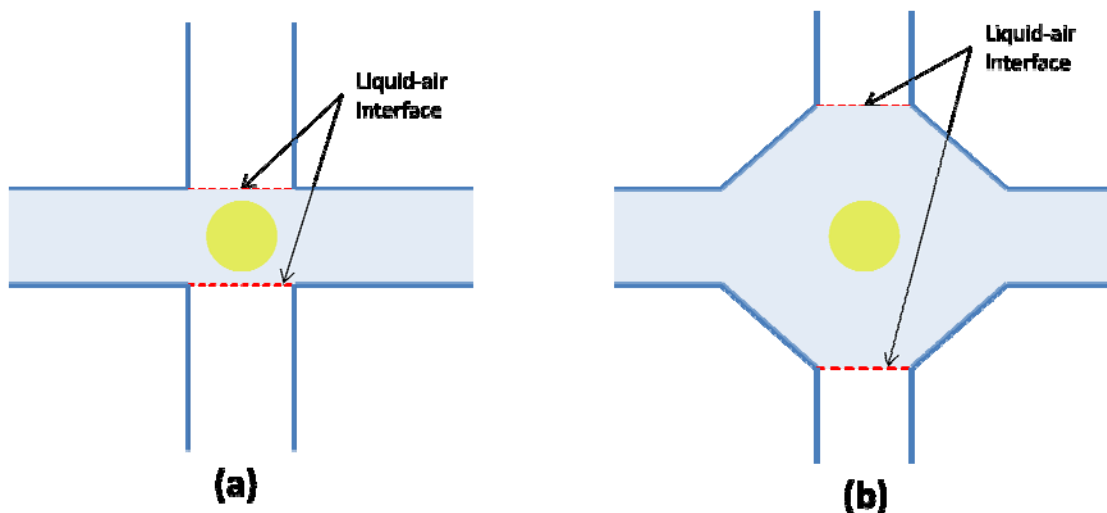


Figure 2.16: Fluid flow through the older (a) and updated (b) microfluidic channel design when using valves. The liquid-air interface is moved further away from the electrode in (b) which reduces problems with evaporation.

By increasing the chamber dimensions, the liquid-air interface is moved further away from the electrode. This minimizes the effects of evaporation at this interface which can pull the solution away from the electrode disrupting biomolecule

assembly and changing the exposed surface area during an electrochemical test. Although the larger chamber size also increases the surface area of the exposed working electrode (since the leads are further exposed), it is still much smaller than the surface area of the counter electrode and is an acceptable trade-off to minimize the evaporation problem.

2.6.2 Pneumatic Valve Channels

The channels formed to create pathways for the pressurized air have no critical dimensions, except for the areas that overlap the microfluidic channels below them. The channels are fabricated to be 100 μm in height and have a rectangular profile with a width of 300 μm , the same width as the microfluidic channels. This provides valve areas consisting of 300 x 300 μm sections above the microfluidic channel.

When considering the sealing efficiency of the valve, the applied pressure, area of the membrane, thickness of the membrane and material constants must all be taken into account. The deflection of the center of an elastic membrane due to a pressure difference has been derived by He et al. and is given in Equation 2.12 [146].

$$\delta = \frac{3(2+\lambda)R^2P}{16\pi\mu(1+\lambda)h^3}, \quad \lambda = \frac{\lambda}{\mu} \quad (2.12)$$

,where R is the radius of the membrane, P is the pressure difference across the membrane, h is the thickness of the membrane and both λ and μ are Lamé constants for an elastic material. Although this equation has been derived for a circular membrane, the same principal applies to the case for a square one. Larger areas, higher pressures and thinner membranes all contribute to greater deflection. The area

of the valve is determined by the width of the microfluidic channel (300 μm) and the pressure can be increased up to the bond strength of the PDMS to the substrate. The thickness of the membrane can be carefully controlled depending on the fabrication parameters used for the microfluidic channel layer and are discussed in detail in Chapter 3.

2.7 Summary

This chapter has described the design of each component of the device. The hybridization of DNA and a brief overview of protein adsorption kinetics were discussed. An overview of the operation of the device including the manipulation of the cross-channel design to perform an array of binding assays was explained. Both cyclic voltammetry and impedance spectroscopy measurements were performed with the device using a micro-patterned three electrode system with platinum as the reference electrode and gold for both the working and counter electrodes. Simulations provided qualitative changes to be expected for biomolecule assembly for both CV and EIS. Changes to the microfluidic channel dimensions were designed to be able to include a second layer of valve channels overlaid on top. The dimensions were chosen based on literature values to ensure good sealing and adequate bond strength to the substrate.

3 Device Fabrication

3.1 Introduction

This chapter will cover the fabrication procedure for every stage of device design. The designs were fabricated over the course of this research in 4 main stages.

- (1) Macroscale (1 mm diameter) electrodes to be used in a beaker of solution
- (2) Microscale electrodes in close proximity so that a droplet of the electrolyte containing the redox compound can be used for testing.
- (3) A microscale electrode array on a chip that includes microfluidic channels but no active valves.
- (4) A microscale electrode array on a chip including microfluidic channels and valves.

Each of these four designs will be referenced throughout the chapter. The chip fabrication process is described in the first section, followed by the PDMS channel fabrication and finally the bonding and packaging of the devices are explained.

3.2 Chip Fabrication

Both glass and silicon dioxide were used as substrates for the patterning of all the chips in this research. Specifically, the chips were fabricated on either 4” Borosilicate glass wafers (Promptar, CA) or 4” silicon wafers (Silicon Quest, CA) with 1 μm of PECVD silicon dioxide deposited on the surface. Each of these substrates provides insulation for the patterned electrodes and also a prime surface for bonding the PDMS layers which will be discussed in more detail later in the chapter.

All of the design stages require the patterning of gold while only stages 2-4 require platinum patterning. The second stage to be used for the droplet tests also




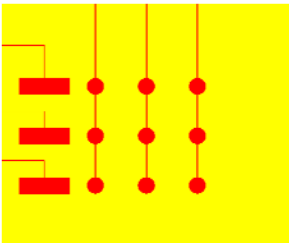
includes a patterned ring of SU-8 5 surrounding the electrodes to create a hydrophobic surface and keep a droplet contained over the electrodes. The parameters used to perform each of these steps for all of the chips are discussed here.

3.2.1 Metal Patterning

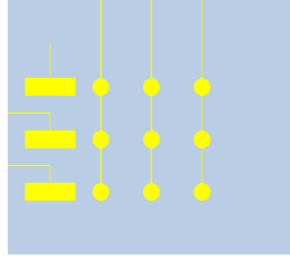
Both gold and platinum are used as the electrodes in the device. The gold is deposited first over the wafer, and patterned using photolithography and wet chemical etchant. The platinum is patterned using a metal lift-off process. Both metal patterning processes are traditional microfabrication techniques.

The process flow for the metal patterning steps is shown graphically step-by-step in Table 3.1. The first chip design only requires steps 1-3 of this process while the other 3 designs use all of the steps shown. Note that the pictures depict only the design of the arrayed sensors. Specific parameters and discussion for each of the process steps are given afterwards.

Table 3.1: Process flow of metal patterning steps for all design stages.

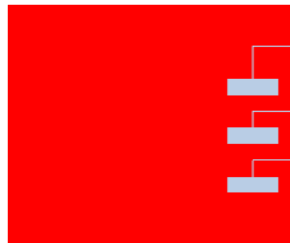
Side View	Top View	Description
(1) 		Begin with a 4" wafer. Sputter 20 nm of chrome, followed by 200 nm of Gold.
(2) 		Deposit and pattern photoresist in order to define the features for the gold electrodes.

(3)



Etch the exposed gold and chrome using Transcense etchants. Remove the photoresist with acetone.

(4)



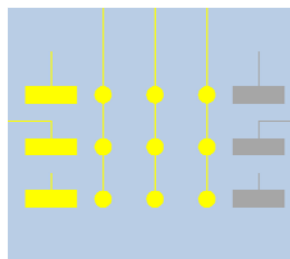
Deposit and pattern photoresist on the wafer to define areas for the platinum electrodes (lift-off process)

(5)



Evaporate 200 Å of titanium followed by 2000 Å of platinum.

(6)



Remove the photoresist with acetone, lifting off the platinum with it.

The gold has poor adhesion on its own to both glass and silicon dioxide substrates. A thin layer of chrome is first deposited under the gold to act as an adhesion layer. The processing parameters using a JEOL AJA sputter machine in the

Fablab at the University of Maryland for depositing the Cr/Au are given below in Table 3.2.

Table 3.2: Parameters used for sputtering Cr/Au onto the wafer.

	Chrome	Gold
Chamber Pressure	10 mTorr	10 mTorr
Argon Flow Rate	20 sccm	20 sccm
Supplied DC Power	200 W	200 W
Sputter Rate	10 nm/min	36 nm/min
Final Thickness	20 nm	200 nm

After the Cr/Au deposition, Shipley 1813 positive photoresist is spun across the wafer and used to pattern the gold electrodes. The parameters for the lithography process are given in Table 3.3.

Table 3.3: Table of processing steps and parameters for patterning the Cr/Au electrodes.

Step	Parameters	Description
Spin Photoresist	3000 RPM, 30 sec	Achieves thickness of 1.6 μm across the wafer
Bake	100 °C, 60 sec	Evaporates solvent from resist
Expose	190 mJ/cm ² @ 405 nm	Expose resist using Mask (Appendix B)
Develop	30 sec	Use Microposit 351 developer, rinse with DI water afterwards
Etch Au	2 min, mild agitation	Etch exposed gold using Au etchant
Etch Cr	30 sec, mild agitation	Etch exposed chrome using Cr etchant
Strip Photoresist		Rinse with acetone, methanol, isopropanol alcohol (IPA)
Clean Wafer	1 minute	Piranha clean with 4:1 H ₂ SO ₄ : H ₂ O ₂

The various masks used to pattern the gold for the different stages of the device design are given in Appendix B. Each mask is printed on a transparency sheet, and taped onto a 5" x 5" glass plate to use with a contact mask aligner. The masks are designed in the program L-edit and printed with a minimum resolution of 5080 dpi from the company Pageworks in Cambridge, MA.

After the Au/Cr pattern step, the first design stage consisting of chips patterned using Mask 1 in Appendix B is complete and the chips can be individually cleaved from the wafer for use. These chips include circular working electrodes and a large gold counter electrode to be used for electrochemical testing in a beaker. The chips are shown in Figure 3.1. The other three chip designs (chips for droplet tests, chips for arrayed sensing in straight microfluidic channels, and chips for arrayed testing using valved microfluidic channels) used masks 2-4 in Appendix B to pattern the gold electrodes.

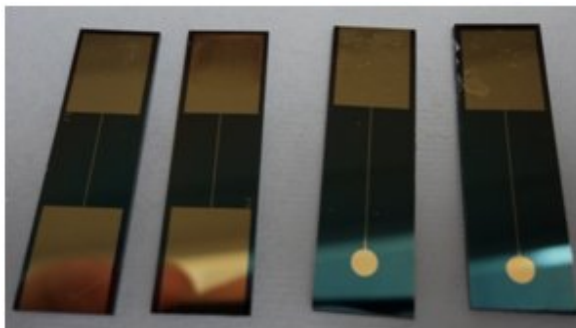


Figure 3.1: Photograph of patterned macroscale chips. Left two chips are counter electrodes while right two are working electrodes.

All of the designs except for the first utilize a patterned platinum reference electrode. Like gold, platinum has poor adhesion to either glass or silicon dioxide. A thin layer of titanium is deposited first under the platinum to promote better adhesion. The Ti/Pt is patterned using a conventional metal lift-off process. An image reversal photoresist, AZ5214, is spun across the wafer and developed with the procedure

shown in Table 3.4. Either one of masks 5-7 in Appendix B are used to pattern the photoresist depending on which design is currently being fabricated.

Table 3.4: Processing parameters for AZ5214 photoresist.

Step	Parameters	Description
Spin AZ5214 Photoresist	3000 RPM, 30 sec	Achieves thickness of 1.4 μm across wafer
Bake	100 °C, 60 sec	Evaporates solvent from resist
Expose	30 mJ/cm ² @ 405 nm	Expose resist using either mask 5-7 (Appendix B)
Bake	125 °C, 45 sec	Post bake step
Flood Expose	1000 mJ/cm ² @ 405 nm	Expose across whole wafer (no mask)
Develop	6:1 AZ400K, 120 sec	Develop patterned regions

Once the photoresist has been patterned, 40 nm of Ti followed by 160 nm of Pt are deposited across the wafer using a Denton E-beam evaporation system from the Fablab at the University of Maryland. The wafer is then placed in an ultrasonicated acetone bath for 5 minutes to completely lift off all of the underlying photoresist and leave behind the patterned platinum features.

At this point, the third and fourth chip designs are complete and they can be cleaved from the wafer. If the pattern is made on a glass substrate, then the chips must be carefully diced out using a dicing saw. Photographs for both chip designs are shown below in Figure 3.2.

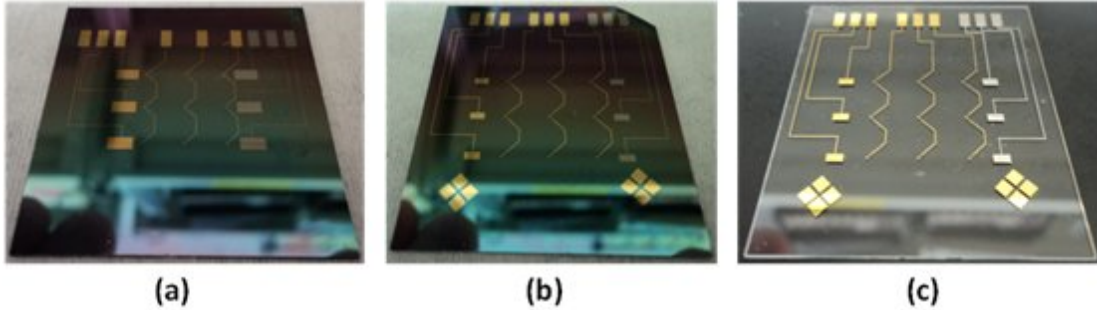


Figure 3.2: Photographs of completed chips for the microfluidic design without valves on silicon dioxide (a), and the design with valves on both silicon dioxide (b) and glass (c).

3.2.2 SU-8 5 Patterning

The second design used for droplet testing requires an additional chip fabrication step. In order to effectively confine the droplet of solution, a thin polymer material is patterned in a ring around the patterned electrodes. Many polymers are hydrophobic which will stop the spreading of the droplet and keep it in place over the electrodes. SU-8 5 resist (Microchem, MA) is chosen for this step since it can be easily spun to low thicknesses, is chemically resistant, and has a contact angle of around 99 degrees [147]. The procedure for the patterning of the SU-8 5 is shown below in Table 3.5.

Table 3.5: Processing parameters for SU-8 5.

Step	Parameters	Description
Spin SU-8 5 resist	500 RPM, 5 sec Ramp: 10 sec 5200 RPM, 30 sec	Achieves thickness of 2.2 μm across wafer
Soft Bake	95 $^{\circ}\text{C}$ Ramp: 300 $^{\circ}\text{C}/\text{hr}$ Time: 16 min	Let wafer cool afterwards to 50 $^{\circ}\text{C}$
Expose	200 mJ/cm^2 @ 365 nm	Expose resist using mask 8 (Appendix B)
Post Bake	Same as Soft Bake	Hardens features
Develop	SU-8 Developer, 120 sec	Clean with IPA following development

After the wafer is cleaned, the individual chips for droplet testing can be cleaved from the wafer and are shown below in Figure 3.3. A microscope image of the patterned sensors within the SU-8 ring is shown in Figure 3.4.

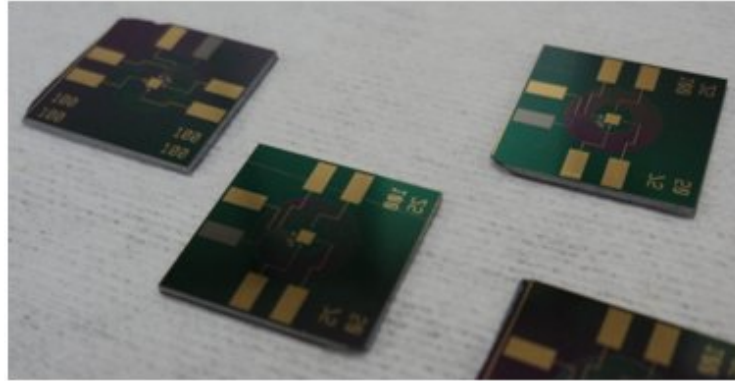


Figure 3.3: Photograph of chips used for droplet tests.

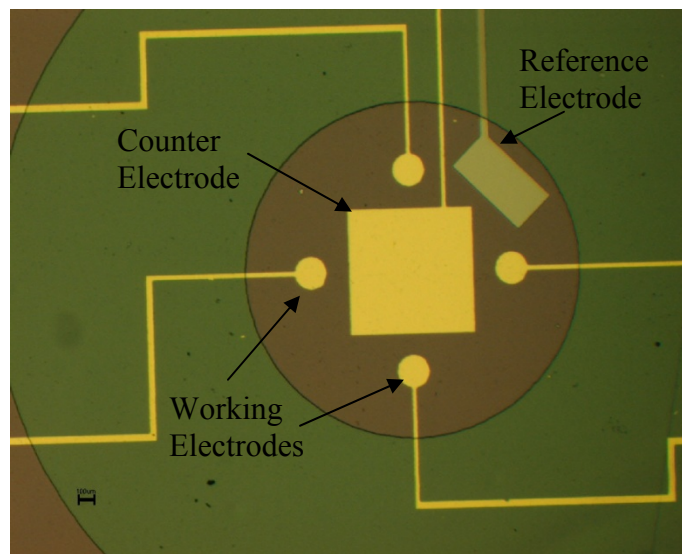


Figure 3.4: Microscope image of droplet sensor chip containing 4 working electrodes, 1 counter electrode and 1 reference electrode patterned within a ring of SU-8.

3.3 PDMS Processing

Polydimethylsiloxane (PDMS) is used to create all of the microfluidic channels in this work. Briefly, the material consists of an elastomer and curing agent mixed in a specific ratio and cured in an oven over a molded surface. The mold contains the pattern for the channel design. After curing, the PDMS can be removed

from the mold and bonded to the previously fabricated chip to complete the device. This section describes the process used to make each of the molds as well as the steps taken for preparing the PDMS.

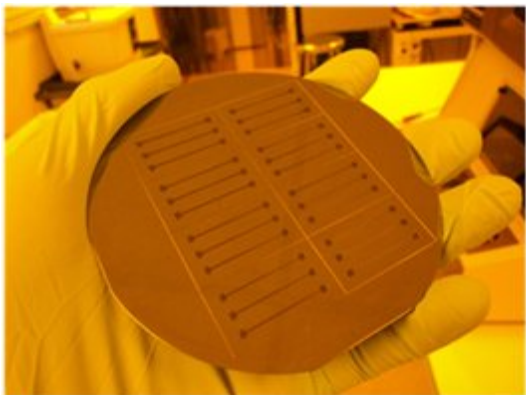
3.3.1 SU-8 50 Mold Fabrication

The resist SU-8 50 (~100 microns thick) was chosen to fabricate molds for both the microfluidic channels used with chip design 3 as well as the valve channels for the final chip design. The SU-8 is patterned on a blank 4" silicon wafer. The condition of the wafer surface is very important in order to successfully peel the PDMS away after it has cured. It was found during the fabrication of numerous molds that silicon wafers of test grade quality had surfaces which demonstrated great affinity to the PDMS and made it nearly impossible to separate the two. Prime grade silicon wafers did not share this problem. It is hypothesized that this may be caused by inadequate polishing of the test grade wafers vs. the more carefully prepared prime grade. Other wafer surfaces beyond bare silicon could be used as well for the substrate, but the SU-8 recipe would have to be optimized to promote better adhesion.

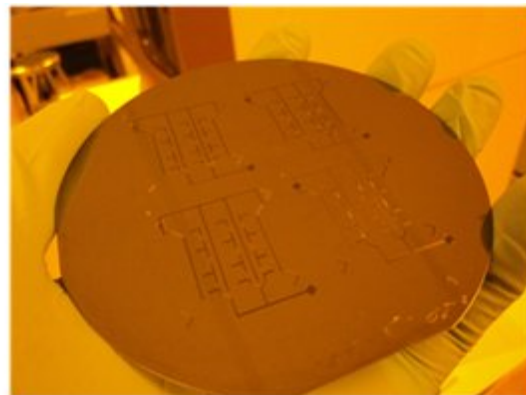
The processing parameters used for the SU-8 50 are shown in Table 3.6. A ramped cooling step down to room temperature is recommended after each heating step to reduce any stress cracking in the SU-8 due to the coefficient of thermal expansion (CTE) mismatch between the polymer and the silicon substrate. Small cracks can be filled by the pre-cured PDMS and cause tearing when trying to peel the cured PDMS away from the mold. Photographs of the completed SU-8 molds are shown in Figure 3.5.

Table 3.6: Processing parameters used for SU-8 50 on silicon.

Step	Parameters	Description
Spin SU-8 50	600 RPM Ramp: 5 sec Time: 10 sec 1150 RPM Ramp: 3 sec Time: 27 sec	Spin parameters used to create uniform film ~ 100 μm thick
Pre-Bake	65 °C Ramp: 300 °C/hr Hold Time: 10 min 95 °C Ramp: 300 °C/hr Hold Time: 30 min	Used to evaporate solvent. Let wafer cool to room temp afterwards
Exposure	2500 mJ/cm^2 @ 405 nm	Expose using Mask 9 or 10 (Appendix B)
Post-Bake	95 °C Ramp: 300 °C/hr Hold Time: 10 min	Crosslinks resist. Let wafer cool to room temp afterwards
Develop	10 min, agitation	Develop in PGMEA developer. Rinse with IPA afterwards



(a)



(b)

Figure 3.5: Completed SU-8 molds for (a) straight microfluidic channels and (b) valve channel network.

3.3.2 AZ9260 Mold Fabrication

The microfluidic channels in the final device design are designed to have a height that lies anywhere in the range of 25 to 35 microns. This is to ensure leak-proof sealing by the valves as discussed previously. Also discussed is the rounded cross section for these channels. The photoresist AZ9260 has the ability to be spun in multiple layers to produce heights ranging anywhere from 10 to 80 microns. Furthermore, it has been shown in literature that it can be rounded by heating to its glass transition temperature after development [148].

A 4" silicon wafer was used for the substrate and an adhesion promoter HMDS (Dow Corning, MA) was first spun to promote better adhesion between the silicon and the AZ9260. In order to achieve thorough development of the UV-exposed areas of the photoresist, the AZ9260 must be adequately hydrated prior to exposure. This hydration process is necessary to activate areas of the UV-exposed polymer chains with water molecules thus making the area soluble to the developer. During the course of this research, the hydration time would change based on the relative humidity present in the cleanroom where the lithography process took place. In the summer months, the high humidity (40% – 70%) caused the wafer to adequately hydrate within 15 minutes after the spinning process. In the winter months, the humidity dropped to extremely low levels (5% - 15%) and the wafer would need to be exposed to the air for at least 24 hours after the spinning process. The hydration of the photoresist is also important for achieving a well-rounded profile when reheated to the glass transition temperature.

The processing parameters used for ultimately achieving a height of 32 microns are shown below in Table 3.7. The development time is longer than what is suggested by the manufacturer to completely dissolve away residues that remain behind due to the use of a transparency mask. The transparent regions on the mask are slightly translucent and speckled which interrupts the UV exposure of the underlying resist. Care must be taken to not leave the wafer too long in the 3:1 AZ400k developer mixture as it will begin to dissolve the pattern away over time.

Table 3.7: Processing parameters for AZ9260 lithography and rounding.

Step	Parameters	Description
Spin HMDS	3000 RPM, 30 sec	Adhesion layer, let sit on wafer 60 sec before spin
Spin 1st Layer	2400 RPM Ramp: 3 sec Time: 60 sec	Creates film ~11 μm
Bake	110 °C, 80 sec	Evaporate solvent
Spin 2nd Layer	2100 RPM Ramp: 3 sec Time: 60 sec	Creates final film thickness ~24 μm
Bake	110 °C, 210 sec	Evaporate solvent
Rehydration	15 min - 24 hr	Rehydration time based on humidity
Exposure	1200 mJ/cm ²	Exposing with Mask 11 (Appendix B)
Develop	4:1 AZ400k 10 min 3:1 AZ400k 5 min	Two step development process removes all residues
Rounding	115 °C, 90 sec	Profile rounded on hotplate

Both a microscope and a Dektak 6M contact stylus profilometer (Veeco, NY) were used to confirm the rounding of the AZ9260 photoresist. Figure 3.6 below

displays both the optical images and profiles before and after the rounding procedure. The bending of the light through the curved surface is observed in the microscope images while the profilometer scan also gives the final height of the resist. The height increases from $23.6\ \mu\text{m}$ to $32.8\ \mu\text{m}$ after rounding.

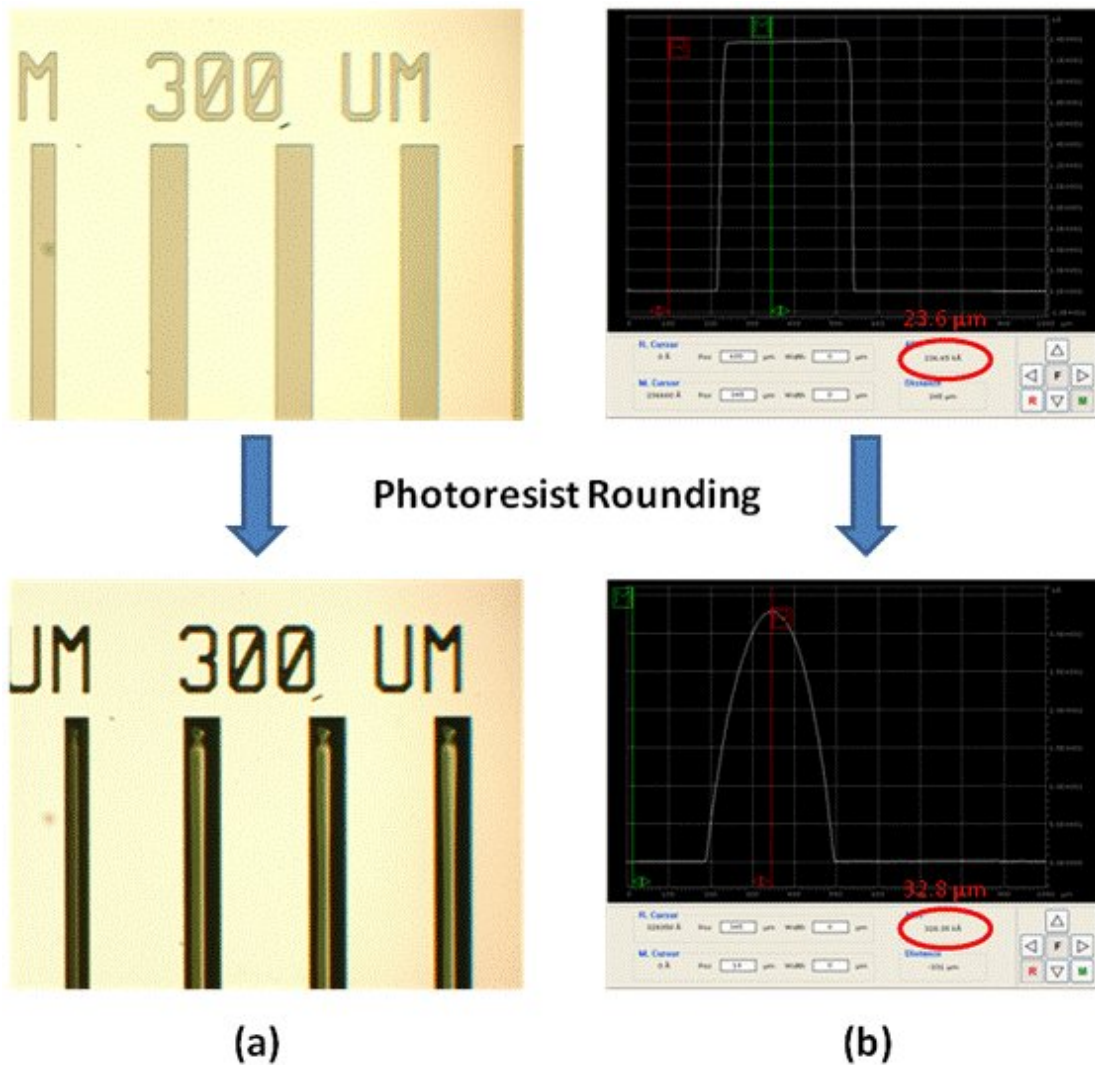


Figure 3.6: (a) microscope images and (b) profilometer scans of AZ9260 photoresist before and after the rounding procedure. Notice the increase in height of the resist from $23.6\ \mu\text{m}$ to $32.8\ \mu\text{m}$ after rounding.

Once all of the lithography steps are performed, the mold requires a release agent to be evaporated across the whole wafer. During initial testing of these molds, it was found that the PDMS would commonly stick too strongly to the mold wafer

which could cause tearing of the thin PDMS layer upon peeling it off the mold or delamination from the second layer of PDMS on top.

Two materials have been demonstrated in literature for the purpose of providing a non-adhesive surface for PDMS-mold separation. These are trimethylchlorosilane [142, 143] and tridecafluoro-(1,1,2,2-tetrahydrooctyl)-1-trichlorosilane [149-151]. Both compounds work by covering the mold wafer with chlorosilane (Si-Cl) groups which do not adhere to the exposed siloxane (Si-O) groups of the PDMS. Ultimately, trimethylchlorosilane (Gelest, PA) was chosen due to cost considerations.

The AZ9260 mold wafer was placed into a vacuum desiccator box with the surface facing downward. A small dish with a few drops of trimethylchlorosilane was placed underneath. The desiccator box was closed and a vacuum pump was used to bring the pressure inside down to -27 inches of Hg. The wafer was left in this environment for 1 hour to let the trimethylchlorosilane evaporate completely over the surface. Trimethylchlorosilane should only be opened and handled under a fume hood, since inhalation of even a small amount can be very harmful. Afterwards, the box was purged with nitrogen and the wafer was removed and ready to be used as a PDMS mold for the microfluidic channels. The trimethylchlorosilane was stored under inert nitrogen inside the desiccator box until further use. A photograph of the completed AZ9260 mold wafer is shown in Figure 3.7.

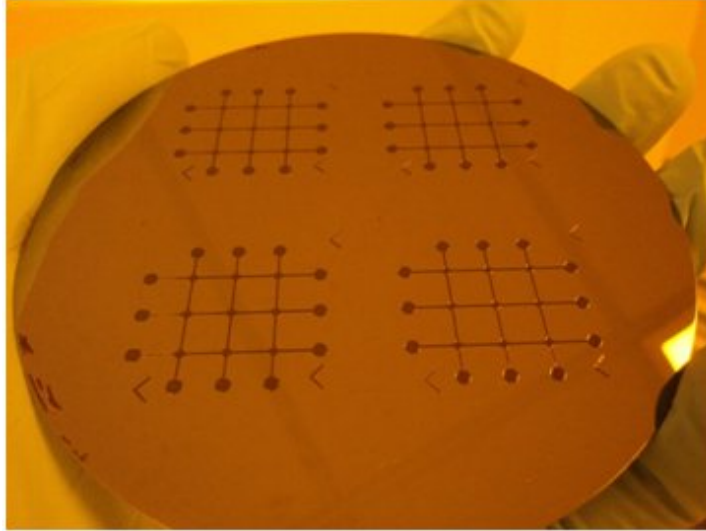


Figure 3.7: Photograph of the completed AZ9260 mold wafer.

3.3.3 PDMS processing parameters

Three different formulations of PDMS were mixed to create the various channels used in this work. Elastomer to curing agent ratios of 5:1, 10:1 and 20:1 were employed. Also, a different fabrication procedure is used whether a single layer or two layers of PDMS are being fabricated. These details are discussed further here.

3.3.3.1 *Single layer PDMS process*

A single layer of PDMS is fabricated to create linear microfluidic channels using the mold displayed earlier in Figure 3.5a. The ratio of PDMS elastomer to the curing agent is 10:1. Specifically, 20g of elastomer and 2g of curing agent are mixed together in large weighing pan then placed in a vacuum bell jar to completely degas the mixture for 20 minutes. An enclosure is made around the mold wafer in aluminum foil and the uncured PDMS is slowly poured over the mold. The mold is then placed in a box furnace with a program set to cure the PDMS at 80 C for 17 minutes with a 5 minute ramp up to 80 °C from room temperature. After curing, the PDMS can be

peeled away from the mold and each individual piece can be cut out using a razor blade. The pieces of PDMS are between 2-3 mm thick.

3.3.3.2 Dual-layer PDMS process

Two distinct PDMS processes are used to create the dual layer PDMS stack consisting of microfluidic channels and valve channels. The microfluidic channels are formed using the AZ9260 mold shown earlier in Figure 3.7. The PDMS is spun over this mold to produce a thin, uniform layer of PDMS covering the wafer. The curing ratio for the spun PDMS is 20:1 elastomer to curing agent which creates a less viscous material for spinning. The thickness of the spun PDMS will determine the thickness of the valve membrane over the microfluidic channel. Thus, it is important to tune the spinning parameters to achieve the desired thickness. Figure 3.8 below displays the final PDMS thickness measured with a profilometer for different RPM speeds for a time of 90 seconds.

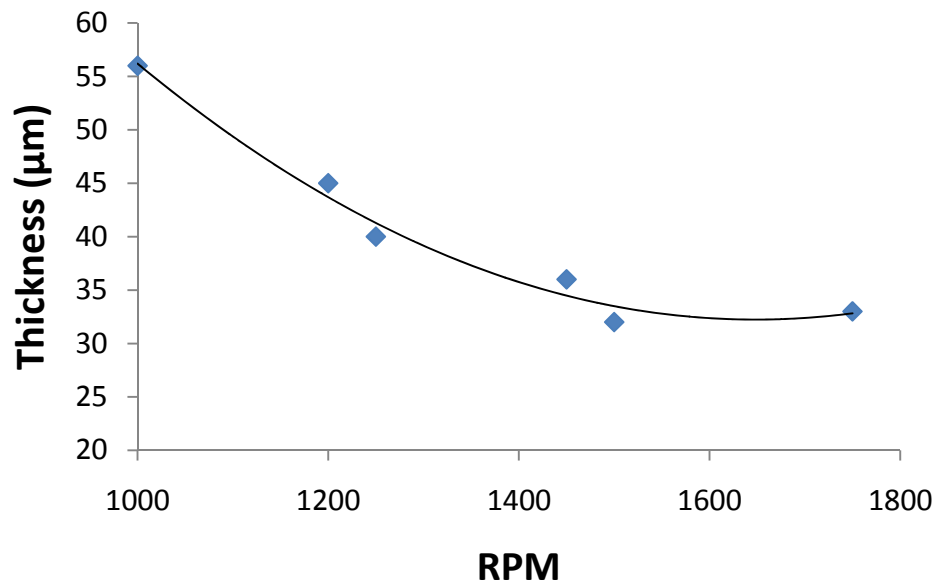


Figure 3.8: PDMS thickness vs. spin speed curve. Speeds higher than 1500 RPM display little change to the thickness.

A polynomial fit has been made to the data in the graph. RPM speeds higher than 1500 do not change the thickness while lower RPM speeds increase the thickness at a higher than linear rate. The AZ9260 mold height is only 32 microns on average, so speeds higher than 1400 RPM do not produce an adequate membrane thickness to use for the valves. It is suggested in literature that good valve sealing is achieved with membranes on the order of 20 – 30 microns [143]. The lowest spin speed in this graph of 1000 RPM produces membranes that are ~24 microns thick. These were found to work well during testing and lower speeds to achieve thicker valves were not attempted.

After the PDMS is spun over the wafer, it is cured in the box furnace with the same recipe previously mentioned of 80 °C for 17 minutes with a 5 minute ramp. The wafer is set aside after curing and the next PDMS process is started.

The valve channels are formed using PDMS cured over the mold wafer shown previously in Figure 3.5b. This PDMS is mixed using a ratio of 5:1 elastomer to curing agent. This high curing agent concentration produces more a more rigid layer of PDMS which also demonstrates high bonding affinity to PDMS with a lower concentration of curing agent i.e. the thin PDMS layer spun over the AZ9260 mold which has a 20:1 ratio). The 5:1 mixture of PDMS is poured over the valve channel mold and cured using the same heating process in the box furnace. Afterwards, individual pieces are cut from the PDMS and aligned over the spun PDMS on the AZ9260 mold to form a stack of two layers. This process is shown schematically in Figure 3.9 and a photo of the bonded layers is observed in Figure 3.10.

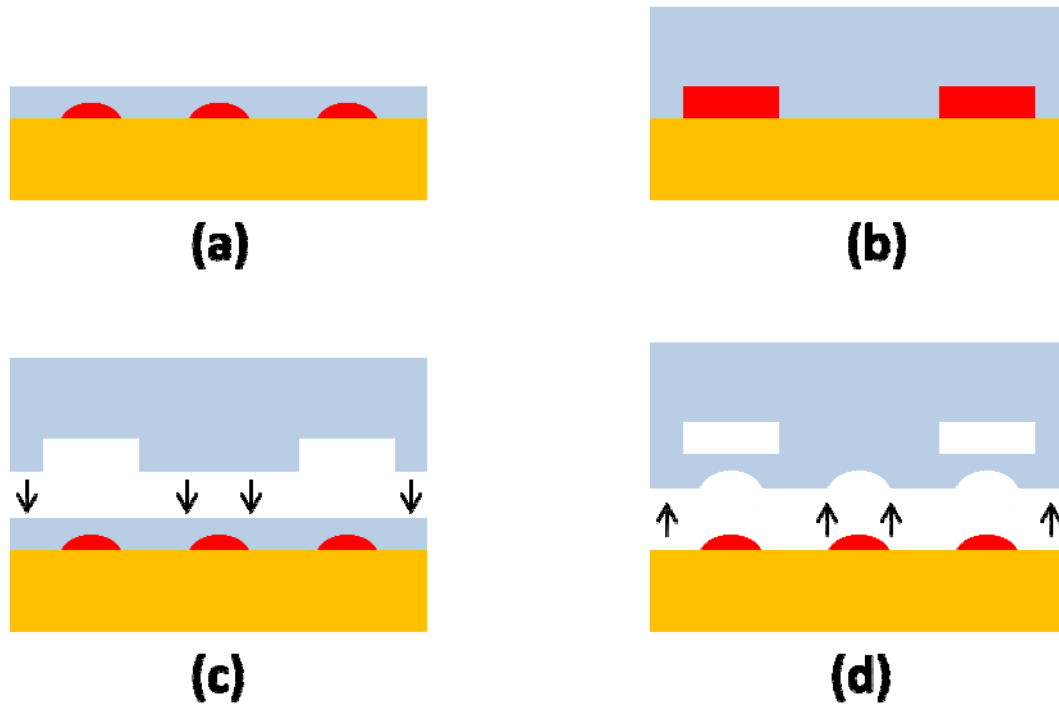


Figure 3.9: Dual layer PDMS fabrication process including a spun layer to form microfluidic channels (a) and a thicker layer to form valve channels (b). The thicker layer is cut into smaller portions and aligned over the spun PDMS as shown in (c). After curing together, the entire stack is cut out and peeled away from the mold as shown in (d).

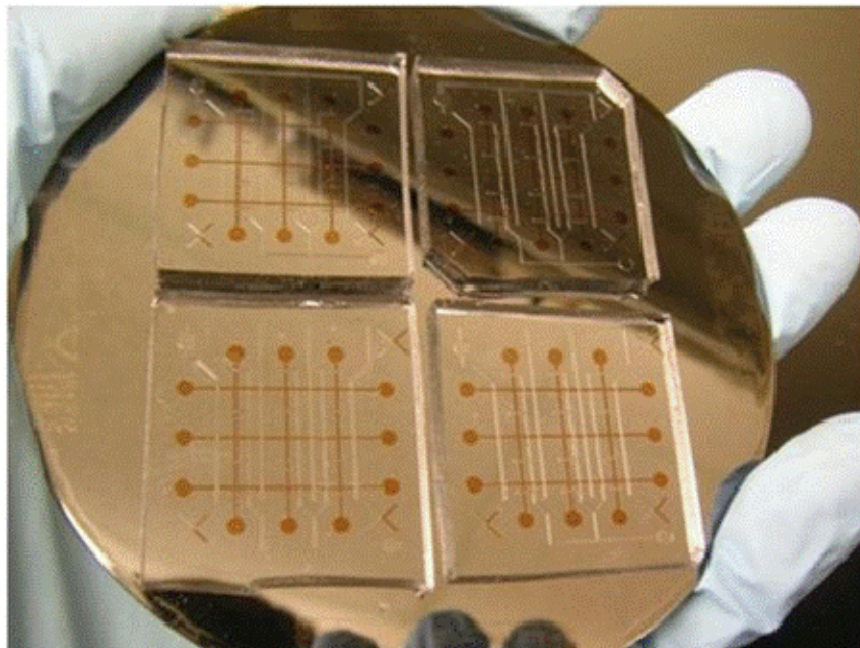


Figure 3.10: Photograph of the two layers of PDMS bonded to one another over the AZ9260 mold wafer. Individual pieces from the top valve layer are aligned over the fluidic channel network. The entire stack is bonded by placing it back into the box furnace.

Once the two PDMS layers have been bonded together, they must be cured together to complete the bond. The curing is performed in the box furnace at 80 °C for 3 hours. The furnace should also be allowed to cool back down to room temperature over another 3 hours. This procedure promotes a stronger bond between the two layers since they each contain a different ratio of curing agent.

3.4 Bonding and Packaging

PDMS is known to bond well with hydrophilic surfaces such as glass and silicon dioxide. A reversible bond can be created by simply pressing the PDMS over these substrates and will provide leak proof sealing providing the channels are large enough and the flow rate is low enough. This bond is used for the microfluidic chip design that does not contain valves. The PDMS channels can be peeled away and replaced onto the chip with adequate sealing so long as the liquid flow rate remains under 200 $\mu\text{l/hr}$. However, a reversible bond is not sufficient when applying air pressure to actuate the valves. A stronger, irreversible bond of the PDMS to the substrate is necessary in this case. The procedure for creating a covalent bond between the PDMS and substrate is explained here. Also explained are the connections for the fluid inlets and outlets.

3.4.1 Plasma Bonding Procedure

By exposing both the PDMS and the substrate surface to oxygen plasma, a strong intermolecular bond can be created between the two. The plasma forms functional silane groups (Si-OH) on the surface of both the PDMS and the glass or silicon dioxide substrate. When the surfaces are brought into conformal contact with one another, the silane groups on each surface condense with each other to form

strong intermolecular siloxane (Si-O-Si) bonds. The activated silane groups on the surface will relax over time and return to methyl groups so it is important to perform the bonding soon after the exposure to the oxygen plasma.

The exact procedure for performing the bonding is detailed here. The wafer containing the four double stacks of cured PDMS (shown earlier in Figure 3.10) is brought into a cleanroom environment along with the individual electrode array chips on either glass or silicon dioxide. One of the four PDMS stacks is cut out using a razor blade and peeled away from the mold. A dermatological punch with a radius of 1 mm is used to punch holes in the dual layer PDMS stack to create both fluid and pneumatic inlets. The electrode chip is cleaned using piranha solution to clean the surface of any organic contaminants. The PDMS stack along with the electrode chip are placed face up in a reactive ion etch (RIE) machine to expose each surface to the oxygen plasma. After exposure, a few drops of methanol are placed on the chip and the PDMS stack is aligned carefully over the electrodes. The methanol allows the user to slide the PDMS over the chip to provide better alignment. The methanol evaporates and the bond is allowed to set for 48 hours.

The parameters used for the RIE oxygen plasma exposure had to be tailored for the machine used in the Fablab. A March Jupiter III O₂ plasma system (Nordson March, OH) was used for this work. The machine allows the user to set the time of the exposure, the RF wattage and the pressure in the chamber. A range of RF wattages and pressures were tested to determine the bond strength of PDMS to silicon dioxide using this machine. The time was kept constant at 30 seconds. These parameters were chosen based on commonly used numbers for PDMS bonding found

in literature [145, 149, 152]. PDMS with 3 punched inlets was used for each bonding test and air pressure was applied to each of the inlets. The pressure at which the bond delaminated was recorded for each trial along with observations concerning what percentage of the PDMS bonded strongly with the substrate. This data is given below in Table 3.8.

Table 3.8: Bond strength of PDMS to silicon dioxide for various RIE machine parameters.

Power (W)	Pressure (mTorr)	Bond Strength (kPa)	Notes
20	200	20.7	~1% of PDMS area strongly bonded
20	400	96.53	~70% of PDMS area strongly bonded
20	600	6.9	0% of PDMS area strongly bonded
20	800	6.9	0% of PDMS area strongly bonded
50	200	110.3*	~15% of PDMS area strongly bonded
50	400	68.9	~20% of PDMS area strongly bonded
50	600	6.9	0% of PDMS area strongly bonded
50	800	6.9	0% of PDMS area strongly bonded

* Only for 1 inlet. Other two inlets delaminated at < 10 kPa applied pressure

From the table, it is clear that lower pressures work much better than higher pressures. Both cases with 800 mTorr demonstrated no bonding at all between the PDMS and the silicon dioxide. Also, using higher RF power did not significantly increase the bond strength. Based on these results, a recipe of 20 W with a chamber

pressure of 400 mTorr was chosen. The pressure utilized for actuating the valves is around 35 kPa so a bond strength of 96.53 kPa is well above this value. Furthermore, this recipe produced the highest area percentage of PDMS strongly adhered to the surface. Bringing this number closer to 100% was achieved by allowing the bond to form over a longer period of time (72 hours as opposed to 48 hours). PDMS bonds much more strongly to glass than to silicon dioxide and it was found that 20 W at 400 mTorr produced a leak-proof bond between PDMS and glass without the need for further characterization.

The fabrication of the valved microfluidic device is complete following the plasma bond of the PDMS. Figure 3.11 demonstrates the completed device on a glass substrate for better clarity of the various channels. The microfluidic channel network is filled with green dye while the two valve channels are filled with red and blue dye.

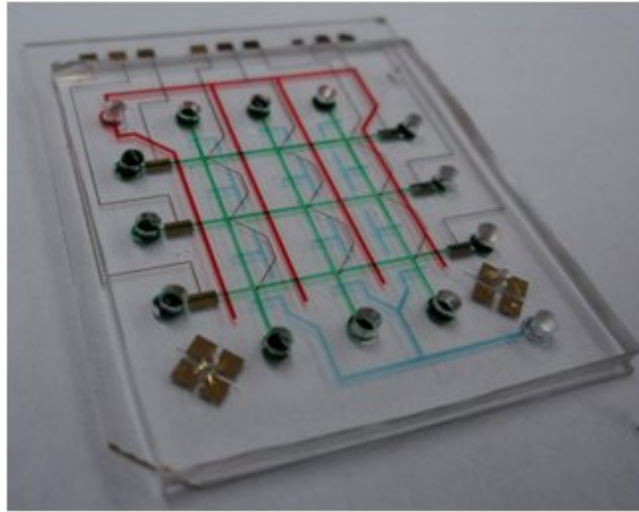


Figure 3.11: Photograph of completed valved microfluidic device containing microfluidic network (green) and valve channel networks (red, blue).

3.4.2 Fluidic connections

Tubing is attached to each of the hole-punched inlets in the device via plastic elbow connectors or straight connectors (Cole-Parmer, IL). The connectors are sized

to fit 1/16" tubing. Tygon flexible tubing is used to deliver either liquid samples or pressurized air to the inlets. Figure 3.12 shows the tubing-connector assembly.

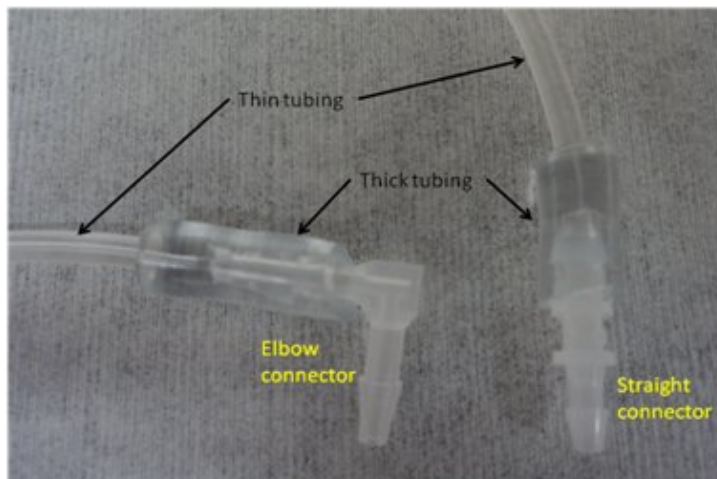


Figure 3.12: Plastic connectors used to interface tubing with the microfluidic device. Two sizes of tubing are used to create a leak-proof seal.

Two sizes of tubing are used to make a leak-proof seal with the connector. Small pieces of thick tubing with OD .1875" and ID .0625" fit snugly around the plastic connector and around thinner lengths of tubing with OD .087" and ID .015". The thinner tubing is used to create a tight fit to the end of a syringe needle which supplies the liquid to the device. The elbow connectors were found to work best with the microfluidic device without valves while the straight connectors were ideal for use with the device containing the valves.

3.5 Summary

This chapter has covered the fabrication procedure for each of the 4 device designs. Metal patterning was performed using both wet chemical etching and lift-off techniques. The second design included an extra patterning of SU-8 5 to create a hydrophobic region on the chip. Molds for forming the PDMS channels were created on silicon wafers with either patterned SU-8 50 for large (100 μm height) channels

and AZ9260 for small (25 μm height) channels. Both the spin speed and bonding parameters were characterized for the PDMS to produce membranes of ~ 30 μm thickness and a bond strong enough to silicon dioxide and glass to withstand the pressures applied during testing. Final packaging of the device was achieved by using plastic elbow and straight connectors coupled with plastic tubing to form a snug fit around both the connectors and a syringe needle.

4 Testing and Characterization

4.1 Introduction

This chapter focuses on the testing set-up utilized for each of the device designs as well as observations concerning the electrochemical characteristics of each sensor. The first section covers preliminary electrochemical tests performed on the macroscale electrode chips as well as the droplet sensing chips. The latter sections cover the testing procedure for the microfluidic device designs and characterization of the 3 x 3 sensor network. The changes to the diffusion regime in the device after integration of the valve network is explored by comparing collected data from the sensors both before and after the integration of the valves.

4.2 Preliminary Electrochemical Tests

Before the construction of the microfluidic device, electrochemical tests were performed using both a beaker of electroactive solution and with the chip designed for testing the micropatterned electrodes using a droplet of electroactive solution. These tests were performed to become familiar with the electrochemical techniques and to test the potential stability of platinum as a reference electrode.

4.2.1 Beaker Experiments

All of the experiments performed with a beaker used 6 mL of electrolyte with the added redox compound in a 10 mL beaker. Alligator clips were used to make contact to the gold macroscale chips consisting of counter and working electrodes. The areas for each electrode were 48.75 mm² and 3.14 mm² respectively. An in-house device was designed to hold the alligator clips in place suspended above the beaker.

A commercially purchased Ag/AgCl reference electrode containing 1 M KCl (CH Instruments, TX), was also suspended along with the chips using the designed holder. A photograph of the testing set up is shown in Figure 4.1.

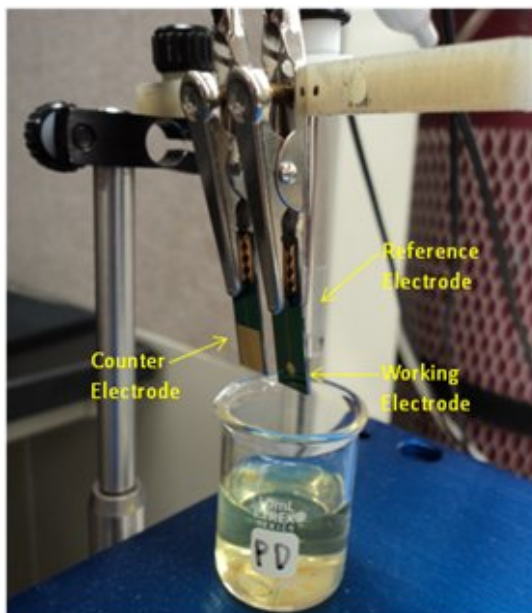


Figure 4.1: Photograph of testing set-up used for all beaker experiments.

The working electrode chip is designed to fit within a 2 mL centrifuge tube so that it can be easily incubated with solutions containing the biomolecules of choice. The blue platform can be raised or lowered to bring the electrodes down into the solution for testing. DNA hybridization experiments using this set up are shown in Chapter 6.

4.2.2 Droplet Testing

The micropatterned chips used with a droplet of solution were made to characterize the stability of the platinum reference electrode and also to perform some basic biomolecule assembly experiments before the fabrication of the microfluidic devices. Probe needles make electrical contact to pads patterned around the edge of the chip. A photograph of one of the droplet chips under test is shown in Figure 4.2.

Cyclic voltammetry experiments were performed using two different sizes of working electrodes and on different days. The data is displayed in Figure 4.3.

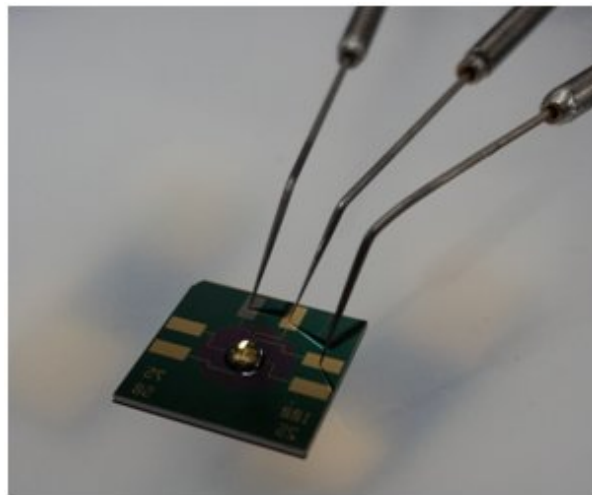


Figure 4.2: Photograph of droplet chip under test. A droplet of electroactive solution is placed over the electrodes in the center of the chip.

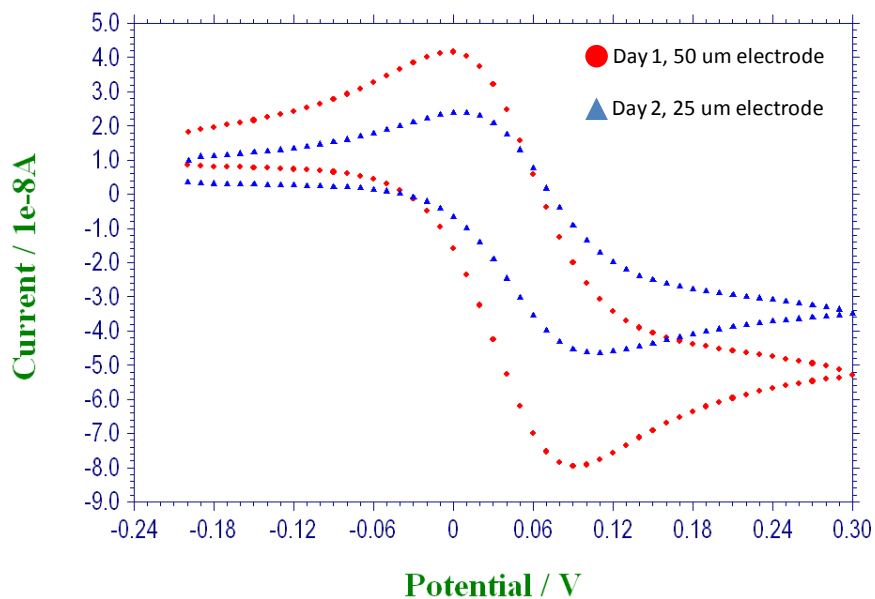


Figure 4.3: CV scans using the droplet chip of two electrodes on different days. The redox peaks occur at nearly the same value which demonstrates the stable nature of platinum as a reference electrode.

Using platinum as a reference instead of Ag/AgCl shifts the potential at which the peaks occur more negative. The important observation from this data is that the redox peak potentials do not change for different days of testing and with different

working electrodes. This data demonstrates the stability of the platinum reference electrode and justifies its inclusion for the microfluidic devices.

Several CV scans separated by 10 minute intervals were performed for the same electrode and the same droplet of solution to determine short term stability of the measurements. The results are shown in Figure 4.4.

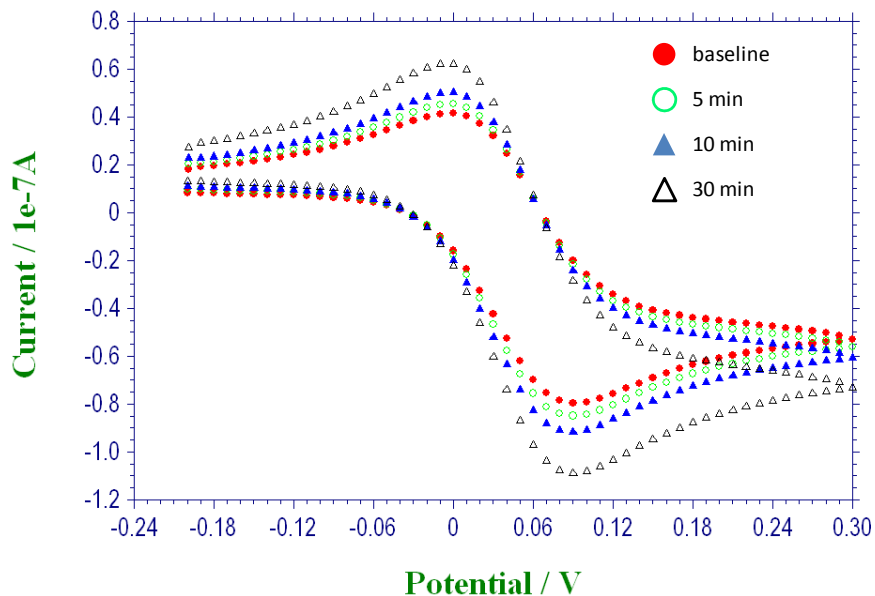


Figure 4.4: Repeated scans of same electrode using droplet sensor. Increasing current attributed to constant evaporation of the droplet.

The data demonstrates little change in the potentials of the redox peaks as expected, however, the peak amplitude increases over time. It was discovered that this effect is due to the slow evaporation of the electroactive droplet. As the liquid evaporates, the concentration of the dissolved redox compound increases which increases the measured current.

4.3 Microfluidic Device Testing

The microfluidic device design incorporating straight parallel channels in a single layer of PDMS contains 9 working electrodes in a 3 x 3 array. This section

covers the testing set-up and procedure for using the device as well as electrochemical characterization data for the patterned sensors.

4.3.1 Testing and Operation

The device contains 6 total fluid inlets/outlets and electrical contact pads along one side of the chip for easy probe access. A photograph of the completed device under test is shown in Figure 4.5. The device in the picture is patterned on a silicon dioxide substrate and uses elbow plastic connectors for each fluid inlet/outlet. The probes can be easily manipulated to make electrical contact to any of the electrodes patterned within the microfluidic channels. The layer of PDMS is molded to be on the order of 2-3 mm thick in order to provide better stability with the inserted plastic connectors.

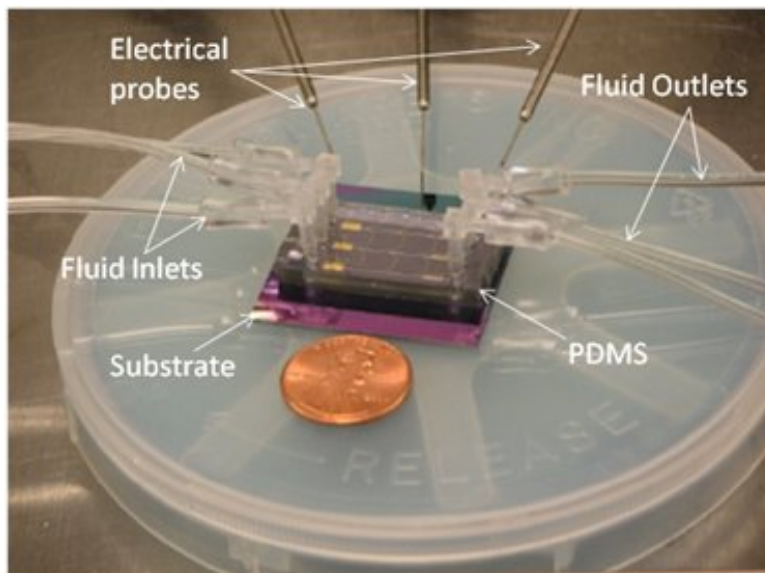


Figure 4.5: Photograph of the microfluidic device design without valves under test.

The spacing of the sensors and the molded channels are designed so that the channels can be placed across the sensors exposing each sensor column in its own unique channel. Each sensor column can be incubated with a different

functionalization compound without any cross-contamination between the other channels. Afterwards, the PDMS channels can be peeled off, rinsed, then rotated 90 degrees in-plane and placed back down over the patterned sensors. In this way, rows of sensors are exposed in each channel along with unique counter and reference electrodes. This process was discussed previously and demonstrated schematically in Chapter 2.

The manual rotation of the channels is necessary due to the lack of valves to control the fluid flow. The surface functionalization consists of different passivation compounds for the protein adhesion study and ssDNA probe sequences for the DNA hybridization study. DNA or protein samples are incubated in the horizontal channels over each of the sensor surfaces. Each channel can be filled sequentially with electroactive solution before and after the sample incubation for each of the sensors to determine any adsorption or affinity based binding activity.

4.3.2 Sensor Uniformity

Each of the 9 sensors within the device was tested to determine their overall uniformity as well as the potential stability of the platinum reference electrode for each channel row. Each channel was filled with electrolyte containing the ferri/ferrocyanide redox couple and CV scans were taken of the bare electrode surface. Results of these scans are shown in Figure 4.6. Each sensor exhibits very similar peak separation (0.087 ± 0.004 V) and peak amplitudes for both the oxidation (-799 ± 9.8 nA) and reduction (746 ± 9.8 nA) peaks. The oxidation and reduction potentials of the ferri/ferrocyanide couple are 0.037 ± 0.002 V and -0.05 ± 0.002 V respectively for each of the nine sensors which demonstrates the relative potential

stability of the platinum reference electrodes in each channel. The three sensors in the bottom microfluidic channel have less exposed gold due to the design of the leads and thus slightly lower peak amplitudes compared to the other six.

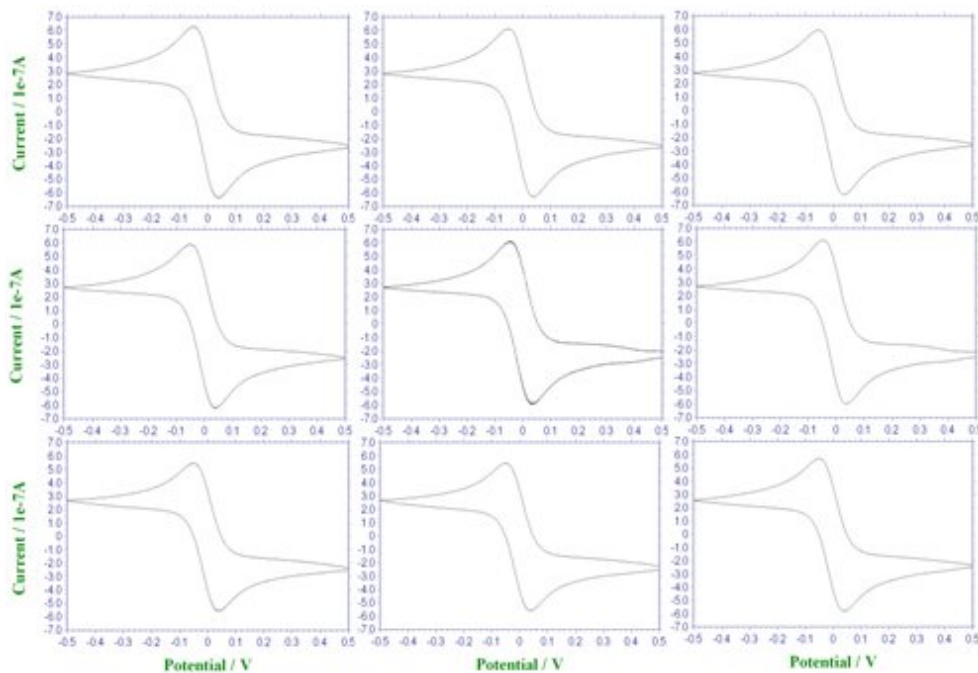


Figure 4.6: Cyclic voltammetry plots from the nine sensors in the microfluidic device arranged in a 3 x 3 grid. The peak heights and peak separation are all very similar for each plot demonstrating excellent reproducibility among the patterned sensors.

4.3.3 Sensor Cleanliness

The cleanliness of the electrode surface can be observed electrochemically from how reversible the oxidation and reduction reactions of the ferri/ferrocyanide couple are. The peak current from a CV scan should follow the Randles-Sevcik equation (2.5) described earlier. According to the equation, the peak current should be linearly proportional to the square root of the scan rate if the reaction is reversible. Figure 4.7 displays the CV response for one of the sensors at scan rates varying from 25 - 800 mV/s. The inset graph displays the linear relationship between the peak current and the square root of the scan rate with an R^2 value near unity. The observed slope is $1.2 \mu\text{A}/\nu^{1/2}$ where ν is the scan rate in (V/s). This value is very close to the

expected value of $0.81 \mu\text{A}/\nu^{1/2}$, which has been calculated using the diffusion coefficient for ferri/ferrocyanide found in literature [153]. The higher observed slope may be due to the roughness of the electrode contributing a higher surface area. It is also important to observe from the cyclic voltammograms that the oxidation and reduction peak potentials at each scan rate are the same which is further evidence of a reversible reaction and a clean electrode surface.

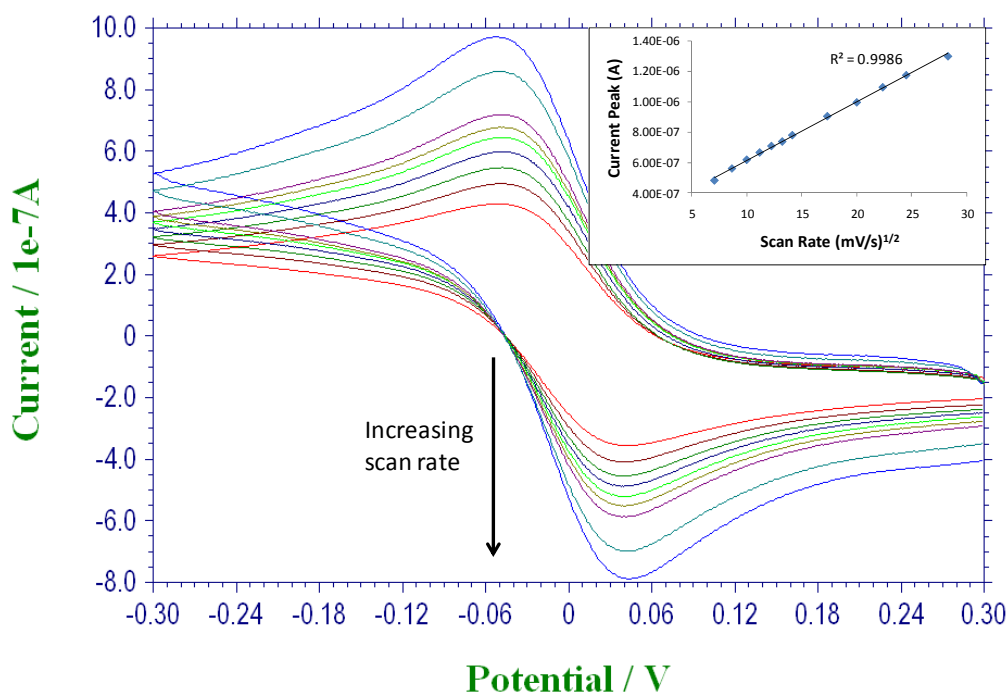


Figure 4.7: Cyclic voltammograms with increasing scan rates from 25 – 800 mV/sec. (inset) Linear relationship observed between the reduction current peak amplitude and the square root of the scan rate.

4.4 Valved Microfluidic Device

The microfluidic device integrated with the PDMS valve layer requires a more careful operating procedure. Puncturing any of the valve membranes either from too much applied air pressure or liquid flow can ruin the entire device. This section details the testing set up and operating procedure for the valved device as well as some electrochemical tests.

4.4.1 Testing and Operation

The valved device contains 12 fluid inlets/outlets and 2 pneumatic inlets. Electrical contact pads are patterned along one side of the chip for probe contact similar to the device without valves. The entire testing set-up is shown in Figure 4.8. A single channel syringe pump (Kent Scientific, CT) is used to deliver fluid samples to the device while a micro centrifuge tube collects the fluid waste. A regulator outputs 5 psi of pressurized air and is controlled via the valve shown in the picture.

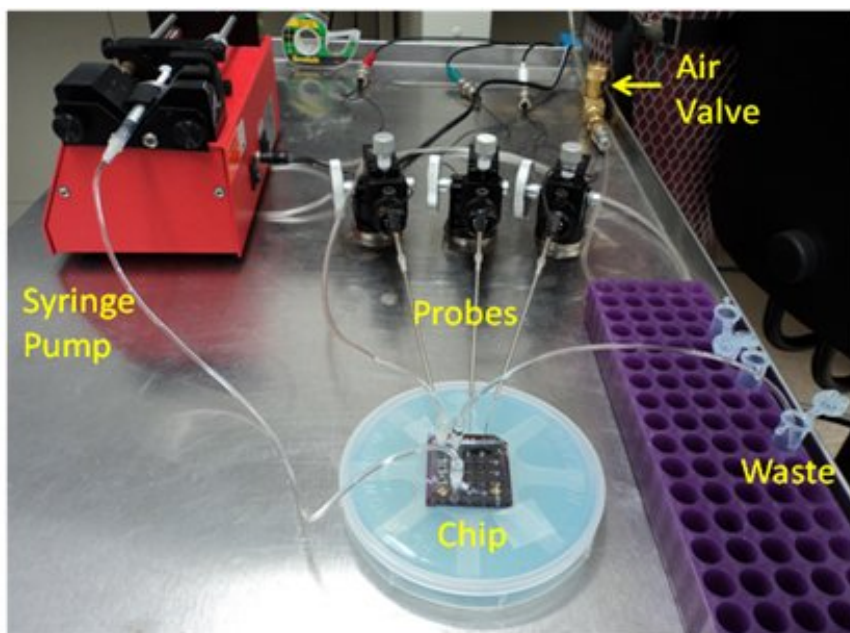


Figure 4.8: Photograph of testing set-up utilized for the valved microfluidic device.

The pressurized air is either applied to the top left or bottom right inlet to form vertical or horizontal microfluidic channels passing over the sensor array. Vertical channels are used for sensor surface functionalization while the horizontal channels are used for electrochemical testing and sample incubation similar to the device without the valves. Figure 4.9 below uses a device with a glass substrate to demonstrate the separation achieved between the vertical and horizontal channels when pressure is applied to the two inlets.

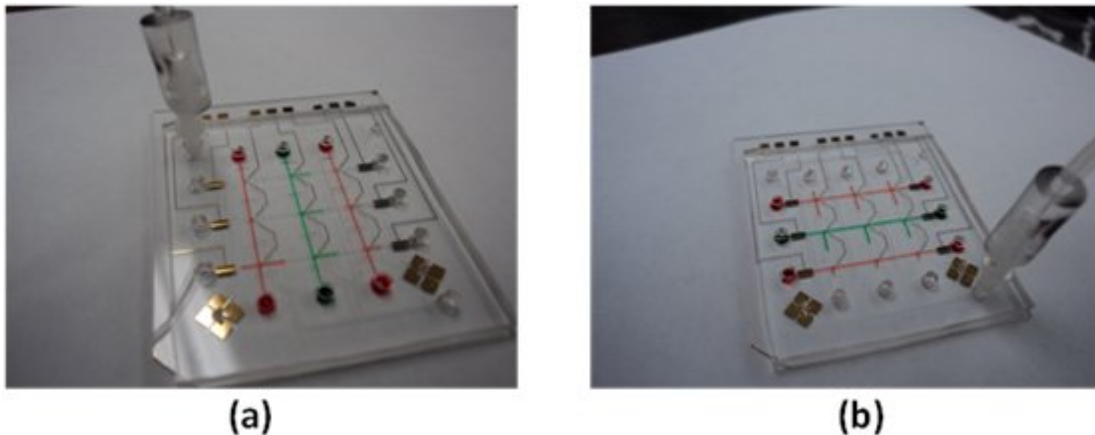


Figure 4.9: (a) vertical channels created in device by applying pressure to top inlet and (b) horizontal channels created by applying pressure to the bottom right inlet.

It can be noticed in the pictures that the liquid also travels a short distance down the perpendicular channel in a few instances. However, the flow is always stopped at the point where the valve crosses the microfluidic channel. The filling of certain perpendicular channels while not filling others is related primarily to minor changes in the hydrophobicity of the surface as well as any trapped air that may be in the channels at the time of the fluid flow. The more important observation is that the liquid from each channel does not cross into the other parallel channels demonstrating the effectiveness of the valves.

4.4.2 Pneumatic vs. Hydraulic Actuation

During the testing of the valved microfluidic device, a problem with the use of pressurized air to actuate the valves became apparent. PDMS is permeable to air, in fact, this property is one of the reasons why it is so widely chosen for in-vitro biological studies [154, 155]. However, the use of pressurized air to depress the thin PDMS membranes causes the air to also leak through the membrane and into the channel. This causes noticeable bubble formation in the channels within minutes of applying the pressure. These bubbles not only disrupt the ability for biomolecules to

self assemble on the surface, they also interrupt the fluid connection between the electrodes during the electrochemical measurement.

The solution to this problem was to fill the valve channels slowly with liquid and apply pressurized air on the back end. In this configuration, the incompressible nature of the fluid is used to press downward on the valve membranes with applied pressure. The channels must be filled very slowly otherwise the membranes will break under the pressure. The syringe pump was used to fill the valve channels with water at a flow rate of 30 $\mu\text{l/hr}$. Rates faster than this value caused the membranes to break during the filling procedure. Each channel takes almost 30 minutes to fill using this procedure. Afterwards, pressurized air at 5 psi was applied to the inlet to push on the back of the water allowing it to completely fill the channel.

4.4.3 Sensor Uniformity

A similar sensor uniformity experiment was performed using the valved microfluidic device as that performed with the non-valved device. CV scans were taken from each of the nine clean sensor surfaces using the valves to control the fluid flow in only the horizontal direction. The results are displayed in Figure 4.10 in the same 3 x 3 grid as the physical sensor layout. The CV results from the nine sensors in the valved device do not display the same level of electrochemical uniformity as the non-valved device. The output of the sensors from the same row shows the highest similarity to one another.

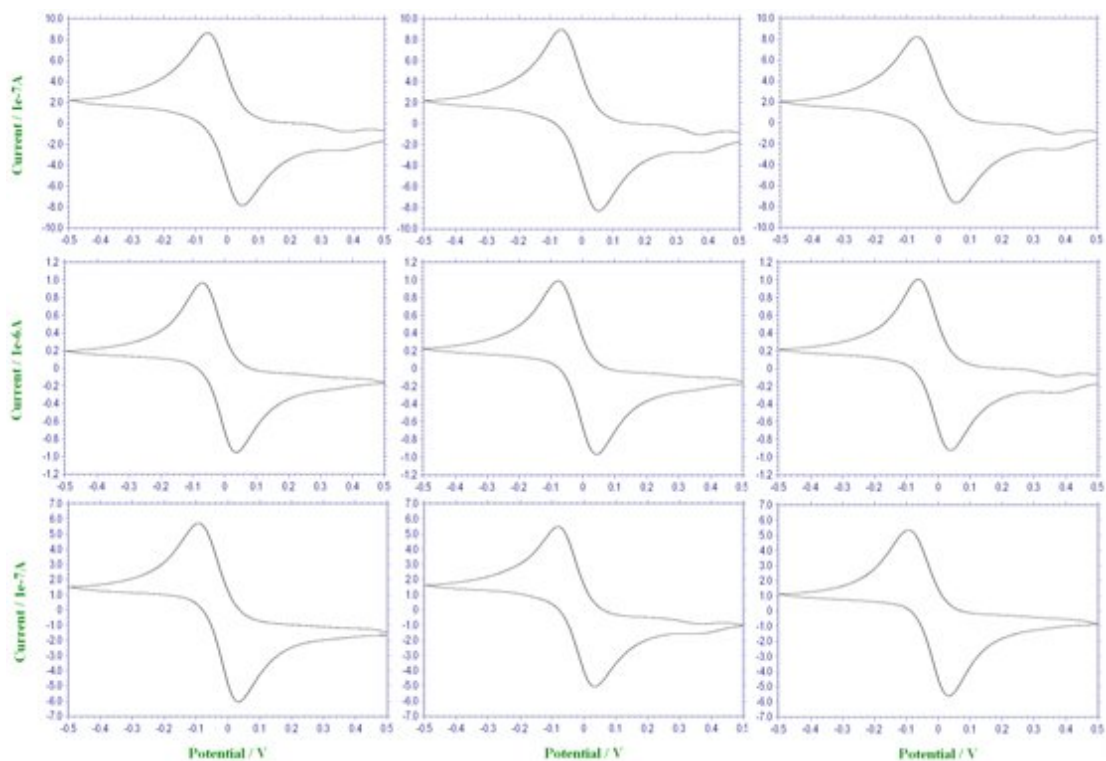


Figure 4.10: CV scans for each of the nine clean working electrodes in the valved microfluidic device. The graphs are displayed in the same 3 x 3 grid as the physical sensor layout.

By examining the rows separately, the top row contained oxidation and reduction peak amplitudes of -768 ± 40 nA and 820 ± 36 nA respectively, the middle row contained oxidation and reduction peak amplitudes of -987 ± 28 nA and 970 ± 13 nA respectively, and the bottom row contained oxidation and reduction peak amplitudes of -594 ± 69 nA and 571 ± 42 nA respectively. The peak separation for all sensors was 116 ± 9 mV so good reference stability was still observed in the valved device. The variation in the peak amplitudes between the three different channels is primarily explained by the way the liquid fills each of the channels. Due to the valve design, trapped air in the system can affect what portions of the channels the liquid fills and this can lead to slight variability between the impedances measured between the electrodes in each of the channels. This is not a significant problem since most

sensing experiments are only concerned with the change in the signal of one sensor and not versus other sensors, but it is still worthy of note.

4.4.4 Sensor cleanliness

A test on the cleanliness (and reaction reversibility) of the electrode was also performed for the valved microfluidic device. CV scans were performed with scan rates varying from 25 – 300 mV with the results displayed below in Figure 4.11.

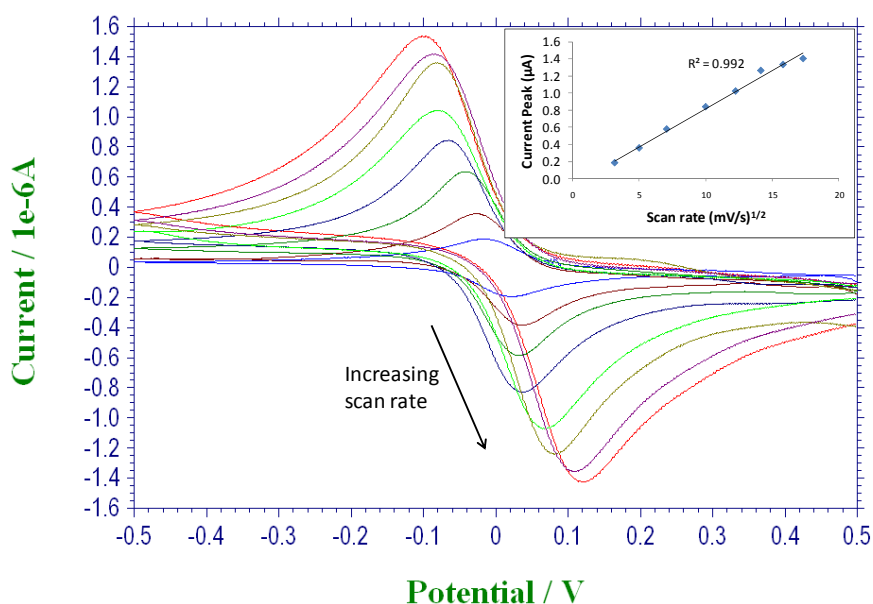


Figure 4.11: CV scans of an electrode in the valved microfluidic system at increasing scan rates. The inset graph displays the linear correlation between the peak amplitude and the square root of the scan rate.

The increasing scan rate increases the peak heights as expected, and a high linear correlation is observed between the peak amplitude and the square root of the scan rate as described by the Randles-Sevcik equation (2.5) for a reversible reaction. The observed slope is 2.9 $\mu\text{A}/\nu$ compared to an expected slope value of 1.4 $\mu\text{A}/\nu$. It is also observed that the redox peak potentials separate further and further apart as the scan rate increases. This can possibly be explained due to the confined geometry of the microfluidic channel. As the scan rate increases, the diffusion gradient above the

electrode surface cannot be maintained due to insufficient redox compound in the vicinity, leading to variation with the half cell potential and increased separation in the peak potentials. Another example of this point can be observed at scan rates over 300 mV/s (not shown in figure) in which the linearity expressed in the Randles-Sevcik equation no longer holds true due to the quick depletion of the redox compound.

4.4.5 Diffusion Limitation of Valve Integration

In order to integrate valves with the electrode array, the channel geometry has to be altered. Without valves, the microfluidic channels have a cross sectional area of $50,000 \mu\text{m}^2$, while the valved version contains channels with a cross sectional area of $6458 \mu\text{m}^2$. This large reduction in the solution volume above the electrode has a noticeable effect on the diffusion properties of each design. The CV plots demonstrate this with the broadening of the peak potentials in the case of the valved device.

Further exploration into this limited diffusion regime requires a comparison of the total charge that the sensor collects for both the non-valved and valved design. The charge can be determined by integrating the current that is collected during the CV scans vs. time. The CV scan taken at a scan rate of 100 mV/sec was compared for both device designs. The current was integrated in a single potential sweep direction until the peak is reached. A comparison of the total charge collected for each design is shown in Figure 4.12. The curves demonstrate that the valved device takes longer to reach its peak charge due to a slower-forming diffusion gradient.

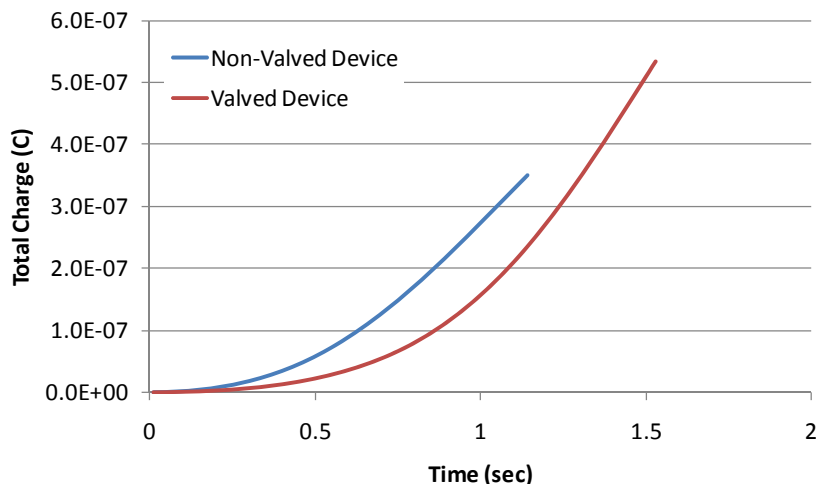


Figure 4.12: Total charge passed through sensor for both the non-valved and valved design. The valved device takes longer to form the diffusion gradient.

With the charge calculated, the ratio of the total number of ferrocyanide molecules that are reduced during the scan can be compared to the total number of molecules that are available over the sensor in the channel. This interaction ratio should be less than 1 for a situation in which the diffusion layer can form without any hindrance and is displayed below in equation 4.1.

$$\frac{n_o}{n} \leq 1 \quad (4.1)$$

Where n_o is the number of molecules oxidized/reduced during the scan and n is the total number of molecules available. If the ratio is greater than 1, then the diffusion in the system cannot maintain the concentration of species required to interact with the electrode. Since it is known that each ferrocyanide molecule exchanges a single electron with the electrode during both oxidation or reduction, the total charge can be divided by the charge of an electron (1.6×10^{-19}) to provide the value of n_o for both the non-valved and valved devices. By performing this calculation, n_o for the non-valved device is 2.19×10^{12} and n_o for the valved device is 3.34×10^{12} .

Calculating the value of n for each case requires first understanding what the extent of the diffusion layer is. The diffusion layer describes the distance a molecule can diffuse in a certain amount of time. It is calculated from solving Fick's 1st and 2nd laws of diffusion for a linear trajectory and the result is shown below in equation 4.2.

$$\delta = 2\sqrt{Dt} \quad (4.2)$$

Where D is the diffusivity of the molecule that is diffusing and t is the time. From Figure 4.12, the time over which the charge is collected can be observed for each device design and a diffusivity of 0.7×10^{-5} is used for ferrocyanide as calculated in literature [153] to determine the diffusion layer to be $56.75 \mu\text{m}$ and $65 \mu\text{m}$ for the non-valved and valved devices respectively. The volume of solution that interacts with each electrode is calculated using the diffusion layer distance to be 2.03 nL and 1.33 nL for the non-valved and valved devices respectively. From the volume, the number of total molecules present (n) can be calculated and these are determined to be 3.06×10^{12} and 2.00×10^{12} for the non-valved and valved devices respectively. Ultimately, the interaction ratios can be calculated to be 0.72 and 1.67 for the non-valved and valved devices respectively.

An interaction ratio greater than 1 is observed after the integration of the valves providing evidence of a diffusion limited system which affects the formation of the diffusion gradient and will have an effect on the formation of any monolayers. This observation of the diffusion limitations in the valved device will ultimately cause a change in the detection mechanism when performing DNA hybridization experiments and is discussed in more detail in Chapter 6.

4.5 Summary

This chapter has discussed the testing procedure and sensor characterization for all 4 device designs. Initial testing with the macroscale chips determined that the ferri/ferrocyanide couple was a better choice of redox compound vs. ferrocene due to its higher charge transfer. Droplet tests were also performed, but were discontinued due to uncontrollable changes in the electrochemical response caused by evaporation. The micro-patterned sensors of the device before and after valve integration showed excellent electrochemical uniformity and redox reversibility. The diffusion limited regime created after valve integration was explored in detail and compared to the non-valved design.

5 Protein Adsorption Study

5.1 Introduction

One major challenge in designing a selective biosensor is the reduction of non-specific adsorption onto the sensor surface. Various passivation compounds are used for this purpose, but it can be difficult to know how effective the material is at resisting adsorption to a wide range of possible proteins. There has also been extensive research aimed at observing biomolecule adsorption to passivation compounds immobilized onto drug delivery systems and various other biomedical devices [111, 156, 157]. The adsorption kinetics of proteins to a vast array of surfaces and immobilized compounds has been debated and analyzed by many groups [158-160]. All purification steps of the cAMP receptor protein (CRP) were performed with the help of Varnika Roy from Dr. Bentley's group at the University of Maryland.

This chapter discusses all of the data collected regarding protein adsorption to various surface compounds using the microfluidic device. To our knowledge, this is the first demonstration of electrochemical measurements in a microfluidic device for this purpose. The first section covers each of the proteins and surfaces used in the study while the proceeding sections will discuss the adhesion data and model fitting.

5.2 Materials Used

The device's sensor surfaces are modified using three well-known passivation agents: mercaptohexanol (MCH), a thiolated polyethylene glycol (PEG), and bovine serum albumin (BSA). MCH is very commonly used to passivate sensing surfaces for both protein and DNA sensing while PEG has been widely studied for its ability to

resist protein adsorption [109, 116, 117, 161]. BSA has been extensively used to passivate surfaces against non-specific binding in a variety of biosensors [162, 163].

Three different proteins have been chosen to interact with the modified sensor surfaces: cAMP (cyclic adenosine monophosphate) receptor protein (CRP), tumor necrosis factor α (TNF α), and tumor necrosis factor β (TNF β). CRP is a common gene regulator in bacteria and is the focus of many genetic and biochemical studies [164, 165]. Both TNF α and TNF β are used extensively in cancer related research as tumor markers [34, 35]. The proteins are chosen to represent various biological applications to highlight the broader impact of this research, and provide a proof-of-concept operation of the device.

Tumor necrosis factor α , tumor necrosis factor β , 6-mercapto-1-hexanol and bovine serum albumin were each purchased from Sigma-Aldrich (St. Louis, MO) and (1-mercapto-11-undecyl)tetra(ethylene glycol) was purchased from Asemblon Inc. (Redmond, WA). Both the MCH and PEG were diluted in 10 mM PBS. TNF α and TNF β were each reconstituted in 10 mM PBS with 0.1% BSA.

The bacterial CRP could not be purchased and had to be purified ourselves. A plasmid gene sequence for bacterial synthesis of CRP was given to us by Christopher Byrd at the Army Research Lab. The procedure for the creation of the CRP is as follows:

- 1) 1 liter of *E. coli* BL21DE3 cells containing a CRP IPTG (Isopropyl β -D-1-thiogalactopyranoside) inducible plasmid are allowed to express for 6 hours. Those cells which do not take in the plasmid are killed using the antibiotic, ampicillin (the plasmid also codes for ampicillin resistance).

- 2) The cells are lysed using an ultrasonic tip for 10 minutes, then placed in a falcon tube and spun at 12000 RPM for 10 minutes at 4 °C.
- 3) The supernatant is collected and the pellet is re-suspended, ultrasonicated again and spun down.
- 4) The two supernatant solutions are mixed and spun down 3-4 more times.
- 5) The supernatant is filtered through a 0.22 µm Millipore filter to remove any remaining cell debris.
- 6) The CRP is extracted from the solution using his-tag based IMAC purification (Immobilized Metal Affinity Chromatography) (GE healthcare hi-Trap column).
- 7) The sample is carefully pipetted into a dialysis membrane and placed in a chilled liter of 10 mM PBS solution for 24 hours at 4 °C to dialyze out the imidazole.
- 8) The sample is removed from the dialysis bag and the protein concentration is estimated using (OD280nm) and frozen at -80 °C in 50 µL aliquots.

The successful purification of the CRP was tested using a gel shift assay and a DNA sequence specific to the binding of CRP when in the presence of the ligand cyclic adenosine monophosphate (cAMP). The test was performed by Chris Byrd at the Army Research Lab in Adelphi, MD and the results are shown in Figure 5.1. In the figure, lanes 1-6 act as controls which contain either DNA only, CRP only, or DNA+CRP without the cAMP. Lanes 7 and 8 contain all three and display a clear binding reaction vs. the controls. This shift confirms the activity of the CRP and its successful purification.



Figure 5.1: Gel shift assay confirming CRP activity. Only lanes 7 and 8 display shifting due to the binding of the CRP to the DNA sequence in the presence of cAMP.

5.3 Surface Preparation

Solutions of 1 mM MCH, 1% BSA and 10 μ M PEG are dissolved in PBS to be used for testing. The PDMS channels are placed on the chip so that the nine working electrodes are exposed within the three channels. Using separate 1 mL syringes operating at 200 μ l/hr, channel 1 is filled with the solution containing the MCH while channel 2 is filled with the solution containing BSA and channel 3 is filled with the solution containing PEG. The solutions are incubated over the working electrodes for 1 hour to allow for the compounds to either bind to the gold surface via their thiol group (in the case of MCH and PEG) or adsorb to the surface (in the case of the BSA). Previous empirical studies were used to find that 1 hour is a sufficient amount of time for the assembly of each of the compounds to the electrode surface.

Afterwards, the PDMS channels are peeled from the chip and both are gently rinsed with PBS followed by de-ionized water, then blown dry with nitrogen. The channels are rotated 90 degrees and placed back over the chip so that each channel now contains a counter electrode, a platinum reference electrode and 3 working

electrodes, each with a different surface functionalization. Refer to Figure 4.6 for a visualization of the channel rotation procedure. PBS solutions containing either 50 $\mu\text{g/ml}$ CRP, 5 $\mu\text{g/ml}$ TNF α , or 5 $\mu\text{g/ml}$ TNF β are introduced across the sensors and allowed to interact with the surfaces for 15 minutes. Afterwards, the channels are flushed with PBS solution to remove any loosely adsorbed molecules. Impedance spectroscopy data is taken using the same PBS solution containing the ferri/ferrocyanide couple at a DC bias potential of -5 mV with an amplitude of 5 mV in the range of 10000 – 0.1 Hz. Scans are taken before and after the proteins are introduced to the channels.

5.4 Protein Adsorption Data

5.4.1 Adsorption to MCH

The change in impedance caused by each protein to the MCH surface is seen from the Nyquist plots in Figure 5.2. Figure 5.2a displays a clear impedance increase after incubation with TNF α . Figure 5.2b displays no measureable impedance change after incubation with TNF β and Figure 5.2c shows a clear decrease in impedance after incubation with CRP. Noise can be observed in some of the data at lower frequencies and is most likely caused by the long probe leads used to make contact to the chip as well as the small size of the electrodes used. These noise variations can be reduced through the use of a Faraday cage (a metal mesh) placed around the testing set-up. The noise is not significant enough to obscure the characteristic semi-circular shape and linear diffusion region and does not impede the ability for the data to be fit to the Randles circuit model from Figure 2.7. For these reasons, it was not made a priority to reduce the noise further during testing.

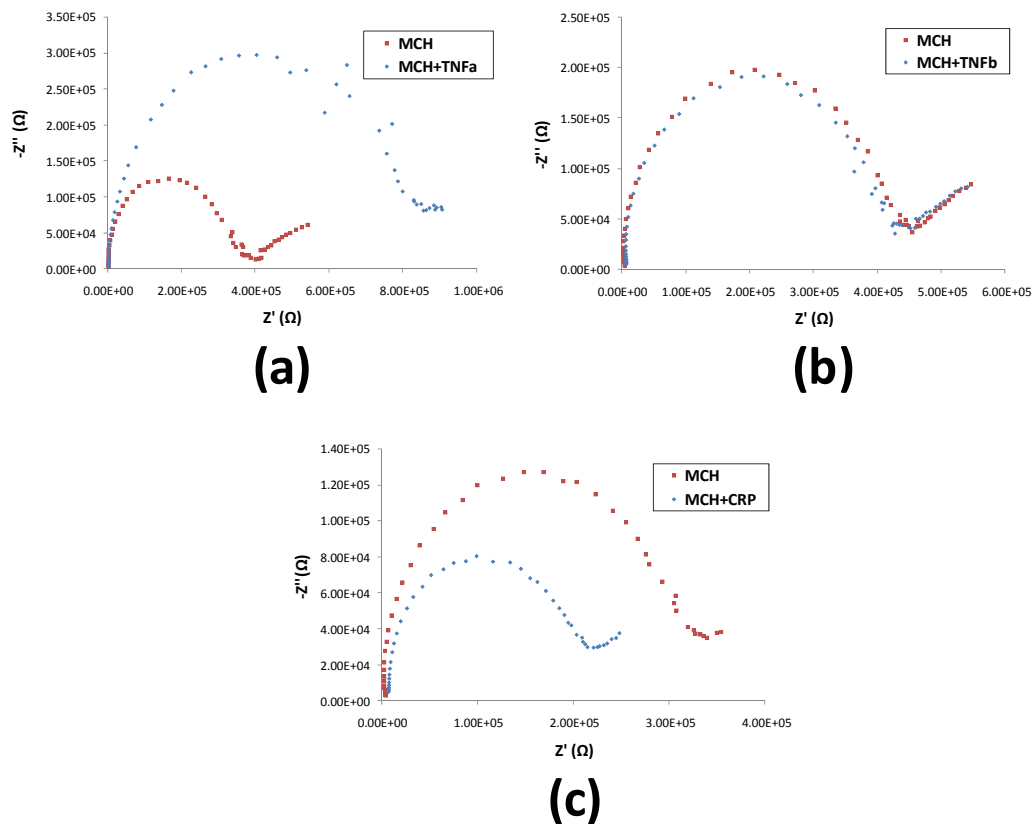


Figure 5.2: Impedance spectroscopy data for electrodes passivated with MCH followed by incubation for 15 minutes with (a) TNF α , (b) TNF β and (c) CRP

5.4.2 Adsorption to BSA

The change in impedance caused by each protein to the BSA surface is seen from the Nyquist plots in Figure 5.3. Each protein yielded only a slight increase in impedance after incubation with the BSA surface. This is attributed to BSA's known ability to reduce adsorption of other compounds to its surface and has been utilized by many groups for this reason as previously mentioned. It should also be noted that the impedance of the BSA surface is much higher (larger R_{ct} value from the Randles circuit) than that of the MCH surface from Figure 5.2. This result is to be expected since BSA is a much larger compound (MW = 70,000) than MCH (MW = 134) and should block more of the redox compound from interacting with the surface. This high impedance can also be used to explain the lack of a linear region in the Nyquist

plot at lower frequencies. The 45° phase response at low frequencies occurs due to diffusion dominated transport of the charge from the redox compound in solution. The BSA molecules provide enough of a physical barrier to the penetration of the redox compounds that diffusion has little overall effect on the measured impedance and thus the linear region is not present at lower frequencies.

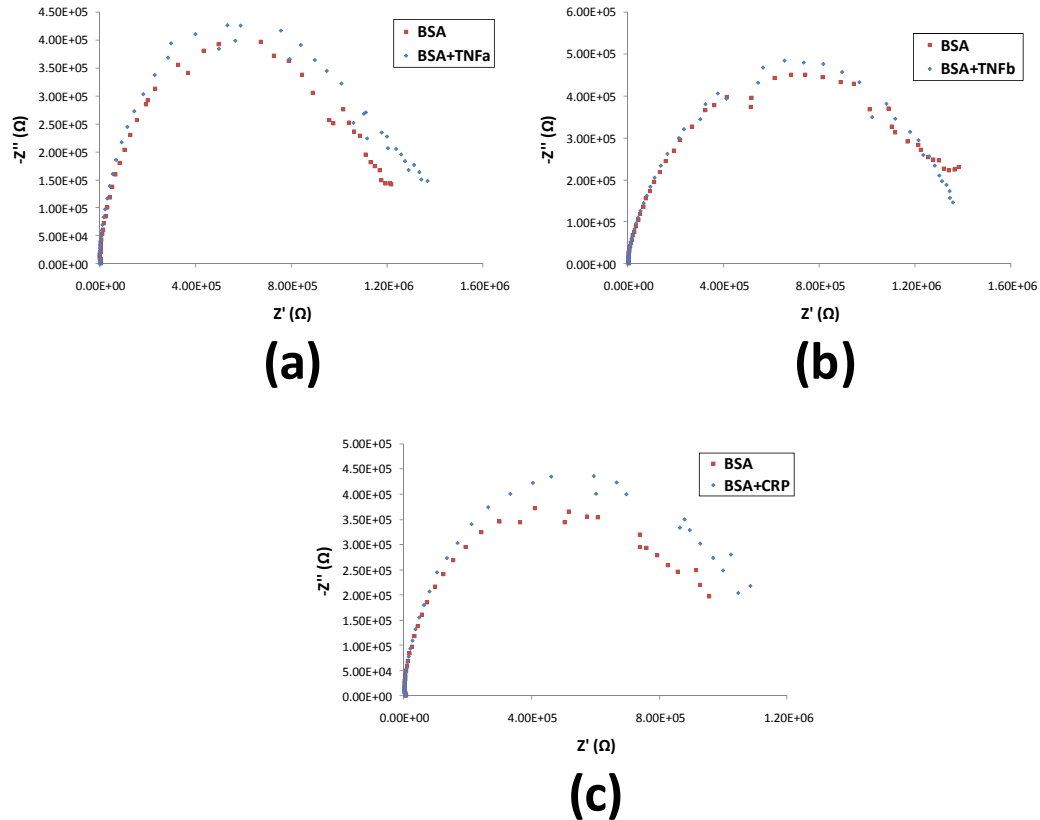


Figure 5.3: Impedance spectroscopy data for electrodes passivated with BSA followed by incubation for 15 minutes with (a) TNF α , (b) TNF β and (c) CRP.

5.4.3 Adsorption to PEG

The change in impedance caused by each protein to the PEG surface is seen from the Nyquist plots in Figure 5.4. For all three proteins studied, the impedance appears to increase greatly after incubation with the PEG functionalized surface. However, it should be noted that the PEG formed an unstable monolayer during testing as evidenced by the large variation in its initial impedance. All three proteins

were able to adsorb strongly to the surface due to this instability. There also appears to be another semi-circular region at high frequencies for the PEG layer on two of the sensors. This suggests a secondary electron transfer reaction taking place in the system from an unknown source. More tests would have to be performed to fully investigate these results, and future studies have been planned to utilize PEG compounds of various length and with different functional head groups to better understand the results obtained in this study. This is discussed in more detail in the future work section of Chapter 7.

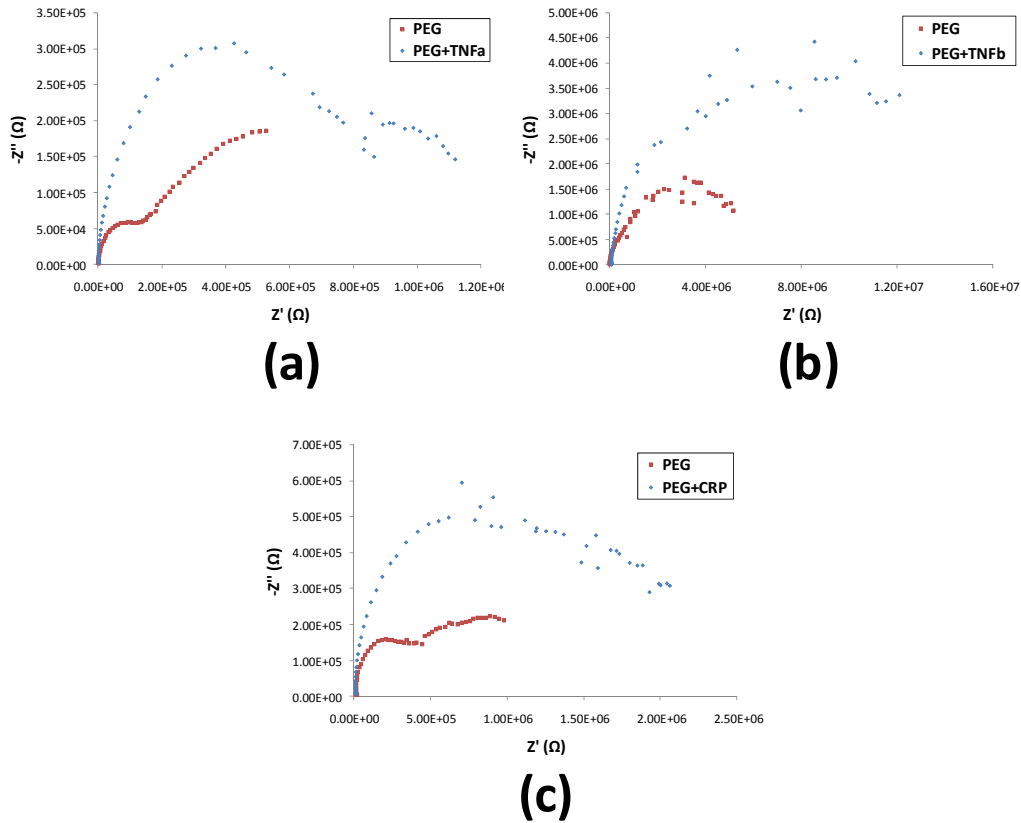


Figure 5.4: Impedance spectroscopy data for electrodes passivated with PEG followed by incubation for 15 minutes with (a) TNF α , (b) TNF β and (c) CRP.

5.5 Data Discussion

All of the collected impedance data was fitted to the Randles lumped circuit model discussed earlier in Chapter 2. The values of R_{ct} and C_d for each surface and

protein tested before and after incubation are shown in Table 1. These values were all extracted from the raw data presented in Figures 5.2 - 5.4. A higher starting R_{ct} value for electrodes covered in BSA vs. those covered with MCH can be attributed to the greater size of BSA proteins vs. the short carbon-chain compound MCH which increases the distance of the redox compound bulk concentration from the electrode surface. The higher C_d value for BSA vs. MCH could be attributed to a higher dielectric effect caused by the presence of the BSA. The capacitance values show little variation following incubation with any of the three proteins for all surfaces.

Table 5.1: Values for the charge transfer resistance (R_{ct}) and double layer capacitance (C_d) for each protein and surface investigated. Values are extracted from the impedance data displayed in Figures 5.2 – 5.4.

Surface	Incubation	TNF α		TNF β		CRP	
		R_{ct}^*	C_d^{**}	R_{ct}^*	C_d^{**}	R_{ct}^*	C_d^{**}
MCH	Before	3.38	6.31	4.16	5.20	2.78	5.46
	After	6.97	6.48	4.00	4.62	1.76	5.01
BSA	Before	8.17	14.90	7.39	15.20	7.06	12.10
	After	9.20	12.60	7.66	16.50	8.25	10.30
PEG	Before	1.16	9.43	13.30	4.01	3.59	5.58
	After	6.63	8.24	41.20	3.62	11.00	4.73

* R_{ct} ($\Omega \times 10^5$) ** C_d ($F \times 10^{-9}$)

Repeated measurements of both the MCH and BSA surfaces with all three proteins were performed using the device and the percent change in R_{ct} was calculated as shown in Figure 5.5. The error bars designate one standard deviation with $n = 3$. This data can be used to discern noticeable trends among the interactions between the surfaces and proteins. TNF β displayed very little impedance change for either surface suggesting little to no adsorption occurring while TNF α displayed the highest impedance increase for both surfaces. CRP consistently displayed a decrease in the impedance with MCH. The BSA surface displays only minor interactions with

all three proteins over the course of numerous experiments. The data for the PEG surface is not included in this figure due to the instability of the layer. It is difficult to compare impedance spectra from various experiments with PEG, as the model could not converge for much of the collected impedance data.

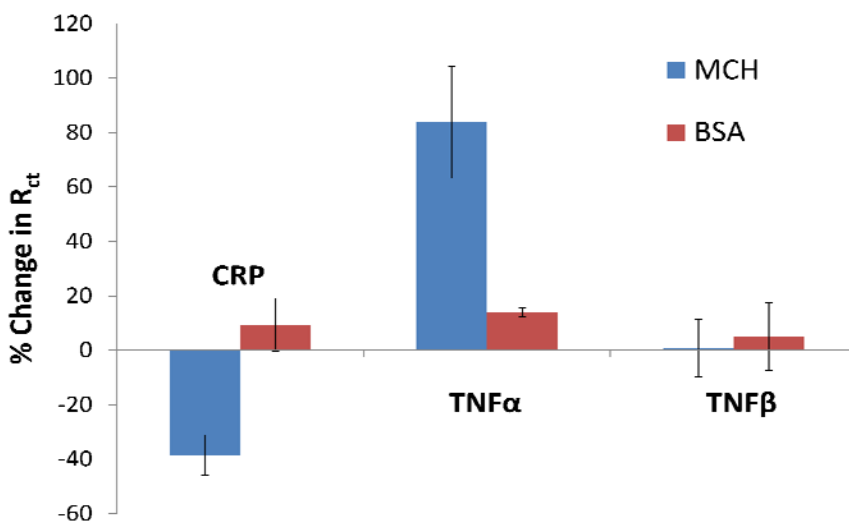


Figure 5.5: Percent change in R_{ct} for adsorption of each protein to both MCH and BSA. Clear trends can be determined including the large impedance increase for TNF α on MCH and impedance decrease for CRP on MCH. All three proteins display roughly the same impedance change for a surface coated with BSA. Error bars designate one standard deviation, n = 3.

The functionalization compounds (MCH, BSA, PEG) and proteins (CRP, TNF α , TNF β) used for this research were chosen to demonstrate the ability of the presented device to electrochemically probe an array of binding interactions. The device was successful in measuring impedance changes for each interaction. The mechanisms regarding both protein adhesion and the effect on the impedance include electrostatic interaction and steric stabilization. The impedance of the system is directly related to the ability for the charged redox compound to exchange electrons with the electrode surface. If the net surface charge is made to be either more positive or more negative, this will either better attract or repel the negative redox compound (in the case of the ferri/ferrocyanide couple) in solution and affect the measured

impedance accordingly. Steric stabilization describes the resistance of polymeric chains to being compressed and has been used to explain why PEG has been demonstrated to resist protein adsorption [110].

The impedance results with MCH from Figure 5 demonstrate the aforementioned electrostatic effect well. Incubation with TNF α displays an impedance increase while incubation with CRP decreases the impedance. The net charge polarity of each protein is different for the conditions used, i.e. the amino acids expressed on the surface of TNF α provide a net negative charge at neutral pH (isoelectric point of 5.01) while those of CRP provide a net positive charge (isoelectric point of 9.2) [32]. The amino acid sequences for each of the three proteins including positively (blue) or negatively (red) charged residues at neutral pH are displayed below.

TNF alpha:

MSTESMIRDVELAEEALPQKMGGFQNSRRCLCLSLFSFLLVAGATTLFCLLNF
GVIGPQRDEKFPNGLPLISSMAQTLTLRSSSQNSSDKPVAHVVANHQVEEQLE
WLSQRANALLANGMDLKDNLVVPADGLYLVYSQVLFKGGQCPDYVLLTH
TVSRFAISYQEKVNLLSAVKSPCPKDTPEGAELKPWYEPIYLGGVFQLEKGDQ
LSAEVNLPKYLDFAESGQVYFGVIAL

Negative Charge: 10D + 15E

Positive Charge: 11K + 3H + 7R

Net Charge: -3

TNF beta:

MTPPERLFLPRVCGTTLHLLLLGLLLVLLPGAQGLPGVGLTPSAAQTARQHP
KMHLAHSTLKPAAHLIGDPSKQNSLLWRANTDRAFLQDGFSLSNNSLLVPTS
GIYFVYSQVVFSGKAYSPKATSSPLYLAHEVQLFSSQYPFHVPLLSSQKMVYP
GLQEPWLHSMYHGAAAFQLTQGDQLSTHTDGIPLVLSPSTVFFGAFAL

Negative Charge: 5D + 3E

Positive Charge: 6K + 11H + 5R

Net Charge: +14

CRP:

MVLGK**P**Q**T**D**P**T**L**E**W**F**L**S**H**C**H**I**H**K**Y**P**S**K**S**T**L**I**H**Q**G**E**K**A**E**T**L**Y**Y**I**V**K**G**S**V**A**V**L**I**K
D**E**E**G**K**E**M**I**L**S**Y**L**N**Q**G**D**F**I**G**E**L**G**L**F**E**E**G**Q**E**R**S**A**W**V**R**A**K**T**A**C**E**V**A**E**I**S**Y**K**K**F**R**Q**
L**I**Q**V**N**P**D**I**L**M**R**L**S**A**Q**M**A**R**R**L**Q**V**T**S**E**K**V**G**N**L**A**F**L**D**V**T**G**R**I**A**Q**T**L**L**N**L**A**K**Q**P**D**A**
M**T**H**P**D**G**M**Q**I**K**I**T**R**Q**E**I**G**Q**I**V**G**C**S**R**E**T**V**G**R**I**L**K**M**L**E**D**Q**N**L**I**S**A**H**G**K**T**I**V**V**Y**G**T**R

Negative Charge: 8D + 16E

Positive Charge: 15K + 6H + 11R

Net Charge: +16 (CRP is a dimer protein containing two identical sub units of this sequence)

The net negative charge on TNF α and the net positive charge on CRP are observed through their respective amino acid sequences. The impedance changes suggest that both proteins interact with the hydroxyl head groups of the MCH and bind to the surface, however, the negatively charged TNF α causes repulsion of the ferricyanide while the positively charged CRP attracts the ferricyanide explaining the opposite impedance changes for each protein. TNF β also carries a net positive charge, however, the protein does not display any interaction with the MCH and so the impedance does not change. Comparatively, the negative charge of TNF α may not appear high, but the electrostatic repulsion is dominated by the amino acid residues expressed on the outer surface of the folded peptide chains. Thus, more of the negatively charged amino acids may reside on the outer surface leading to higher repulsion and greatly increased impedance.

The microfluidic device is very useful for helping one discover what surface modifications specific proteins show little to no interaction with. TNF β from Figure 5.5 does not cause any measureable impedance change to a MCH functionalized surface. This is an interesting result given that it shares nearly 28% of its amino acid

sequence with $\text{TNF}\alpha$ and both versions of TNF bind to the same receptors [166]. Neither $\text{TNF}\beta$ nor CRP adsorb to the electrode surface passivated with BSA. $\text{TNF}\alpha$ displays some increased impedance with a BSA passivated electrode due to its high repulsion of the redox compound, but the effect is far less than that observed with the MCH surface.

The values for the electron transfer resistance and double layer capacitance in Table 5.1 for each of the impedance measurements were obtained by fitting the data to the Randles model using the potentiostat's software program. However, this model is not always the most accurate way to describe every environmental situation. In this study, the electrode surface was densely covered by the passivation compounds used, especially when using BSA. This can be observed in the Nyquist impedance plots from the lack of a linear region at low frequencies. The absence of this linear region suggests that the diffusion of the redox compound has been almost completely blocked by the surface passivation. In order to more accurately model this scenario, the circuit shown in Figure 5.6 was utilized.

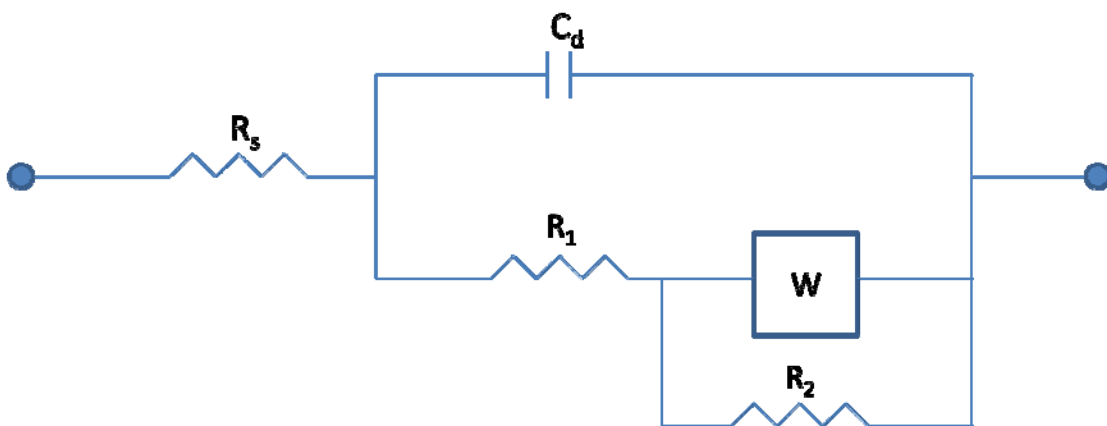


Figure 5.6: Modification of the Randles circuit to more closely model the collected impedance data. The same solution resistance (R_s), double layer capacitance (C_d) and Warburg impedance (W) from Figure 2.7 are used, but the resistance contribution from R_{ct} has now been split amongst R_1 and R_2 .

A resistor (R_2) has been added in parallel with the Warburg impedance element. This resistance reduces the effect that the Warburg impedance has on the system and more accurately models a situation in which diffusion is not the dominant mechanism at lower frequencies. The modeling of the charge transfer resistance has now been split amongst the two resistances R_1 and R_2 . Figure 5.7 displays how the circuit model in Figure 5.6 better fits the raw impedance data than the conventional Randles circuit from Figure 2.7.

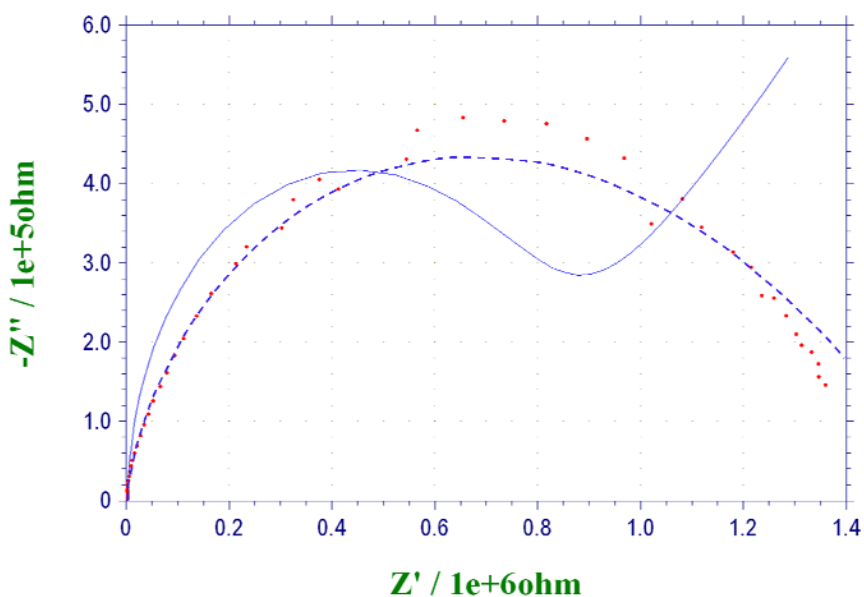


Figure 5.7: Impedance spectra for an electrode passivated with BSA including the fitted curve for two circuit models. The solid line displays the fit using the Randles circuit from Scheme 1 while the dotted line displays the fit using the improved circuit from Scheme 2. The improved fit results in a 4x reduction of the fitting error.

This impedance data is taken from an electrode passivated with BSA. A 4x reduction in the fitting error was achieved when using the circuit from Figure 5.6 vs. the circuit from Figure 2.7. The average percent error for fitting all of the data collected was reduced from 14.6% to 5.3% for BSA passivated surfaces and from 8.1% to 6.5% for MCH passivated surfaces by using the improved circuit model. The error is calculated by the impedance fitting program by comparing the fit data to the experimental data using equation 5.1.

$$error = \frac{\sqrt{\frac{\sum (F-E)^2}{E^2}}}{N} \quad (5.1)$$

Where F is the fitted data, E is the experimental data and N is the total number of data points. This error calculation is very similar to the standard deviation of a population.

5.6 Sensor Reusability

Another advantage of having integrated electrical sensors is the ability to refresh the sensor surface via an applied potential. Typically, an electrode surface is electrochemically cleaned by dipping the electrode into a 1 M sulfuric acid solution while potential is cycled vs. a Ag/AgCl reference [116]. However, sulfuric acid is too caustic for use with PDMS, so a similar cleaning procedure was achieved by cycling the potential applied to the working electrode well above and below the formal reduction potential of ferricyanide in PBS. Figure 5.8 displays cyclic voltammograms of an electrode surface demonstrating passivation with a high concentration (1mM) of PEG and subsequent regeneration of the current response due to electrochemical cleaning.

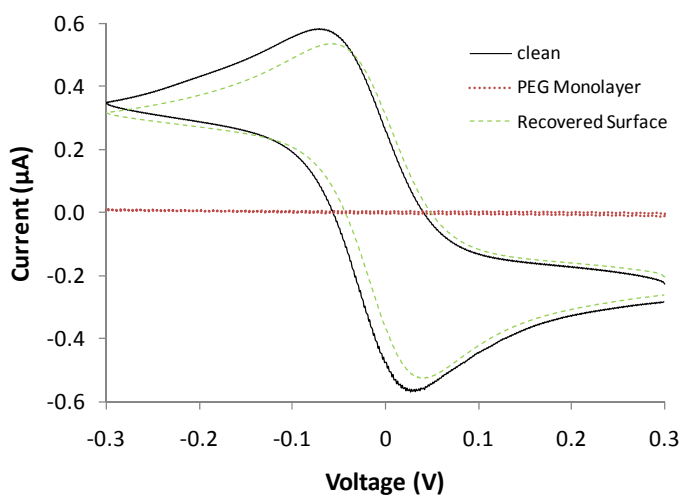


Figure 5.8: Cyclic voltammetry measurements of a blank electrode (solid), the response after incubation with PEG (dotted), and the final response after applying a high switching potential (0.8 to -0.8 volts) to the electrode (dashed).

PEG was chosen due to its high packing density at higher concentrations. The layer becomes so dense that there is little to no penetration of the ferricyanide to reach the electrode surface as evidenced by the lack of any measurable current response after PEG binding. After electrochemically cycling the sensor surface between -0.8 and 0.8 volts vs. platinum, the current peaks were almost completely regenerated. Higher cycling potentials began to anodize the gold which damaged the surface. The potentials at which this anodization can occur vary depending on the surface area of both the counter and working electrodes. For this reason, it is recommended to slowly increase the cycling potential for each sensor until the CV plot is recovered. Regeneration was observed for electrodes passivated with MCH and BSA as well.

5.7 Summary

This chapter has covered the use of the microfluidic device for observing protein interactions with various surface types. The interaction between a commonly studied bacterial gene regulator (CRP) and two cancer marker proteins (TNF α and TNF β) was observed to three modified electrode surfaces (MCH, BSA and PEG) using impedance spectroscopy. Each protein repeatably demonstrated a different impedance change with the MCH surface, while none of the proteins greatly changed the impedance of the surface passivated with BSA. The PEG layer proved to be too unstable for any definite conclusion. Re-programmability of the sensor surface by applying a high sweeping potential between -0.8 and 0.8 volts vs. platinum has also been demonstrated.

6 DNA Hybridization Study

6.1 Introduction

The devices fabricated in this research are also used to perform DNA hybridization sensing. This chapter covers all aspects of this study starting with details about the DNA sequences and buffers used. Attachment procedures specific to the DNA study are discussed next. The hybridization data is finally examined for all stages of device design including the macroscale electrodes, and the microfluidic device both before and after the integration of valves. Experiments using multiple target ssDNA concentrations to determine the limit of detection for the microfluidic sensor were performed with help from my colleague at the MEMS Sensors and Actuators Lab, Hadar Ben-Yoav.

6.2 DNA Sequences and Buffers

All DNA used in this study was purchased from Integrated DNA Technologies (Coralville, IA). One strand for each pair contains a thiol modification at the 3' end for self assembly onto the gold electrode as discussed in Chapter 2. A few of the complementary strands contain a fluorescent label to confer visual confirmation of hybridization.

Three unique DNA sequences were created to perform the arrayed hybridization sensing. A fourth sequence was also created which included a fluorescent probe modification on the 5' end of the complementary strand in order to help characterize the assembly optically. Nucleotide bases consist of adenine (A), thymine (T), guanine (G) and cytosine (C) with adenine bonding to thymine and

guanine bonding to cytosine via hydrogen bonds. The sequences and their labels are listed below.

ssDNA1_T: 5'-/5ThioMC6-D/AAAGCTCCGATAGCGCTCCGTGGACGTCCC-3'
ssDNA1: 5'-GGGACGTCCACGGAGCGCTATCGGAGCTTT-3'

ssDNA2_T: 5'-/5ThioMC6-D/ACGCGTCAGGTCATTGACGAATCGATGAGT-3'
ssDNA2: 5'-ACTCATCGATTTCGTCAATGACCTGACCCGT-3'

ssDNA3_T: 5'-/5ThioMC6-D/ACCTAGATCCAGTAGTTAGACCCATGATGA-3'
ssDNA3: 5'-TCATCATGGGTCTAACTACTGGATCTAGGT-3'

ssDNAop_T: 5'-/5ThioMC6-D/AAAATAGCATAAATTGTGATCTATTCGGAAA
TATGTGCAATGTC-3'
ssDNAop: 5' -/5TEX615/GACATTGCACATATTTCCGACGAATAGATCACAAT
TTATGCTATTTT-3'

The label names given to each strand will be used from this point onward in the dissertation. The ssDNAop_T and ssDNAop strands contain 47 base pairs each while the first three DNA sequences all only contain 30 base pairs. During the early stages of this research, longer DNA strands were used but eventually shortened after it was determined that the yield from the company was greater for shorter sequences. Hybridization of shorter DNA sequences is also less prone to tangling.

The DNA is shipped as a lyophilized powder and is re-suspended to a concentration of 100 μ M using a buffer containing: 10 mM Tris, 50 mM NaCl and 1 mM EDTA. Afterwards, aliquots of 20 μ l each are frozen at -15 C. The attachment buffer for self assembly of the thiol ssDNA on the electrode contains: 10 mM PBS, 100 mM NaCl and 10 μ M Tris (2-carboxyethyl) phosphine (TCEP). The TCEP is a reducing agent that cleaves the disulfide bond at the end of the ssDNA strand and expresses the free thiol group. Without this agent, the disulfide bonds of the ssDNA will still assemble on the electrode, but the bond is much weaker than the thiol-gold

bond and will not remain stable throughout the experiment. The buffer used for immobilizing mercaptohexanol (MCH) as a backfilling material contains: 10 mM PBS, 100 mM NaCl and 1.395 mM TCEP. Further discussion about the use of MCH for backfilling is found in the next section. All DNA hybridization events were performed in 4x saline sodium citrate (SSC). This buffer is diluted from a 20x SSC stock solution created with 3M sodium chloride and 0.3 M trisodium citrate.

6.3 Hybridization Testing Procedure

This section describes the procedure used for performing the DNA hybridization experiments with both the macroscale electrodes and microfluidic device. The three main steps include immobilization of the ssDNA probes, backfilling the electrode with MCH, and hybridization with the target sequence. Further considerations are explained when using the microfluidic devices due to the diffusion limited regime within the channels over the electrodes.

6.3.1 DNA probe immobilization

6.3.1.1 Macroscale electrodes

A patterned working electrode chip is placed into 500 μ L of attachment buffer containing 1 μ M of thiol ssDNA. The chip should be cleaned using piranha prior to any attachment procedure. The ssDNA is allowed to incubate with the working electrode surface for at least one hour. Incubation times between one and two hours were found to be sufficient for forming a stable ssDNA monolayer for hybridization detection and are common incubation periods used by other groups [25, 139].

Afterwards, the electrode is rinsed with PBS solution to remove any unbound molecules from the surface.

A probe ssDNA concentration of 1 μM was chosen based on studies performed by other groups demonstrating a high surface density of molecules as shown in Figure 6.1 from work performed by Ricci *et al.* [139]. Intuitively, the figure also shows that the separation distance between probes is the lowest for higher packing densities. Although an optimized hybridization signal may be obtained for lower packing densities due to easier access to the probes, it was not explored in this work and hybridization was observed nonetheless for a surface density of approximately 3×10^{12} molecules/ cm^2 . Furthermore, Ricci *et al.* observed a higher hybridization signal for the higher surface densities albeit requiring a longer incubation period with the target sequence to achieve equilibrium.

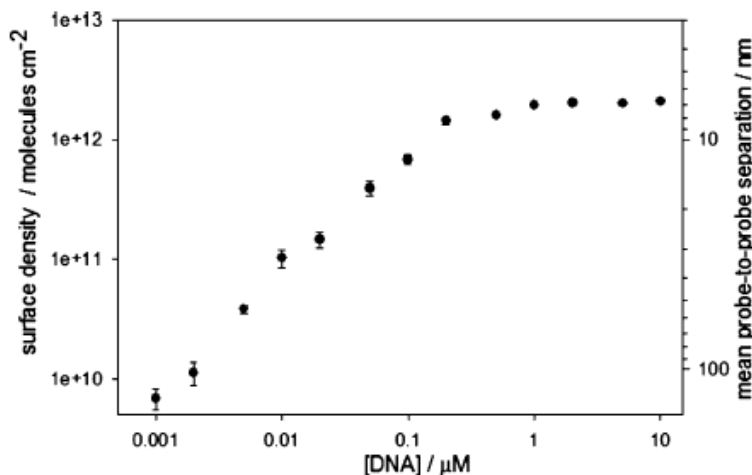


Figure 6.1: Surface density and separation of thiol-DNA probe molecules for a given concentration during incubation over a gold electrode for 1 hour. Reproduced from [139].

The thiol DNA (by nature of its strong covalent bond with gold) produces a much higher monolayer density on the electrode surface vs. passive adsorption of the ssDNA. Impedance data for an electrode with either adsorbed ssDNA or thiol bonded ssDNA is shown in Figure 6.2. The adsorbed ssDNA molecules increase the

impedance slightly from that of the blank electrode, but the thiol ssDNA creates nearly an order of magnitude higher impedance due to the formation of a densely ordered monolayer.

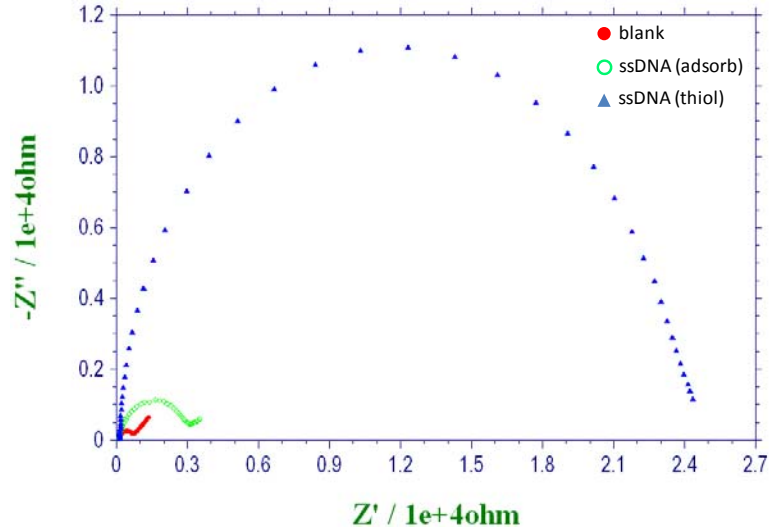


Figure 6.2: EIS results of a blank macro-scale electrode (●) after either adsorbed DNA (○) or thiol-terminated DNA (▲).

6.3.1.2 Microfluidic electrodes

The DNA probe immobilization procedure for the microfluidic device is similar to the macroscale case. A solution containing 1 μ M of the thiol ssDNA is introduced into the channel using a syringe at a flow rate of 200 μ l/hr. Once the fluid has completely filled the channel, the flow rate is stopped and the sample is allowed to incubate over the exposed electrodes for 1 hour. It was found through testing that any movement of the liquid greatly disrupted the monolayer formation and caused too few probes to be strongly bound to the surface. After 1 hour, the channel is flushed with PBS at a flow rate of 200 μ l/hr for 1-2 minutes to remove any unbound molecules from the surface of the electrodes.

6.3.2 MCH backfilling

Once the ssDNA probes have been assembled onto the electrode, a second compound is used to passivate any exposed regions on the surface to reduce non-specific binding effects. Mercaptohexanol (MCH) is commonly used for this purpose [29, 116, 117, 167]. The compound consists of a short chain of 6 methyl (CH_2) groups with a thiol at one end and a hydroxyl ($-\text{OH}$) head group at the other. The thiol group allows for self assembly onto the gold and the hydroxyl group reduces non-specific adsorption of the ssDNA in solution. This passivation is crucial for establishing a stable impedance baseline measurement of the sensor, reducing false positive signals and removing any weakly bound molecules from the surface.

The electrode containing the immobilized probe DNA is incubated in a 500 μL solution containing 1 mM MCH in a buffer of 10 mM PBS, 100 mM NaCl and 1.395 mM TCEP for 1 hour. For the microfluidic devices, 1 mM of MCH in the same buffer is injected into the channel using a syringe and allowed to sit over the electrodes with no added flow for 1 hour. The high TCEP concentration is used to reduce the thiol groups that may have oxidized to form disulfide bonds. It was discovered that without the high TCEP content in the buffer, the MCH would form unstable monolayers and the impedance data would vary accordingly. The thiol groups of MCH oxidize slowly over time, so the high TCEP content may not be required for freshly purchased MCH, however, in this research the MCH was used over the course of more than a year necessitating the use of TCEP.

The MCH has another important function when using it as passivation with ssDNA molecules. The oxidative adsorption process of the MCH injects electrons

into the electrode and reduces the surface potential. This causes an electrostatic effect with the anionic probe ssDNA already immobilized and the ssDNA stands upright away from the electrode. This phenomenon has been studied in depth by Arinaga *et al.* [168]. Upright probes greatly increase the hybridization efficiency since the target ssDNA strands have much easier access to the entire length of the probe sequence. The open circuit potential of the fabricated macroscale gold electrode was measured vs. Ag/AgCl before and after MCH immobilization using only 10 mM PBS as the electrolyte (no added redox compound). The potential decreased from -38.8 ± 0.05 mV down to -303.5 ± 4.5 mV after the MCH immobilization. The more negative electrode potential will cause the ssDNA probe molecules to stand upright and improve the hybridization results.

6.3.3 Hybridization Reaction

6.3.3.1 Macroscale Electrodes

Following the MCH immobilization, the chip is placed in a 500 μ L solution containing 1 μ M of target DNA in 4x SSC buffer for 20 minutes. The hybridization reaction was performed at room temperature and also in an incubator at 37 C. The elevated temperature did not change the observed hybridization signal and so all experiments have been performed at room temperature.

In order to receive visual confirmation of the hybridization reaction, the sequence ssDNAop_T was immobilized onto a gold electrode and allowed to hybridize with its target ssDNAop which included a fluorescent probe. The fluorophore chosen was TEX615 due to its low cost and common emission spectra around 615 nm. After hybridizing the DNA on the electrode surface, the chip was

taken to a fluorescent microscope (Zeiss model 310) in order to capture a picture of the assembled DNA. Figure 6.3 below demonstrates how the DNA is only assembled onto the gold electrode area.

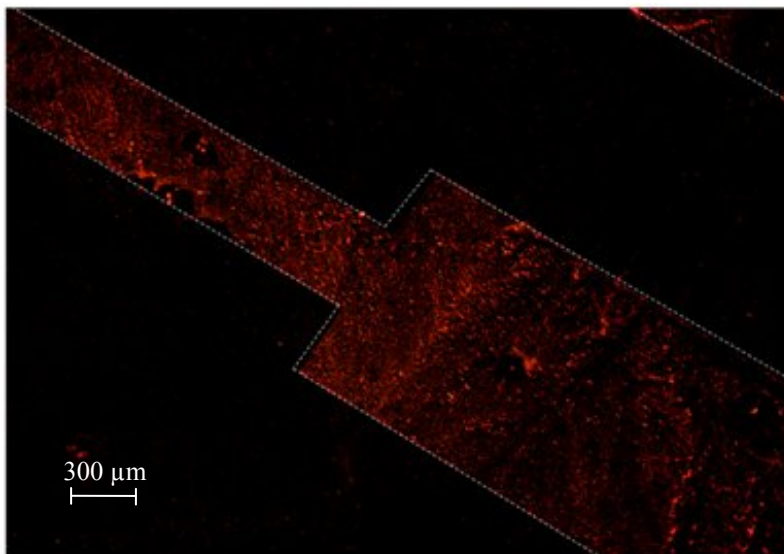


Figure 6.3: Fluorescent microscope image of TEX615-labeled DNA assembled on gold electrodes outlined in white.

6.3.3.2 Microfluidic electrodes

The hybridization in the microfluidic device was performed using $1 \mu\text{M}$ ssDNA target in 4x SSC buffer. The sample was allowed to incubate over the electrodes in the channel for 20 minutes. After the incubation period, the channel was flushed using PBS for 1 – 2 minutes at $200 \mu\text{l/hr}$.

The reaction kinetics are quite different in a microfluidic channel versus those found with the macroscale electrode in the beaker. A large bulk solution exists over the electrode surface when using the beaker and the slow diffusion process dominates the transport of the target ssDNA strands to the probes immobilized on the electrode surface. Due to the amount of bulk solution, the concentration gradient is easily replenished over time as the molecules bind. In the microfluidic device, the concentration gradient is severely limited by the enclosed geometry of the channel so

a small flow rate is typically added to continually replenish the ssDNA concentration. The transport of the ssDNA target to the immobilized probes in solution is now governed by two transport mechanisms: molecular diffusion of the molecules and convection in the direction of the fluid flow. For this type of transport, the Peclet number, Pe , a measure of the relative rate of convective to diffusive transport, is given as:

$$Pe = \frac{U_m H}{D} \quad (6.1)$$

Where U_m is the mean fluid velocity, H is the height of the channel and D is the diffusion coefficient. The mean fluid velocity can be calculated by dividing the volumetric flow rate by the cross sectional area of the channel given as:

$$U_m = \frac{Q}{wH} \quad (6.2)$$

Where Q is the volumetric flow rate, w is the width of the channel and H is the height of the channel. According to a study of DNA hybridization in a microfluidic channel performed by Kim *et al.*, the best hybridization results were obtained for Peclet numbers that fell between 50 and 100 [119]. It was discovered through testing that DNA hybridization was observed in the microfluidic device with no added flow. This is attributed to the large channel cross-section dimensions (100 μm x 500 μm) allowing for a large diffusion gradient to exist. Further tests to improve the hybridization efficiency via an applied flow rate with the device were not performed, but could be the basis for future research. However, after the integration of the valves, the microfluidic channel becomes much smaller and diffusion plays a much greater

role. Using the cross sectional area from the valved device, a linear flow velocity of 0.67 mm/s is calculated for achieving the most efficient hybridization based on the Peclet number.

In order to achieve a 0.67 mm/s linear flow velocity in the valved microfluidic device, a flow rate of 17 $\mu\text{l/hr}$ is required (computed using the cross sectional area of the rounded channel). Therefore, hybridization was performed in the valved microfluidic device under a continuous flow rate of 17 $\mu\text{l/hr}$ applied over the course of 20 minutes.

6.4 Macroscale DNA Hybridization Results

During a typical experiment, a baseline electrochemical measurement is collected of the chip containing the ssDNA probe sequence and MCH backfilling followed by incubation with a non-matching target sequence and subsequent measurement and ending with incubation of the matching target sequence and a final measurement. It is always important to compare the non-matching sequence measurement with the baseline to ensure that any change in the signal is not due to non-specific adsorption.

Figure 6.4 below displays CV data and the complementary EIS data for a macroscale electrode chip incubated first with non-matching, then matching DNA sequences for 20 minutes each.

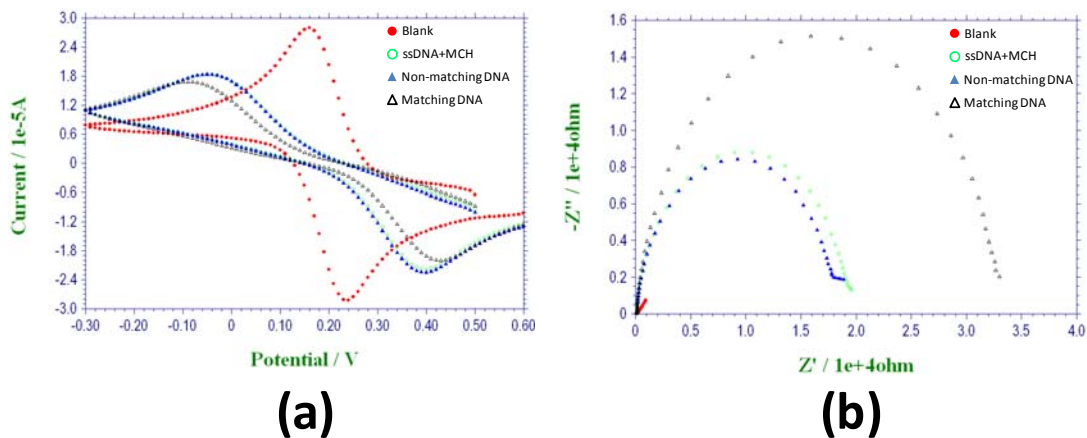


Figure 6.4: (a) CV results and (b) EIS data for a blank electrode (●), after ssDNA probe and MCH immobilization (○), after incubation with a non-matching sequence (▲) and after incubation with a matching sequence (△). The binding event is more clearly observed using EIS.

The CV data of Figure 6.4a demonstrates good agreement with the simulation results discussed in Chapter 2. The first monolayer consisting of probe DNA and MCH causes a large reduction in the peak heights and large separation in the peak potentials. The addition of charged ssDNA molecules upon hybridization causes a further decrease in current and slight separation of the peaks. The change in impedance shown in Figure 6.4b displays a greatly increased result upon hybridization that is more apparent than the CV data. This clear impedance result upon hybridization is related to the high sensitivity of EIS to surface coverage and charge.

Each of the three purchased DNA sequences (ssDNA1, ssDNA2 and ssDNA3) were incubated with three separate sensors each containing one of the three probe DNA molecules as seen in Figure 6.5. In this way, each probe sequence is tested against both non-matching sequences, and ultimately, its matching sequence.

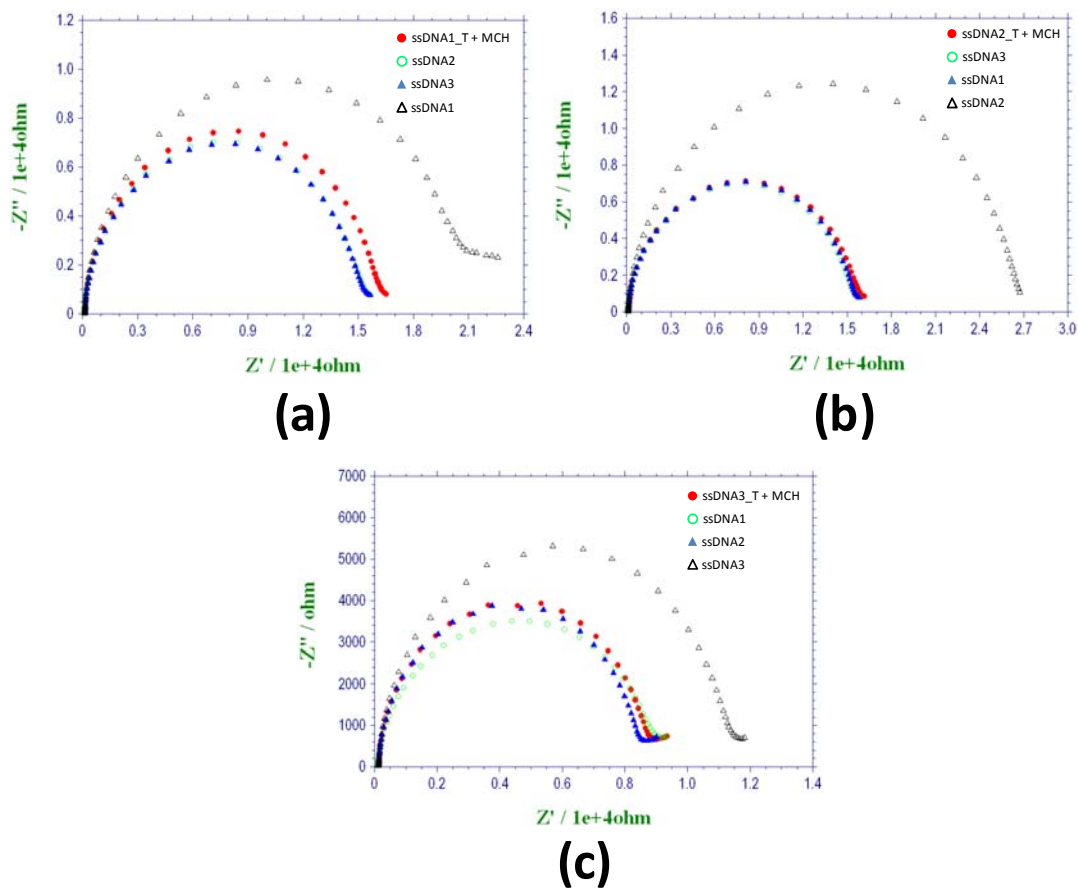


Figure 6.5: EIS data for three electrodes immobilized with (a) ssDNA1_T, (b) ssDNA2_T and (c) ssDNA3_T. Each sensor is incubated in both mis-matching sequences and the final matching sequence.

Each sensor demonstrates only a slight change in impedance when incubated with both mis-matching target sequences as compared to the large impedance change after incubation with the matching target sequence. The various starting impedance values for each monolayer should also be noted. Assembly of DNA3_T displayed a lower starting impedance than either of the other probe sequences. This is attributed to either a poor electrode surface condition or possible degradation of the thiols for that particular batch of ssDNA. In either case, hybridization was still observed even when the surface coverage is not as high.

The EIS plots were each fitted to the Randles equivalent circuit (Figure 2.7) in order to extract the charge transfer resistance (R_{ct}) for each measurement. Figure 6.6

displays the percent change to R_{ct} after each incubation for all three ssDNA targets against all three probe sequences.

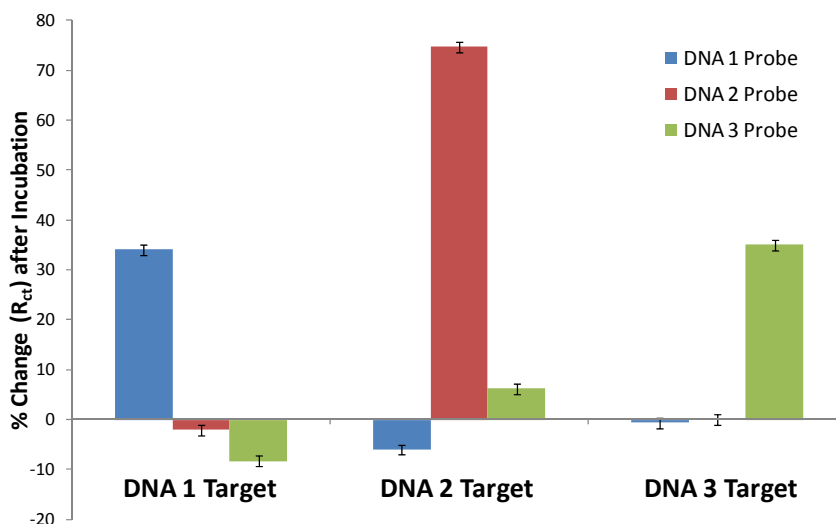


Figure 6.6: Bar graph displaying % change in R_{ct} following each target DNA incubation for each probe sequence. Hybridization events are clearly observed for matching target-probe sequences.

The error bars designate one standard deviation over three scans. Increases in the change transfer resistance of 34%, 75% and 35% are observed when the probe sequences (ssDNA1_T, ssDNA2_T and ssDNA3_T) are incubated with their matching target ssDNA sequences. R_{ct} decreases in some cases after incubation with a non-matching sequence. These decreases could be the result of cationic molecules from the salt buffer adsorbing to the surface, however, any decrease seen in R_{ct} is a clear indication that no further ssDNA is being immobilized on the surface (since any immobilization of the anionic ssDNA will always cause an increase in R_{ct} with the negatively charged ferri/ferrocyanide couple). The larger increase seen in the impedance for DNA2 hybridization is interesting and may be related to its random base pair sequence having a higher binding affinity than that of the other two sequences.

6.5 Microfluidic DNA Hybridization Results

Results from DNA hybridization experiments using multiple sequences in the same device were performed in the microfluidic device. Hybridization data was also collected after the integration of valves with the device. This data is discussed and compared to that collected from the device without valves to draw conclusions on how changes in the diffusion volume alter the formation of the monolayers and affect the impedance measurement.

6.5.1 Non-valved Microfluidic Device

The three probe ssDNA sequences were incubated over columns of electrodes in three separate channels followed by MCH passivation in each channel. After the channels were rotated 90 degrees, each of the three target ssDNA sequences were flown down the three channel rows. The impedance data for each of the 9 sensors was taken before and after the target ssDNA was introduced with the results shown in Figure 6.7. The graphs are displayed in the same 3 x 3 grid as the sensor array. Each sensor column contains the immobilized probes ssDNA1_T, ssDNA2_T and ssDNA3_T in order from left to right. From top to bottom, the target sequences ssDNA1, ssDNA2 and ssDNA3 are flown down each sensor row. A clear increase in impedance is observed only for the sensors in which a matching probe-target pair is made (along the diagonal of the array). These experiments were all performed in parallel allowing each row to provide two control non-matching sequences and one correct matching sequence for each incubation.

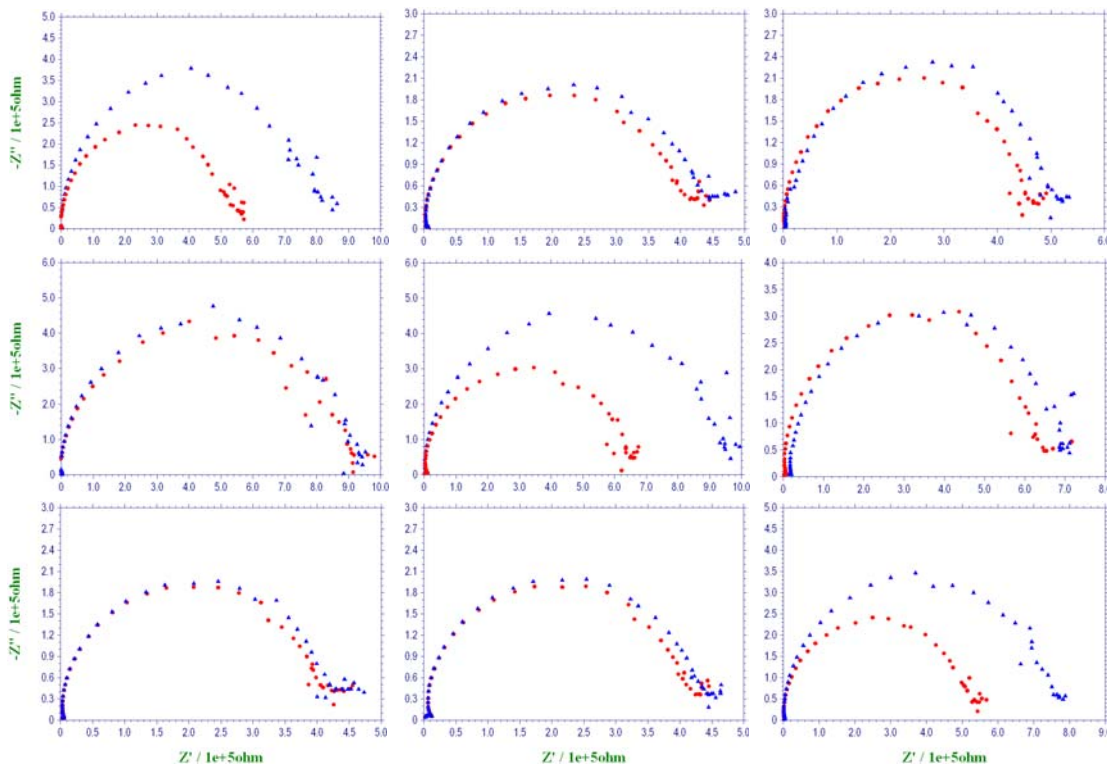


Figure 6.7: EIS plots for each electrode surface before (●) and after (▲) incubation with the target ssDNA sequence. Each column of sensors is immobilized with a different probe sequence while each row is incubated with a different target ssDNA sequence.

The Randles circuit was used to fit the impedance data collected and the R_{ct} value was extracted for each baseline scan and subsequent scan after incubation with the target ssDNA. The percent change of R_{ct} in each case is provided in Figure 6.8.

The error bars designate one standard deviation over 3 measurements. The error is much larger when using the microfluidic device as opposed to the beaker study and can be attributed to the smaller electrode surface making it more sensitive to RF noise especially at low frequencies. Nonetheless, the hybridization events are very clear and display large increases of R_{ct} for each of the three target-probe pairs. Also of note is the fact that the impedance always increased even upon incubation with a non-matching sequence. This result is expected since the ssDNA targets are exposed to all three electrodes (working, reference and counter) in the channel and

some adsorption to the counter electrode will occur, causing a slight increase to the impedance.

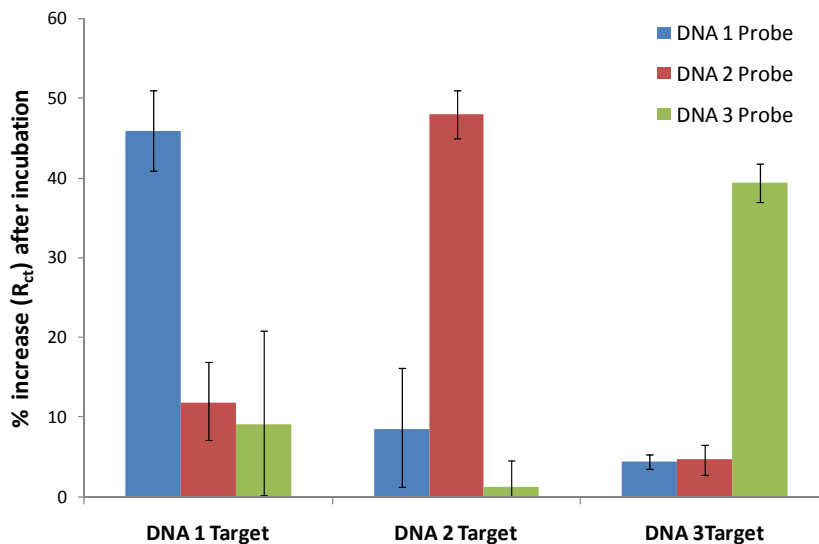


Figure 6.8: Bar graph showing % change in R_{ct} after incubation with each target ssDNA sequence for each probe sequence.

These results from the microfluidic device demonstrate true arrayed detection of multiple DNA sequences using a single device. What makes this type of arrayed detection unique is the ability to detect the hybridization events without the need for labels of any kind. This reduces the time needed to perform the experiment and the number of steps required to measure a signal. Qualitative data regarding the hybridization efficiency can be determined from the shape of the Nyquist impedance plots while quantitative data can be achieved by fitting the measured impedance to a circuit model and comparing specific elements. The analysis time depends on the software of the potentiostat and the measurement time can be reduced even further by using a multi-channel potentiostat capable of measuring numerous 3-electrode systems in parallel.

The dependence of the impedance change on the target ssDNA concentration was also determined using the patterned sensors in the device. Probe ssDNA (1 μM)

and MCH (1 mM) were immobilized onto a single working electrode. Complementary target ssDNA sequences with concentrations of 0.01 μM , 0.1 μM , 1 μM and 10 μM were sequentially incubated over the sensor for 20 minutes each. EIS measurements were taken of the probe monolayer surface and after each incubation with the results shown in Figure 6.9.

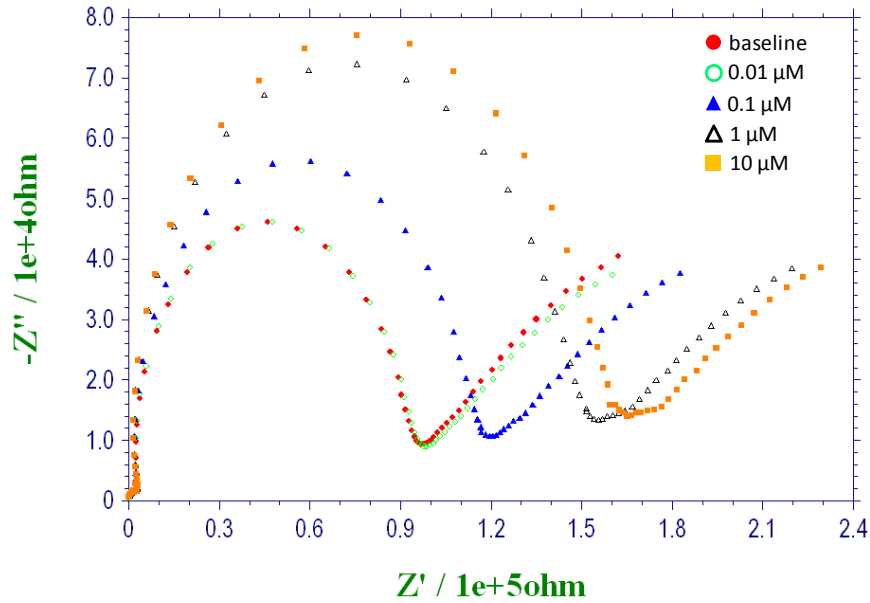


Figure 6.9: EIS data of a single working electrode in the non-valved microfluidic device. Incubation with increasing concentrations of the complementary target ssDNA causes increasing impedance until saturation at 10 μM .

In order to increase the sensitivity of the measurement (for the binding of low target ssDNA concentrations), EIS was performed using 5 mM of the ferri/ferrocyanide redox couple as opposed to 2.5 mM. Furthermore, the amplitude of the AC signal was increased from 5 mV to 25 mV and the software averaged over three collected points for each frequency. The frequency was also swept as low as 0.1 Hz in order to better visualize the linear diffusion controlled region of the plot.

The impedance increases after each incubation with a higher target concentration. The increase is very small for the lowest concentration used (0.01 μM) while the highest concentration (10 μM) does not display as large of an increase from

the previous measured concentration. It appears that the available probe sites on the sensor surface have saturated during the 10 μM incubation as evidenced by the slight increase for such a large target concentration. This effect is even more observable when examining the charge transfer resistance (R_{ct}) from the Randles circuit for each concentration as shown in Figure 6.10.

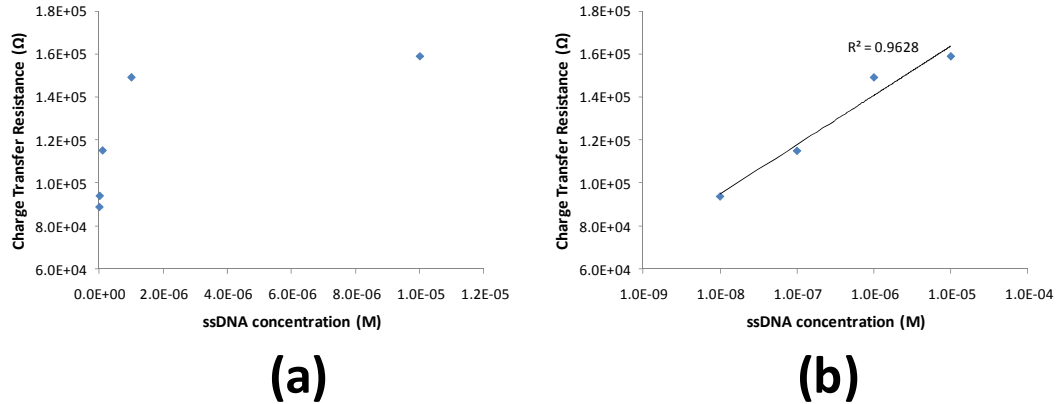


Figure 6.10: (a) Values of charge transfer resistance for each concentration which includes a zero concentration data point corresponding to incubation with a non-complementary target. (b) Logarithmic dependence of the charge transfer resistance on the target concentration observed via high linear correlation on the log scale.

The data shown in Figure 6.10a follows the common curve for an affinity based binding event. Saturation of the available binding sites occurs for high target concentrations and the data follows a logarithmic pattern. Figure 6.10b displays a highly linear correlation of the data when plotted on the logarithmic scale as expected.

The limit of detection for the sensor was calculated by measuring the change in the R_{ct} value when incubating with a non-complementary ssDNA target. This value was observed to be 3970 Ohms and is considered to be the noise level of the sensor. By using this value within the linear regression equation fitted to the plotted data, the limit of detection was determined to be 8 nM.

6.5.2 Valved Microfluidic Device

Numerous DNA hybridization experiments were performed using the device following the integration with valves in order to characterize the binding events within the smaller channels. As previously discussed, the microfluidic channels for the valved device have a cross sectional area of $6,458 \mu\text{m}^2$ while the channels used for the non-valved device have a cross sectional area of $50,000 \mu\text{m}^2$. It became clear soon after testing that the smaller microfluidic channel geometries made it very difficult to achieve stable monolayer assembly on the sensor surface.

Probe ssDNA was immobilized onto an electrode in the valved device followed by MCH incubation, each for 1 hour. The electrode was incubated sequentially with two different non-complementary target sequences followed by the complementary target sequence for 20 minutes each with no flow. The impedance was measured between each incubation. The results are shown below in Figure 6.11.

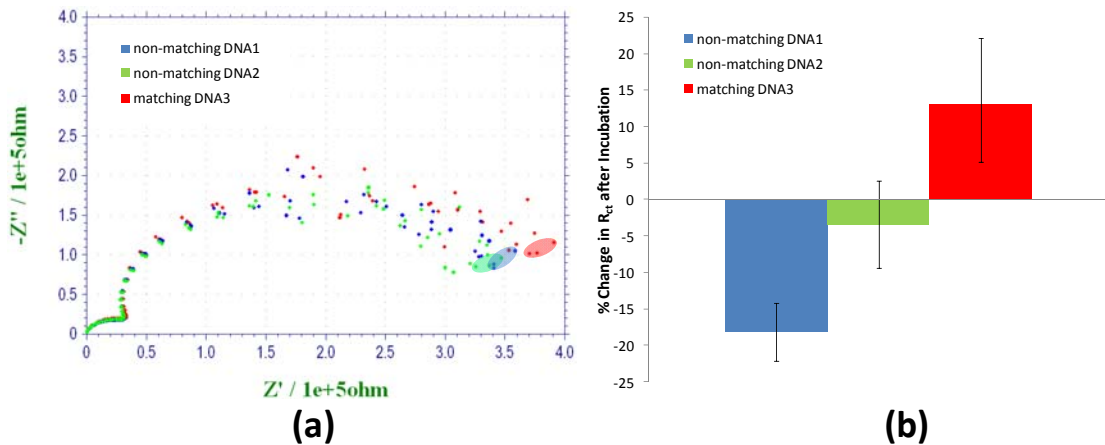


Figure 6.11: (a) EIS data displaying three scans each for two non-matching DNA incubations and the matching DNA incubation. The lowest frequency points are highlighted. (b) The percent change in the fitted R_{ct} value after each incubation.

Three EIS scans are taken for each incubation making a total of nine curves displayed in Figure 6.11a. There are two noticeable areas of the curves. The first is the smaller semi-circular region at high frequencies which was often observed when

taking EIS measurements in the small microfluidic channels. The geometry of the channels increases the resistance between the electrodes and may contribute to this effect when the applied frequency is high and dominated entirely by charge transport (not diffusion). The second region is the lower frequency semi-circular curve which displays more noise than the higher frequencies. This noise is reduced in later experiments by unplugging the syringe pump and taking multiple scans at each frequency. However, even with the noise, it is observed that the incubation with the matching DNA sequence slightly increases the impedance. The extracted R_{ct} values decreased after incubation with two mis-matching sequences and only showed an increase after incubation with the matching sequence.

The increase seen in the impedance is very low from this early experiment with the valved device. In an attempt to achieve higher hybridization efficiency, the same experiment was repeated with an added flow rate of 17 $\mu\text{l/hr}$ for each target sequence incubation. The flow rate was determined in order to achieve Peclet numbers between 50 and 100 as discussed in section 6.2.3.2. The probe sequence was ssDNA2_T and the data for the phase change vs. applied frequency is shown in Figure 6.12. The phase data from the bode plot is used because it best demonstrates the change which occurs after incubation with the matching sequence. The noise from the Nyquist data obscures the impedance change.

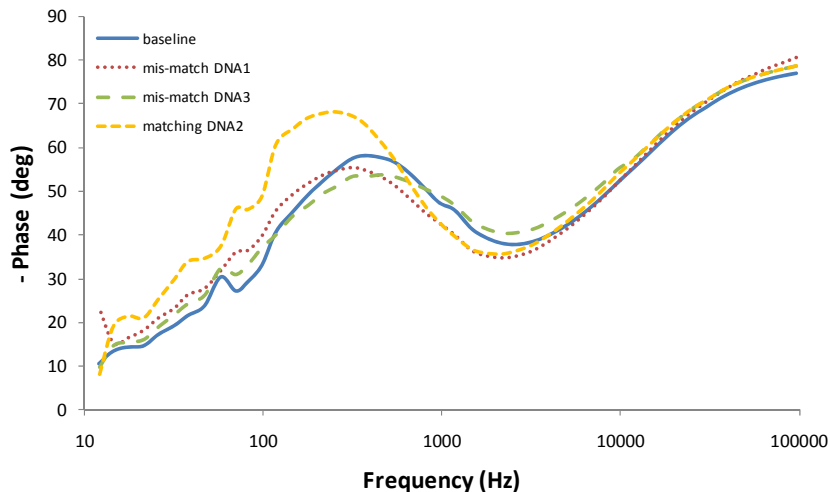


Figure 6.12: Bode plot displaying phase change vs. applied frequency after each incubation with three target DNA sequences. The matching DNA2 sequence causes a greater phase change between the frequencies of 100 - 1000 Hz indicating an increased capacitance.

A noticeable peak in the plot occurs around a frequency of 400-500 Hz. This peak in the negative phase corresponds to curvature given to the semi-circle at these lower frequencies and is related to the capacitance of the electrode-solution interface. It appears that the hybridization of the matching DNA sequence increases this capacitance which decreases the observed phase angle. The addition of further DNA molecules could be increasing the dielectric constant on the surface of the electrode which can contribute to a higher capacitance. The increase in the R_{ct} value for each incubation of mis-matching DNA1, mis-matching DNA2 and matching DNA3 was 24%, 6% and 54% respectively.

The parameters for the formation of the probe DNA and MCH monolayer were ultimately adjusted in an attempt to achieve a more stable biological layer. The concentration of the probe DNA was increased to 5 μM from 1 μM and the incubation time was increased to overnight. The MCH was allowed to incubate for 3 hours. These changes were made to allow more molecules to diffuse to the surface of the electrode in the constricted geometry of the microfluidic channels. Two different

sensors within the same channel were functionalized with ssDNA probes followed by MCH. A third sensor was also tested using a separate channel in a different device with two non-complementary sequences followed by the complementary sequence. The results after the sequential incubation with each of the target ssDNA sequences are shown in Figure 6.13.

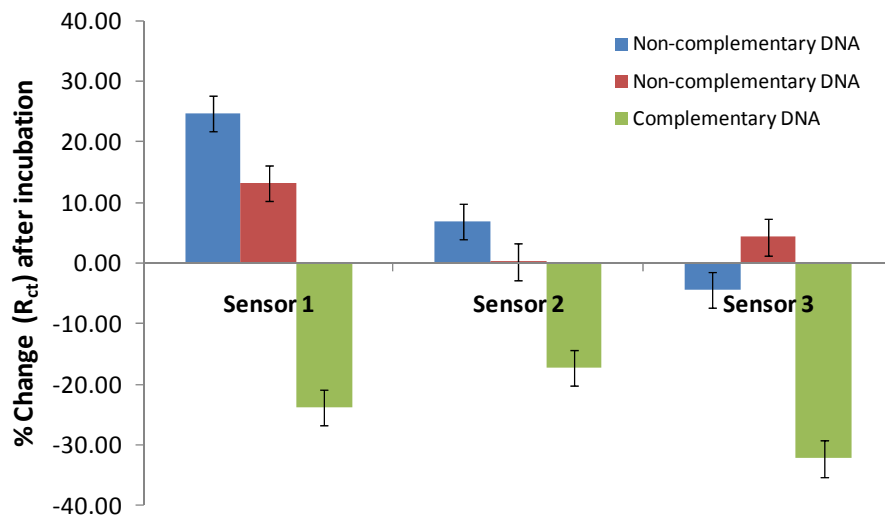


Figure 6.13: The percent change in R_{ct} for two different sensors in the same channel after incubation with 3 target ssDNA sequences. Each sensor displayed a clear decrease in R_{ct} after incubation with the matching DNA sequence.

Following incubation with each of the two non-complementary targets, the R_{ct} either increased or showed very little change for all three sensors. The increasing charge transfer resistance may be due to non-specific adsorption occurring of the DNA molecules to the counter electrode in the channel, or to adsorption on the working electrode. If adsorption is occurring on the working electrode, then that is an indication that the monolayer is not well assembled. Further evidence to support this theory is observed by the large decreases in R_{ct} for all three sensors when the matching DNA sequence is introduced. While it may seem counterintuitive that the charge transfer resistance would decrease upon hybridization, it is possible that the DNA probes are lying flat against the MCH layer before the introduction of the

matching target. Upon hybridization, the rigidity of the double helix structure causes the probes to release from the substrate and stand upright. This change in the DNA orientation can create more ion paths for the redox compound to approach the electrode surface and consequently result in a reduction of the measured impedance.

This phenomenon of decreasing impedance upon hybridization has been experienced by other research groups [25, 169, 170] and an example from Gooding et al. is shown below in Figure 6.14.

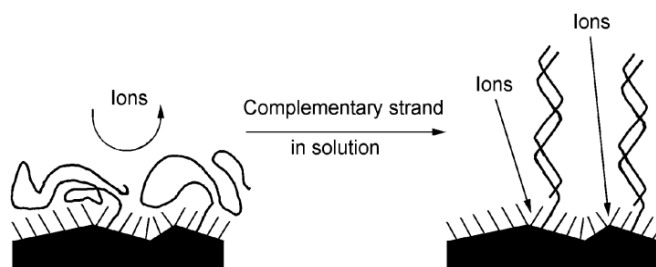


Figure 6.14: Schematic example of how DNA hybridization can cause probes to stand upright and allow more ions to interact with the electrode. Reproduced from [169].

The process described by Gooding et al. is believed to be the same situation occurring in the valved device. Providing an ordered assembly of the MCH layer is important for keeping the DNA probes from lying on the surface as previously mentioned in the chapter. In the valved device compared to the non-valved version, the assembly of the MCH layer is affected by the limited diffusion regime due to the smaller geometry of the microfluidic channels. This change in the MCH assembly has altered the detection mechanism occurring at the surface of the electrodes within the valved device.

6.6 Summary

DNA hybridization experiments were successfully performed across multiple stages of the device design. Macro-scale tests confirmed the increase in the measured

impedance for complementary target sequences while non-complementary sequences displayed very little change in the impedance. The microfluidic device was used to demonstrate the arrayed detection capability provided by the multiple patterned electrodes and rotation of the parallel channels. The device with integrated valves was also used for DNA hybridization studies, however, the smaller geometry of the channels directly affected the monolayer assembly and altered the detection mechanism of the sensor to display an impedance decrease upon hybridization. Future design changes have been planned which include etching deep pits (~70 microns) over the regions where the working electrodes are patterned in order to increase the solution volume and provide more bulk solution for the diffusion gradients to form in.

7 Conclusion

7.1 Summary

The microfluidic platform demonstrated in this dissertation is meant to showcase the possibility of using lab-on-a-chip systems for high-throughput, arrayed analysis of biological samples. Unique to this design are the detection methodology of electrochemical measurements which allow for label free sensing of affinity based binding events on the sensors' surfaces, and the multi-cross-channel design which provides simple loading of various probe molecules and samples to act as a combinatorial array. With nearly all current laboratory tools for drug screening and drug discovery requiring large, bulky equipment with long testing times and multiple laborious steps needing to be performed by highly trained personnel, lab-on-a-chip systems offer a beneficial alternative. The reduction in sample volumes, testing time, and device footprint can all lead to faster analysis at a lower cost which will dramatically improve the research being performed in the pharmaceutical field.

The microfluidic device designed in this work included an array of gold working electrodes patterned in a grid with each row containing a separate gold working electrode and platinum reference electrode. The layout is compatible with using microfluidic channels molded in PDMS to create either horizontal or vertical channels laid over the grid of sensors. One design used channels which had to be manually rotated to change the direction while a more integrated system design incorporated a second layer of PDMS valves to pinch off areas of the underlying channel and control the flow direction. Each design was successfully used for an

arrayed characterization of protein adhesion and for performing a binding affinity assay.

7.1.1 Protein Adhesion Study

The ability to screen the interactions between many proteins and surfaces using a single microfluidic device is very advantageous for designing the passivation layer to be used for a sensor surface. There has also been extensive research aimed at observing biomolecule adsorption to passivation compounds immobilized onto drug delivery systems and various other biomedical devices. Three proteins (CRP, TNF α , TNF β) were chosen to interact with three different passivation surfaces (MCH, BSA, PEG) in the device and electrochemical measurements were used to probe for adsorption. Each surface functionalization was allowed to passivate over columns of electrodes followed by rotating the channels and allowing each protein to incubate with multiple surfaces exposed in the rows.

The results demonstrated a large amount of interaction with the MCH surface and that the charge of the protein caused noticeable electrostatic effects in the measurements. BSA showed high resistance to adsorption of the proteins (with only a slight impedance increase seen with TNF α). PEG surfaces were not stable enough for accurate electrochemical measurements to be made and perhaps the study has provided some insight into problems with using PEG as a passivation material for electrochemical sensors. Impedance parameters for quantitative comparison of the adhesion were extracted from a lumped element circuit model used to fit the collected data. The ability to quickly characterize protein interactions with many different surfaces in the same device can help future researchers understand how to improve

the selectivity and non-adsorption behavior for the next generation of biosensors and biomedical devices.

7.1.2 DNA Hybridization Study

The ability to quickly screen for particular DNA sequences is very beneficial in the fields of cancer research, influenza detection and genetic engineering. Most arrayed detection methods utilize a label to produce the signal and multiple washing and incubation steps. Using the designed microfluidic devices in this work, DNA hybridization was performed with numerous sequences in the same device without the need for labels of any kind.

Probe ssDNA sequences were functionalized with a thiol group and self-assembled onto the gold working electrodes surfaces both in the microfluidic device and on the macro-scale electrodes used in a beaker. Complementary ssDNA sequences were incubated over various the various probes sequentially in the case of the macro-scale electrodes and all at once with the microfluidic device. Both CV and EIS results were used to determine any hybridization events. The results conclusively demonstrated the sensor's ability to distinguish between a complementary target sequence and a non-complementary sequence. Quantitative comparisons could be made by fitting the impedance data to a circuit model for each of the device designs. The added negative charge on the electrode due to hybridization with a complementary ssDNA sequence greatly increases the charge transfer resistance when using a negatively charged redox couple. It is my hope that providing new tools for performing DNA hybridization analysis faster and cheaper than currently used methods will lead to more efficient diagnosis of disease and genetic abnormalities,

especially in parts of the world which do not have the benefit of easy access to large laboratories with expensive high-throughput equipment.

7.2 Future Work

There are many improvements that could be made to the design of the devices which could enhance their signal-to-noise ratio and lead to better uniformity among the sensor responses. Furthermore, the device could be used for many other assay types and to perform more unique studies including single base pair mismatching with DNA and characterization of DNA breathing modes. This section provides details on these possible future endeavors with this research.

7.2.1 Microfluidic Design Improvements

As the research progressed, various channel designs were used to help reduce evaporation of the liquid as described in Chapter 2. These new designs caused more of the working electrode area to be exposed in each channel and made it more difficult to expose the exact same area for each of the nine working electrodes. One potential solution to this issue is to passivate the entire surface of the chip with an insulating material like silicon dioxide and open well defined areas over the electrodes. The deposited layer only needs to be a few hundred nanometers thick to provide adequate insulation between the solution and the underlying electrodes. A possible cross section schematic of this new design is shown in Figure 7.1.

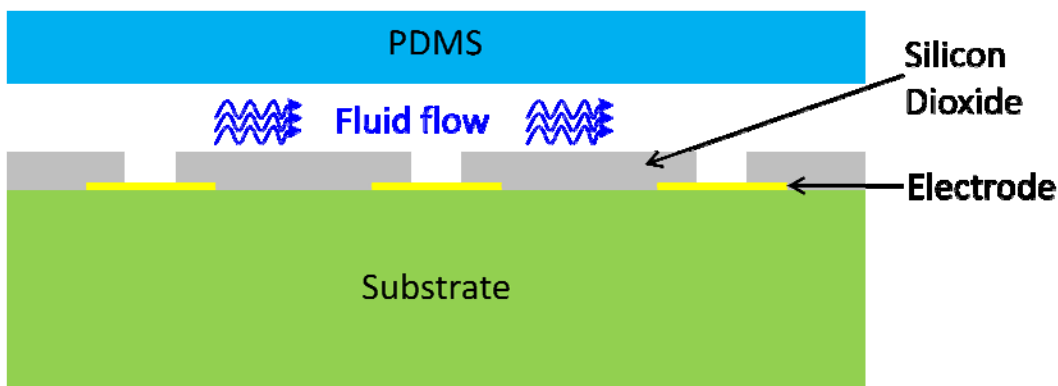


Figure 7.1: Cross section layer structure of the microfluidic device with a patterned silicon dioxide layer used to expose sensor areas. Picture is not drawn to scale.

Openings would be patterned in the silicon dioxide layer over each of the electrodes in the system and for the contact pads on the edge of the chip. This allows for precise control over the exposed areas for each of the sensors. However, it must be noted that using such a layer design will affect the diffusion profile of the biomolecules and the redox compound over the electrodes. This will alter the shape of collected CV plots and could also affect the impedance data at low frequencies. A more detailed explanation of how these recessed electrodes will affect the diffusion properties can be found in [171].

By patterning numerous small (~ 10 μm diameter) openings in a cluster over the working electrode, an ultra-microelectrode array can be formed. Such arrays have been used extensively by other groups in order to increase the sensitivity of the measurement while keeping the current amplitude high, thus improving the SNR of the system [127, 172]. A local diffusion gradient existing over each electrode opening contributes to the high sensitivity while the high overall exposed area between all the openings contributes to a greater measured current. These patterned arrays could be very beneficial for future studies with the device to further decrease the limit of detection for samples with a very low target concentration.

Another added advantage to using a patterned passivation layer is that new electrode lead designs can be explored. One example is to connect the columns of working electrodes in a parallel configuration as opposed to the current series configuration. If a high current is accidentally passed through one of the working electrodes, it can cause anodization and possible damage to the surface. With the configuration in series, this damage could affect measurements taken from electrodes further down the column, but if a parallel configuration is used, any damage to one electrode will not affect the others.

It became increasingly clear while performing DNA hybridization experiments using the valved microfluidic device that the smaller cross-section geometry of the microfluidic channels directly affected the assembly of the monolayers and caused the detection mechanism to completely change upon DNA hybridization. When larger microfluidic channels with a height of 100 microns were used, these issues were not present. However, in the valved device design, the channel height cannot be made much larger than 35 microns in order to achieve efficient valve sealing. One possible solution is to provide deeper “wells” only in the regions where the working electrodes are patterned in order to increase the diffusion distance above the electrode. This requires a selective etching process in these areas.

An Oxford PlasmaLab system was used to provide an inductively coupled plasma (ICP) etch of the glass substrate. The recipe used 24 sccm C₄F₈ and 56 sccm He at an ICP power of 1400 W and an RIE power of 85 W. The substrate was also heated to 50 °C during the process. A 20 minute etch using a patterned mask of

AZ9260 was performed. A contact profilometer was used to provide a depth measurement and the result is shown in Figure 7.2.

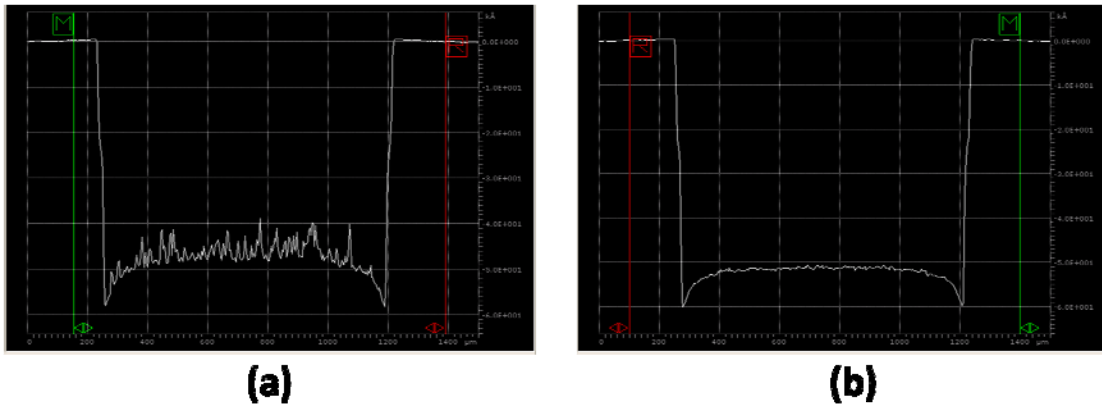


Figure 7.2: Depth profiles along a pit patterned in glass directly after the ICP etch (a) and after dipping the wafer into HF for 15 seconds (b). The depth is around 5 microns with deeper notches observed around the inner edge.

Figure 7.2a displays the profile directly after the etch has been performed. There is significant roughness along the bottom of the well and an etch depth of 5 microns is observed giving an etch rate of about 250 nm/min. In order to reduce the roughness, the wafer was dipped into a concentrated hydrofluoric acid (HF) for 15 seconds which quickly and isotropically etches away glass. The resulting profile in Figure 7.2b after the HF dip displays much lower roughness and would be better suited for patterning electrodes. Further characterization of the process would still need to be performed to achieve deeper wells and to eliminate the deeper notches around the inner edge.

A series of experiments could be performed using the microfluidic device before and after the valve integration both with and without the added etched pits. However, the electrode area exposed to the solution should be kept constant for each test in order to compare only the effects of diffusion on the collected data. The silicon

dioxide passivation procedure mentioned earlier in this chapter could be used with these tests to precisely control the exposed electrode area.

7.2.2 Use of Chitosan

Chitosan is a unique amino-polysaccharide material that can be patterned on sensor surfaces to confer functionality. This can be achieved either through probe compounds covalently bound to the amine groups of the chitosan or through proteins co-immobilized within the chitosan during deposition. Chitosan has been used extensively at the University of Maryland for a variety of sensing applications in both microfluidic devices and for macro-scale study [76, 82, 173-175].

One of the great advantages of chitosan is its ability to be patterned through electrodeposition. By applying a small potential between an anode and cathode in a chitosan solution, the pH gradient formed at the cathode causes deprotonation of the chitosan amine groups and the chitosan becomes insoluble. Consequently, a solid, stable film forms over the cathode. This gives the patternability of chitosan both temporal and spatial control while self assembled monolayers like those used in this research only have spatial control.

Chitosan also contains a dense population of exposed amine groups which can be covalently bonded to numerous types of biomolecules. In fact, our own lab has performed DNA hybridization studies using chitosan to immobilize the probe ssDNA [46, 82].

The microfluidic devices already contain an array of patterned electrodes to be used for the chitosan electrodeposition. Chitosan could be deposited on each of the nine sensors with a different enzyme co-immobilized over each sensor. In this way,

multiple fluid paths can be formed with each one containing a different biosynthetic pathway comprised of sequential enzymatic conversion steps. A prime example of such a pathway includes the enzymes involved in the production of the bacterial signaling molecule AI-2 in *E. coli* as shown below in Figure 7.3.

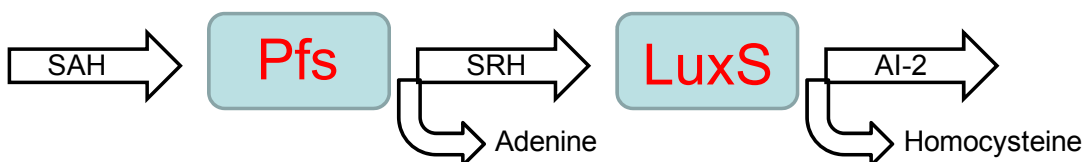


Figure 7.3: Biosynthetic pathway for the production of AI-2 converted from the substrate SAH via the enzymes Pfs and LuxS.

In this example, two enzymes found within *E. coli* convert the substrate SAH into AI-2, the concentration of which facilitates quorum sensing behavior amongst the bacteria leading to pathogenic biofilm formation. Studies by our group and collaborators as part of the Biochip collaborative are aimed at producing microsystems and biochemical technology to help understand this pathway and developing drugs to inhibit biofilm formation.

Each enzyme could be immobilized within the device using the chitosan electrodeposition while impedance measurements can be made to probe the activity of each enzyme and for the production of any specific targets downstream. The advantage of the device is the ability to screen more than just one channel containing each of these enzymes, and possibly even to screen other types of biosynthetic pathways in the neighboring channels.

7.2.3 Other Assays and Studies

This research demonstrated a protein adhesion study and a DNA hybridization study, but many other affinity based binding studies can be performed. These include DNA-protein binding assays, aptamer-protein binding assays, and immunoassays.

Furthermore, unique phenomena of DNA binding including single-base pair mismatching and DNA breathing modes may be explored as well.

Gene expression or repression can be controlled via proteins bound to specific DNA sequences, and the ability to screen for these interactions in-vitro has far reaching pharmaceutical implications. Very few research groups have successfully used electrochemical measurements to detect protein binding to immobilized dsDNA [176, 177], but the field is still young and the platforms described in this work could ultimately be used for this purpose. One difficult hurdle to overcome is any hindrance the protein may have to accessing the binding site of the DNA if it is immobilized to an electrode.

The majority of electrochemical measurements for detecting specific proteins use aptamers as probe compounds. Aptamers are ssDNA sequences that are coded specifically to bind to a certain protein. They are extremely sensitive and can be self assembled onto electrodes using a thiol group just like the ssDNA used in this research. The main drawback of aptamers is that they do not exist for all proteins that may be of interest in studying. Nevertheless, if the correct aptamers do exist, their inclusion could be an excellent way to use the microfluidic devices for protein screening.

Immunoassays involving an antibody-antigen reaction are performed constantly using conventional laboratory equipment and fluorescent labels. However, it has been demonstrated that these assays could also be performed using electrochemical measurements [99, 130, 178]. Immobilizing antibodies over various

sensors in the device either through the use of chitosan or another protein such as biotin would allow for a label-free immunoassay array to be performed.

The ability to detect small DNA mutations (as small as a single base pair defect) along the length of the sequence could greatly benefit genetic research. The work demonstrated with the microfluidic devices in this research was able to determine whether or not complete hybridization occurred, but it would not be sensitive enough in its current state to detect such small mutations in the ssDNA target sequence. To perform more advanced hybridization studies, the probe ssDNA strand can be intercalated with a redox label so that charge transport occurs through the double helix of the DNA. Any mismatches along the length of the helix will cause a change in the transport properties.

A similar phenomenon to single base pair mutations in DNA hybridization is the concept of breathing modes. DNA “breathing” refers to a temporary opening between matching base pairs which can close and re-open again typically on a time scale of nearly 1 second [179]. Researchers believe that these breathing dynamics are crucial for biological functioning during transcription and interaction with proteins [180]. The microfluidic devices in this research could be utilized for detecting breathing events by using the same method described for single base pair mutations; by attaching a redox label to the DNA duplex and measuring charge transport properties through the helix. The unzipping of base pairs along the duplex will alter the transport properties and should be well observed due to the large time scale of breathing events compared to the rate of charge transfer.

7.3 Conclusion

The ever evolving field of clinical diagnostics and drug screening will always have a need for faster, cheaper, and more sensitive tools. It is believed that the research performed in this dissertation will help add to the knowledge base for developing such tools. By demonstrating operation with both proteins and DNA, the devices' capabilities for performing many different assays and biological studies are presented. Furthermore, the effects that the microchannel dimensions have on the measurement and assembly mechanism have been explored to highlight a few of the challenges involved with designing a more complex system. These devices may be a small part of an eventual movement towards widespread use of electrochemical arrays for diagnostic research.

Appendix A

This Appendix contains the MATLAB source code that used to performed CV simulations which are found in Chapter 2.

```
% Electrochemical response simulator
% Definition of variables
a = .5; % reaction transfer coefficient assumed to be same for both
ox and red
kchem = 0; % homogenous reaction rate for chemical reaction (none
for my case)
E = 0.245; % Formal reduction potential (for Ferrocene Dimethanol,
its about 0.25)
khet = 0.5; % heterogenous rate constant, must be found through
testing
R = 8.3145; % Universal gas constant
n = 1; % number of electrons exchanged per reaction
F = 96485.34; % Faraday's constant
D = 1 * 10^-5; % Diffusion coefficient
ipot = 0.7; % Starting potential for the scan
fpot = 0.7; % Final scan potential
spot = -0.3; % Switching potential
nt = 200; % discrete number of time steps for simulation to run
area = .03141; % area of 1 millimeter radius electrode
temp = 298; % Room temperature in K
scanr = 0.1; % Scan rate in V/s
T = 2*abs(spot - ipot)/scanr; % Computes total time of the
experiment
delt = T/nt; % each time increment is computed
X = 2 * sqrt(D*T); % Total diffusion layer thickness above electrode
delx = sqrt(D*delt/0.5); % small spatial increment values
ns = round(X/delx); % discrete number of spatial increments above
electrode

% Initialize my matrices and arrays
C = zeros(3,ns+1);
Ctemp = zeros(3,ns+1);
potforward = ipot:(2*(spot-ipot)/nt):spot;
potreverse = (spot+(2*(fpot-spot)/nt)):(2*(fpot-spot)/nt):(fpot-
(2*(fpot-spot)/nt));
pot = [potforward potreverse];
current = zeros(3,nt);
J = [0 0 0];

for count = 1:1:3

    % Create initial concentration profile above electrode surface
    for i = 1:1:(ns+1)
        C(1,i) = 1.0; %contains current oxidation concentration
        C(2,i) = 0.0; %contains current reduction concentration
        C(3,i) = 0.0; %reference

        Ctemp(1,i) = 1.0;
```

```

        Ctemp(2,i) = 0.0;
        Ctemp(3,i) = 0.0;
    end

    % Start main program loop

    for i = 1:1:nt
        for y = 1:1:3
            for z = 1:1:ns
                C(y,z) = Ctemp(y,z);
            end
        end

        % Calculate current from Butler-Volmer equation based on
        % Surface concentration
        kf = khet * exp(-a*n*F*(pot(i)-E)/(R*temp));
        kr = khet * exp(a*n*F*(pot(i)-E)/(R*temp));

        J(1) = (kf*C(1,1) - kr*C(2,1))/(1+kf/0.9+kr/0.9);
        J(2) = -J(1);
        J(3) = 0.0;

        current(count,i) = J(1)*((sqrt(D*delt/0.5))/delt)*96484*10^-
        6*area;

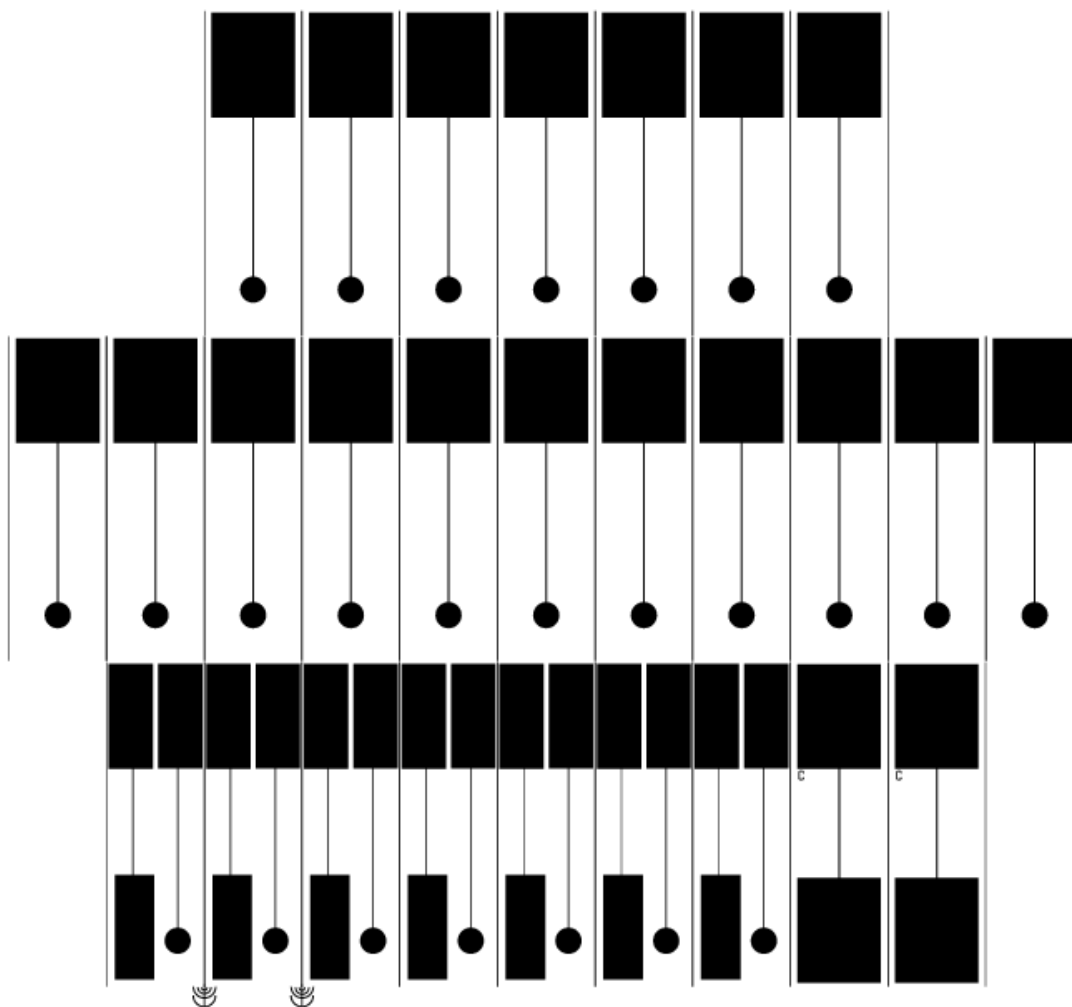
        % Calculate concentration change due to diffusion
        for y = 1:1:3
            Ctemp(y,1) = C(y,1) + ((delt*D/delx^2)*(C(y,2) -
            C(y,1))) - J(y);
            for z = 2:1:ns
                Ctemp(y,z) = C(y,z) + ((delt*D/delx^2)*(C(y,z-1)-
                2*C(y,z)+ C(y,z+1)));
            end
        end
    end
    khet = khet/10;
    D = D/1.5;
end
% Output vectors for potential and current
plot(pot,current)

```

Appendix B

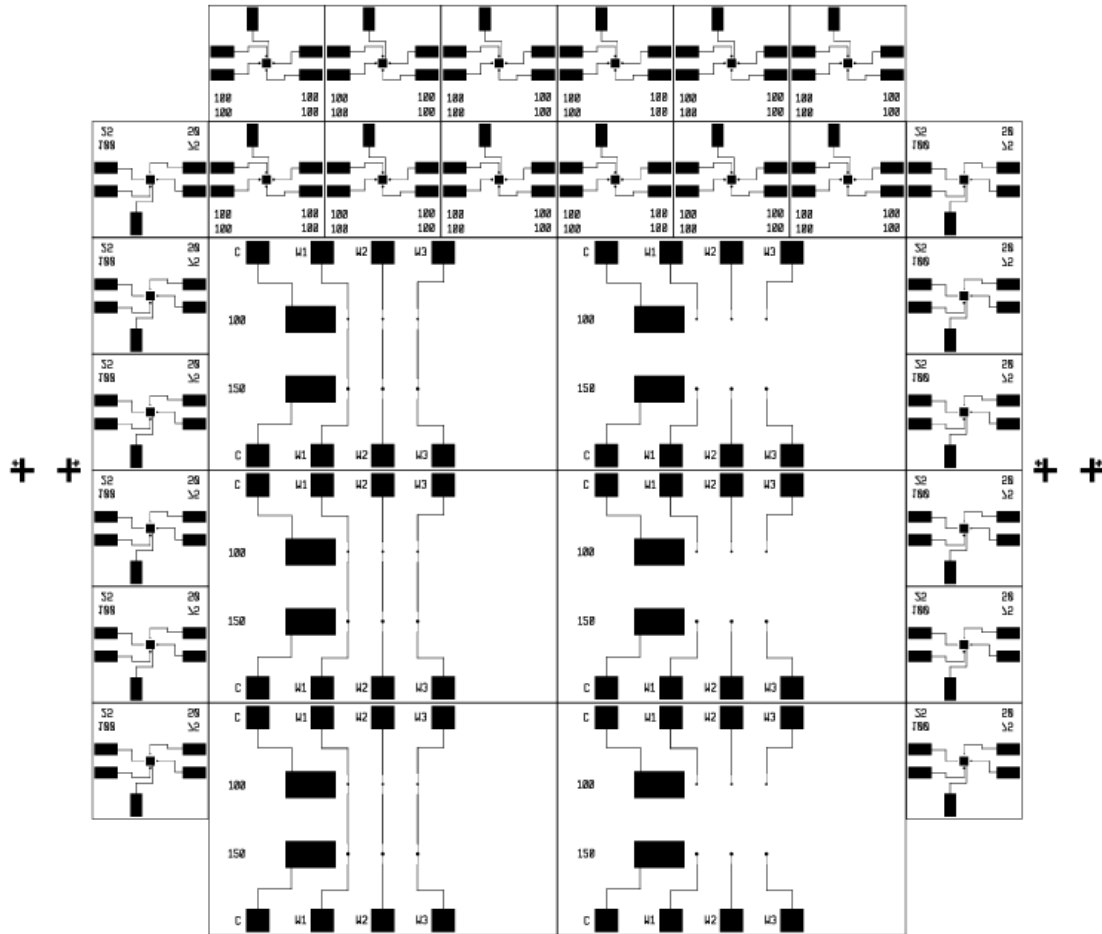
Mask #1

Pattern used for macroscale chips consisting of working and counter electrodes



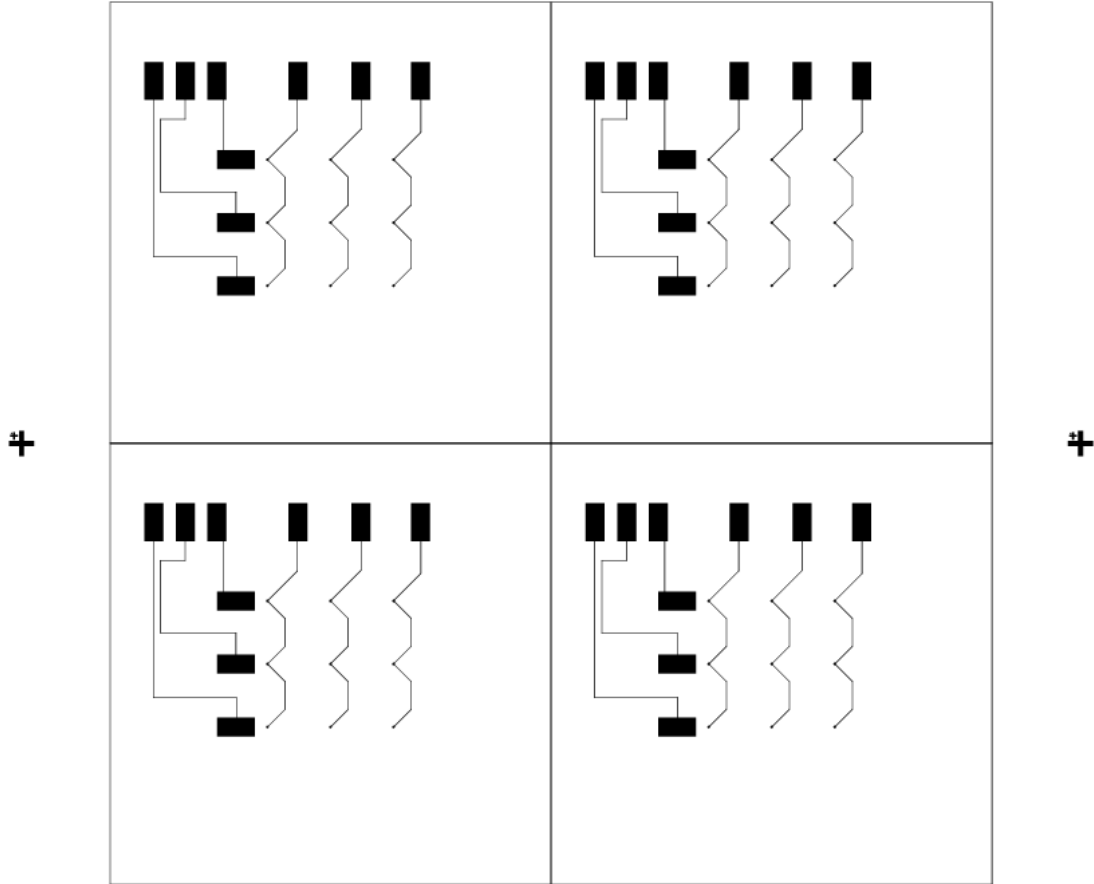
Mask #2

Gold pattern on 1 cm x 1 cm chips used for droplet testing. The mask also has larger patterned chips which were not used.



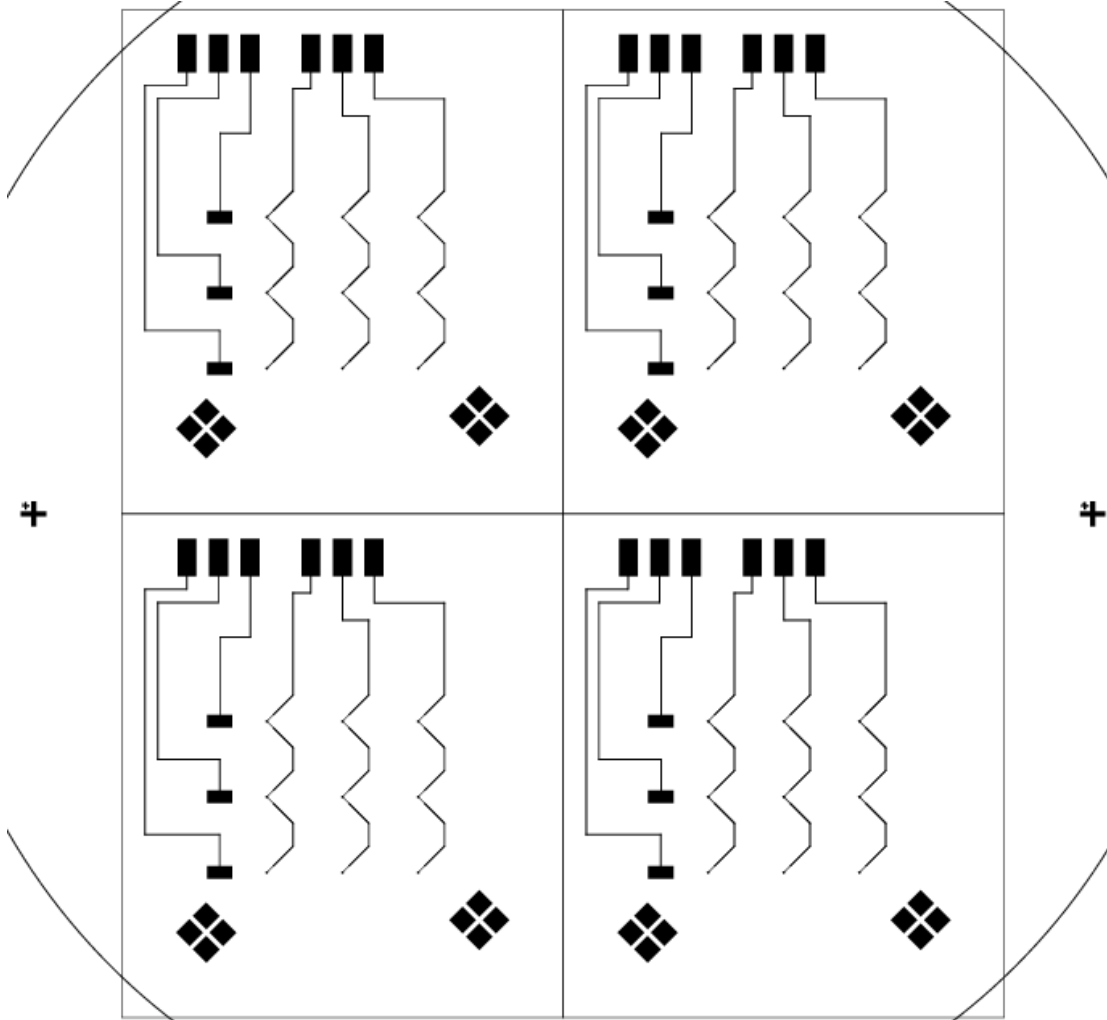
Mask #3

Gold pattern used for the non-valved microfluidic design.



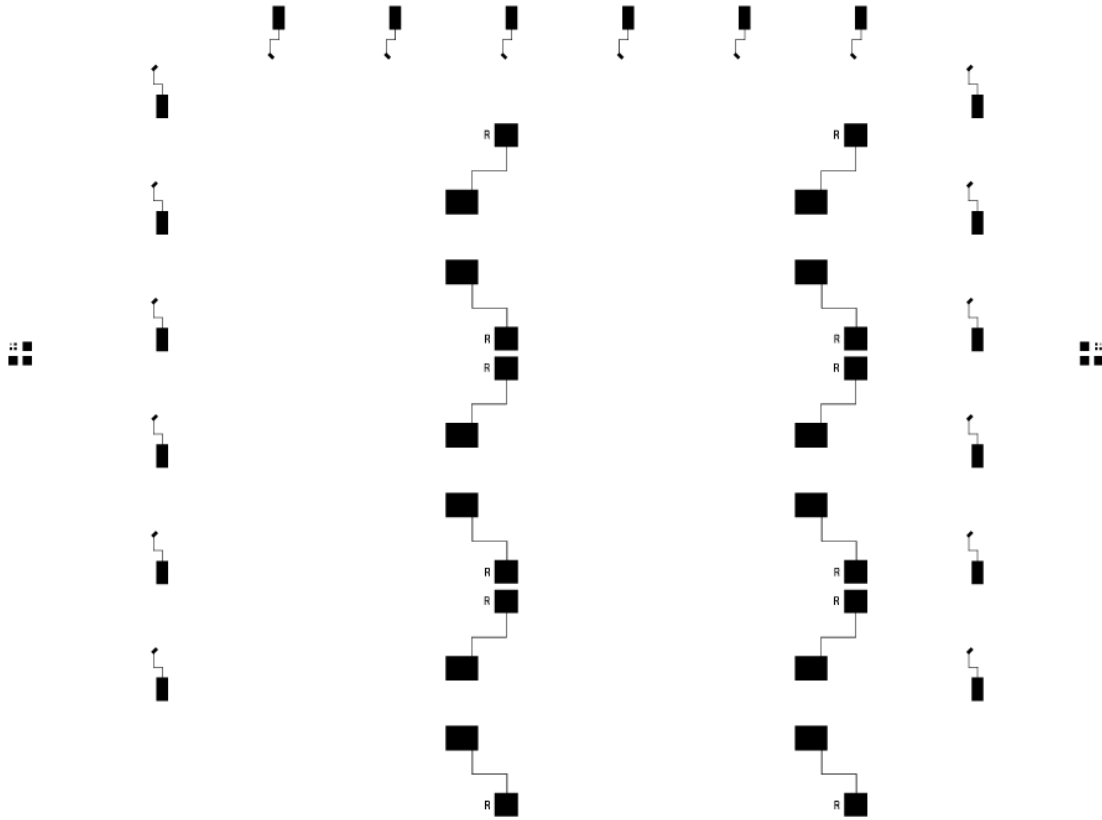
Mask #4

Gold pattern used for the valved microfluidic design



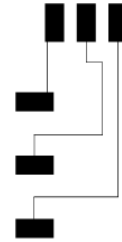
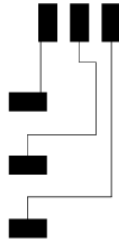
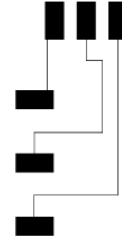
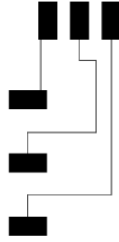
Mask #5

Platinum pattern on 1 cm x 1 cm chips used for droplet testing



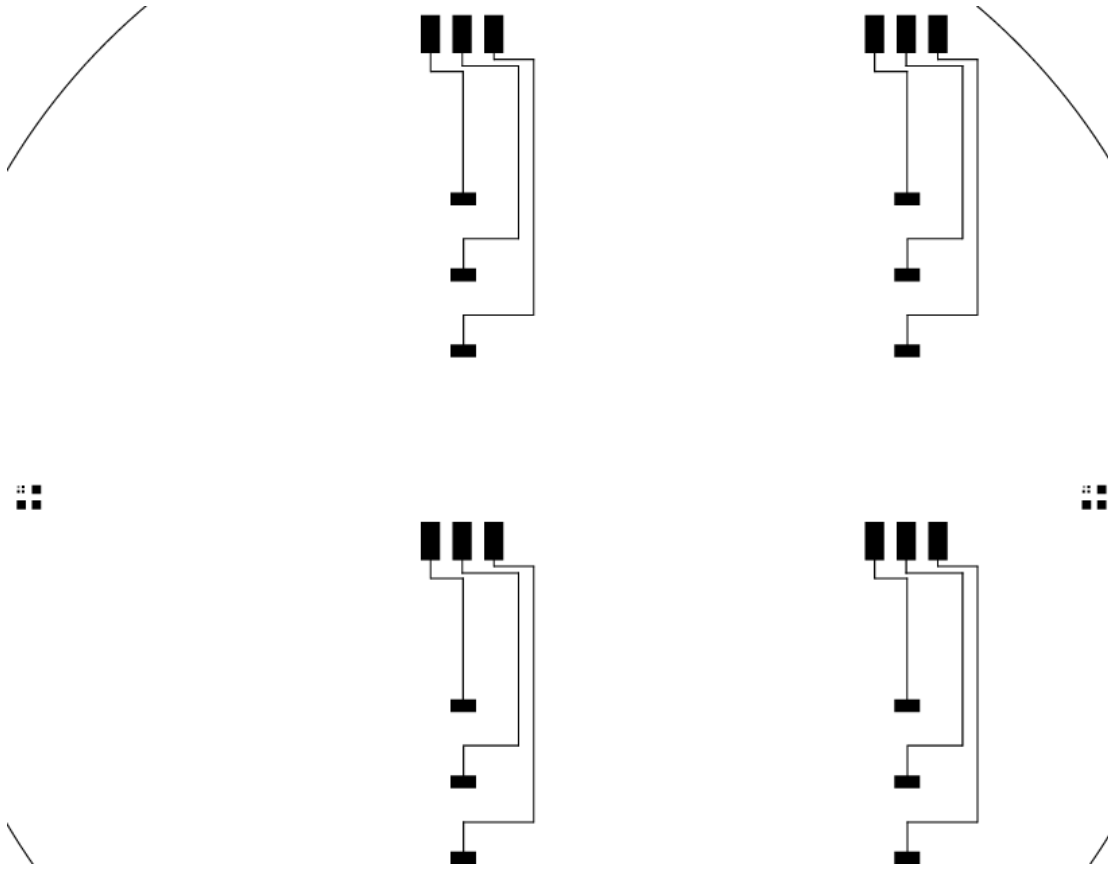
Mask #6

Platinum pattern used for the non-valved microfluidic design



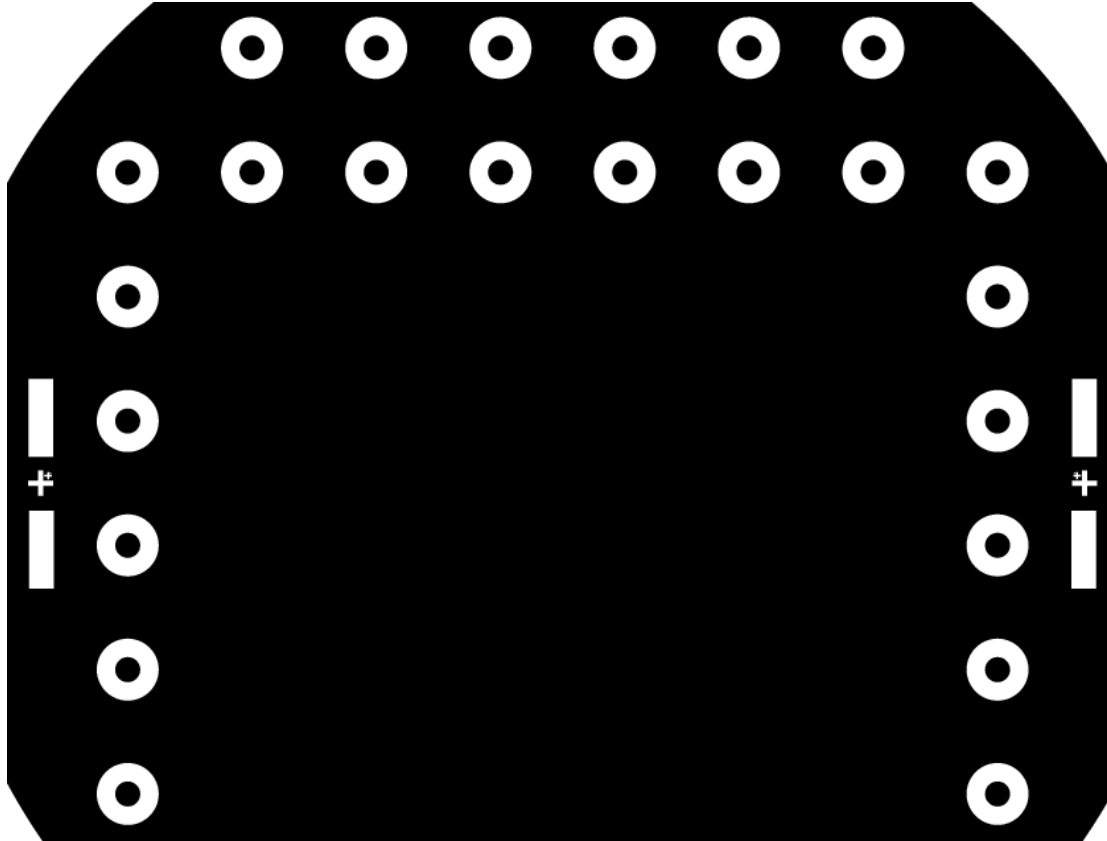
Mask #7

Platinum pattern used for the valved microfluidic design



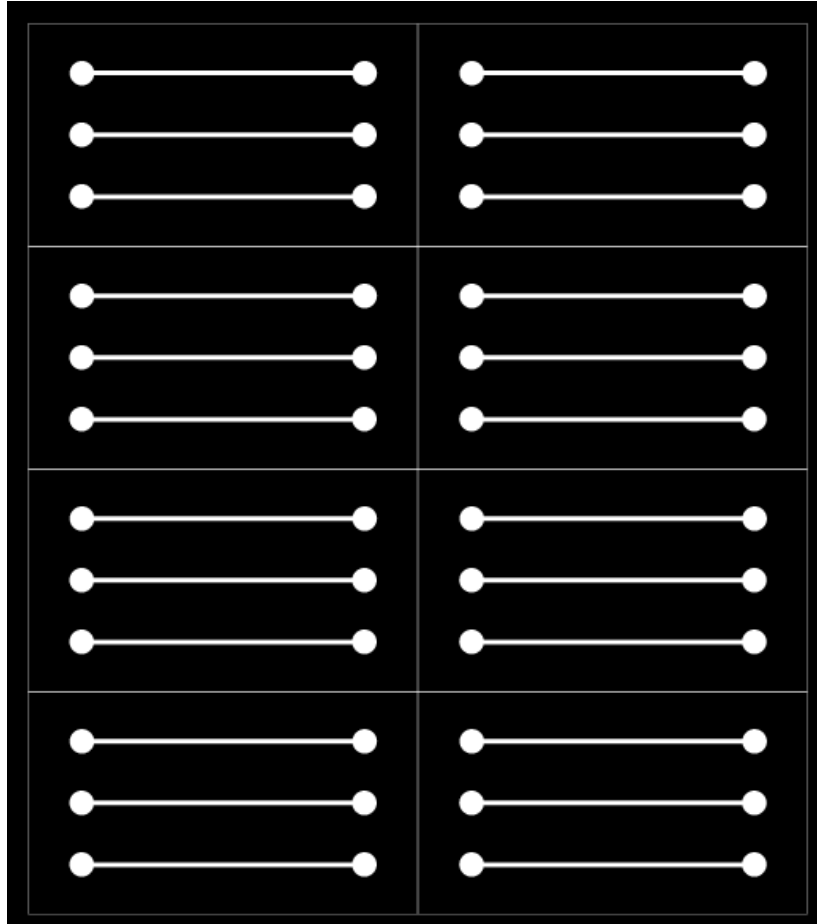
Mask #8

SU-8 5 pattern on the 1 cm x 1 cm chips used for droplet testing



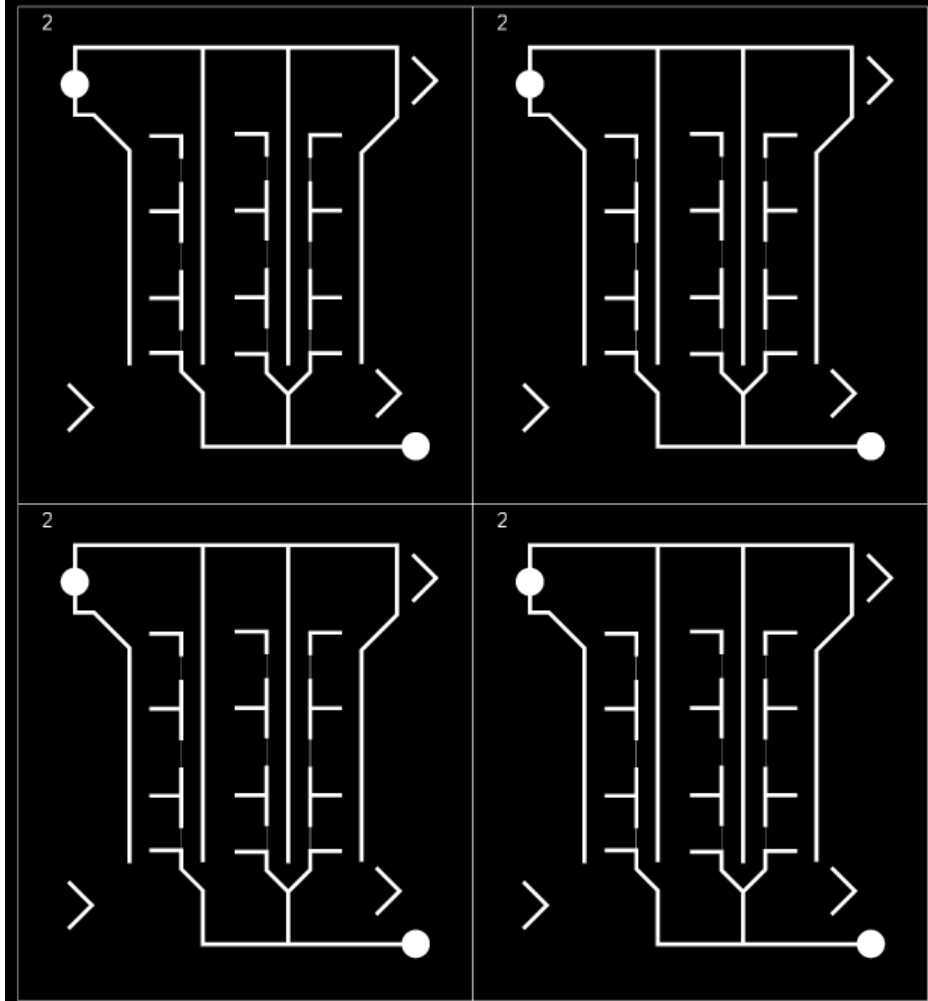
Mask #9

Mold for creating straight microfluidic channels to be used with the non-valve design



Mask #10

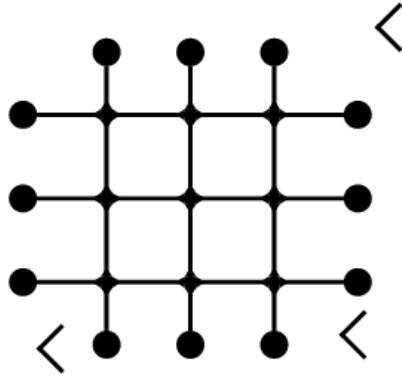
Mold for creating valve channels to be used with the valved chip design



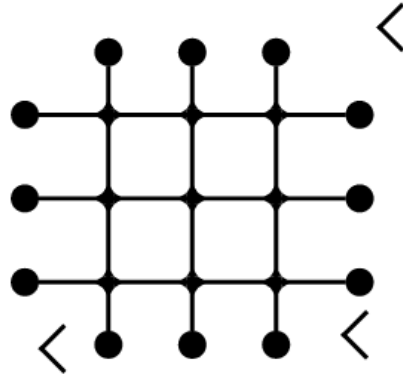
Mask #11

Mold used for the microfluidic channels in the valved design

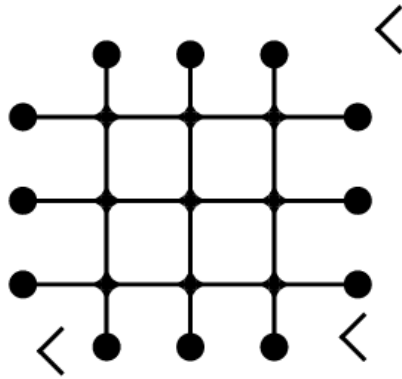
1



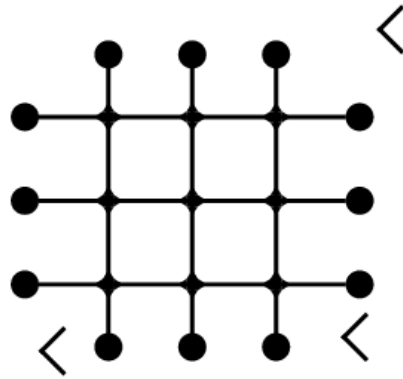
1



1



1



References

- [1] J. A. DiMasi, R. W. Hansen, and H. G. Grabowski, "The price of innovation: new estimates of drug development costs," *Journal of Health Economics*, vol. 22, pp. 151-185, 2003.
- [2] H. K. Bleicher, H.-J. Böhm, K. Müller, and A. I. Alanine, "Hit and Lead Generation: Beyond High-Throughput Screening," *Nature Reviews Drug Discovery*, vol. 2, pp. 369-378, 2003.
- [3] J. Drews, "Drug Discovery: A Historical Perspective," *Science*, vol. 287, pp. 1960-1964, 2000.
- [4] A. J. Bard and L. R. Faulkner, *Electrochemical methods: Fundamentals and applications*, 2nd ed. New York: John Wiley & Sons Inc., 2001.
- [5] C. D. Chin, V. Linder, and S. K. Sia, "Lab-on-a-chip devices for global health: Past studies and future opportunities," *Lab Chip*, vol. 7, pp. 41-57, 2007.
- [6] D. Figeys and D. Pinto, "Lab-on-a-Chip: A Revolution in Biological and Medical Sciences," *Anal. Chem.*, vol. 72, pp. 330A-335A, 2000.
- [7] E. A. M. Graham, "Lab-on-a-chip technology," *Forensic Science, Medicine, and Pathology*, vol. 1, pp. 221-223, 2005.
- [8] S. Haerberle and R. Zengerle, "Microfluidic platforms for lab-on-a-chip applications," *Lab Chip*, vol. 7, pp. 1094-1110, 2007.
- [9] B. H. Weigl, R. L. Bardell, and C. R. Cabrera, "Lab-on-a-chip for drug development," *Advanced Drug Delivery Reviews*, vol. 55, pp. 349-377, 2003.
- [10] J. Hong, J. B. Edel, and A. J. deMello, "Micro- and nanofluidic systems for high-throughput biological screening," *Drug Discovery Today*, vol. 14, pp. 134-146, 2009.
- [11] Y. Sun and Y. C. Kwok, "Polymeric microfluidic system for DNA analysis," *Anal. Chim. Acta*, vol. 556, pp. 80-96, 2006.
- [12] Y. Xu, X. Yang, and E. Wang, "Review: Aptamers in microfluidic chips," *Anal. Chim. Acta*, vol. 683, pp. 12-20, 2010.
- [13] W. Yang and A. T. Woolley, "Integrated Multiprocess Microfluidic Systems for Automating Analysis," *Journal of Laboratory Automation*, vol. 15, pp. 198-209, 2010.
- [14] T. Gervais and K. F. Jensen, "Mass transport and surface reactions in microfluidic systems," *Chemical Engineering Science*, vol. 61, pp. 1102-1121, 2006.
- [15] H. Song and R. F. Ismagilov, "Millisecond Kinetics on a Microfluidic Chip Using Nanoliters of Reagents," *J. Am. Chem. Soc.*, vol. 125, pp. 14613-14619, 2003.
- [16] K. K. Jefferson, "What drives bacteria to produce a biofilm?" *FEMS Microbiology Letters*, vol. 236, pp. 163-173, 2004.
- [17] K. Lewis, "Riddle of biofilm resistance," *Antimicrob. Agents Chemother.*, vol. 45, pp. 999-1007, 2001.
- [18] X. G. Han and C. P. Lu, "In vitro biosynthesis of autoinducer 2 of *Streptococcus suis* Serotype 2 using recombinant LuxS and Pfs," *Enzyme and Microbial Technology*, vol. 44, pp. 40-45, 2009.

- [19] M. Li, A. E. Villaruz, V. Vadyvaloo, D. E. Sturdevant, and M. Otto, "AI-2-dependent gene regulation in *Staphylococcus epidermidis*," *BMC Microbiology*, vol. 8, 2008.
- [20] V. Singh, et al., "Structure and inhibition of a quorum sensing target from *Streptococcus pneumoniae*," *Biochemistry*, vol. 45, pp. 12929-12941, 2006.
- [21] A. Vendeville, K. Winzer, K. Heurlier, C. M. Tang, and K. R. Hardie, "Making 'sense' of metabolism: Autoinducer-2, LuxS and pathogenic bacteria," *Nature Reviews*, vol. 3, pp. 383-396, 2005.
- [22] F. Caruso, E. Rodda, D. N. Furlong, and V. Haring, "DNA binding and hybridization on gold and derivatized surfaces," *Sensor. Actuat. B-Chem.*, vol. 41, pp. 189-197, 1997.
- [23] M. Chee, et al., "Accessing Genetic Information with High-Density DNA Arrays," *Science*, vol. 25, pp. 610-614, 1996.
- [24] K.-S. Ma, H. Zhou, J. Zoval, and M. Madou, "DNA hybridization detection by label free versus impedance amplifying label with impedance spectroscopy," *Sensor. Actuat. B-Chem.*, vol. 114, pp. 58-64, 2006.
- [25] T. Ito, K. Hosokawa, and M. Maeda, "Detection of single-base mismatch at distal end of DNA duplex by electrochemical impedance spectroscopy," *Biosens. Bioelectron.*, vol. 22, pp. 1816-1819, 2007.
- [26] A. Kallioniemi, et al., "Detection and mapping of amplified DNA sequences in breast cancer by comparative genomic hybridization," *Proc. Natl. Acad. Sci.*, vol. 91, pp. 2156-2160, 1994.
- [27] A. M. Wang, et al., "Molecular cloning of the complementary DNA for human tumor necrosis factor," *Science*, vol. 228, pp. 149-154, 1985.
- [28] L. T.-H. Kao, L. Shankara, T. G. Kanga, G. Zhanga, G. K. I. Taya, S. R. M. Rafeia, and C. W. H. Lee, "Multiplexed detection and differentiation of the DNA strains for influenza A (H1N1 2009) using a silicon-based microfluidic system," *Biosens. Bioelectron.*, vol. 26, pp. 2006-2011, 2011.
- [29] A. Kukol, P. Li, P. Estrela, P. Ko-Ferrigno, and P. Migliorato, "Label-free electrical detection of DNA hybridization for the example of influenza virus gene sequences," *Analytical Biochemistry*, vol. 374, pp. 143-153, 2008.
- [30] E. Pavlovic, R. Y. Lai, T. T. Wu, B. S. Ferguson, R. Sun, K. W. Plaxico, and H. T. Soh, "Microfluidic device architecture for electrochemical patterning and detection of multiple DNA sequences," *Langmuir*, vol. 24, pp. 1102-1107, 2008.
- [31] J. Li, S. Chen, and D. H. Evans, "Typing and subtyping influenza virus using DNA microarrays and multiplex reverse transcriptase PCR," *J. Clin. Microbiol.*, vol. 39, pp. 696-704, 2001.
- [32] J. G. Harman, "Allosteric regulation of the cAMP receptor protein," *Biochim. Biophys. Acta*, vol. 1547, pp. 1-17, 2001.
- [33] A. Kolb, S. Busby, H. Buc, S. Garges, and S. Adhya, "Transcriptional Regulation by cAMP and its Receptor Protein," *Annu. Rev. Biochem.*, vol. 62, pp. 749-795, 1993.
- [34] C. L. Lawson, D. Swigon, K. S. Murakami, S. A. Darst, H. M. Berman, and R. H. Ebright, "Catabolite activator protein: DNA binding and transcription activation," *Curr. Opin. Struc. Biol.*, vol. 14, pp. 1-11, 2004.

- [35] E. Kamali-Sarvestani, A. Merat, and A.-R. Talei, "Polymorphism in the genes of alpha and beta tumor necrosis factors (TNF-a and TNF-b) and gamma interferon (IFN-g) among Iranian women with breast cancer," *Cancer Lett.*, vol. 223, pp. 113-119, 2005.
- [36] R. Polsky, J. C. Harper, D. R. Wheeler, S. M. Dirk, D. C. Arango, and S. M. Brozik, "Electrically addressable diazonium-functionalized antibodies for multianalyte electrochemical sensor applications," *Biosens. Bioelectron.*, vol. 23, pp. 757-764, 2008.
- [37] Z. Yin, Y. Liu, L.-P. Jiang, and J.-J. Zhu, "Electrochemical immunosensor of tumor necrosis factor based on alkaline phosphatase functionalized nanospheres," *Biosens. Bioelectron.*, vol. 26, pp. 1890-1894, 2011.
- [38] T. G. Drummond, M. G. Hill, and J. K. Barton, "Electrochemical DNA sensors," *Nat. Biotechnol.*, vol. 21, pp. 1192-1199, 2003.
- [39] W. Yao, L. Wang, H. Wang, X. Zhang, and L. Li, "An aptamer-based electrochemiluminescent biosensor for ATP detection," *Biosens. Bioelectron.*, vol. 24, pp. 3269-3274, 2009.
- [40] S. Ichiyama, Y. Inuma, Y. Tawada, S. Yamori, Y. Hasegawa, K. Shimokata, and N. Nakashima, "Evaluation of Gen-Probe Amplified Mycobacterium Tuberculosis Direct Test and Roche PCR-Microwell Plate Hybridization Method (AMPLICOR MYCOBACTERIUM) for Direct Detection of Mycobacteria," *Journal of Clinical Microbiology*, vol. 34, pp. 130-133, 1996.
- [41] H. H. Kessler, et al., "Rapid Detection of Mycoplasma pneumoniae by an Assay Based on PCR and Probe Hybridization in a Nonradioactive Microwell Plate Format," *Journal of Clinical Microbiology*, vol. 35, pp. 1592-1594, 1997.
- [42] S. K. Sia, V. Linder, B. A. Parviz, A. Siegel, and G. M. Whitesides, "An Integrated Approach to a Portable and Low-Cost Immunoassay for Resource-Poor Settings," *Angew. Chem. Int. Ed.*, vol. 43, pp. 498-502, 2004.
- [43] N. T. K. Thanh and Z. Rosenzweig, "Development of an Aggregation-Based Immunoassay for Anti-Protein A Using Gold Nanoparticles," *Anal. Chem.*, vol. 74, pp. 1624-1628, 2002.
- [44] S.-N. Cho, et al., "Colorimetric Microwell Plate Hybridization Assay for Detection of Amplified Mycobacterium tuberculosis DNA from Sputum Samples," *Journal of Clinical Microbiology*, vol. 33, pp. 752-754, 1995.
- [45] C.-Y. Lee, G. Panicker, and A. K. Bej, "Detection of pathogenic bacteria in shellfish using multiplex PCR followed by CovaLink NH microwell plate sandwich hybridization," *Journal of Microbiological Methods*, vol. 53, pp. 199-209, 2003.
- [46] M. Powers, "Design, Fabrication and Testing of a Chitosan Based Optical Biosensor," Master's Thesis, University of Maryland, College Park, MD, July 2006.
- [47] E. Engvall and P. Perlman, "Enzyme-linked immunosorbent assay (ELISA). Quantitative assay of immunoglobulin G," *Immunochemistry*, vol. 8, pp. 871-874, 1971.
- [48] R. Lequin, "Enzyme immunoassay (EIA)/enzyme-linked immunosorbent assay (ELISA)," *Clin. Chem.*, vol. 51, pp. 2415-2418, 2005.

- [49] B. Zhang, F. Foret, and B. L. Karger, "High-Throughput Microfabricated CE/ESI-MS: Automated Sampling from a Microwell Plate," *Anal. Chem.*, vol. 73, pp. 2675-2681, 2001.
- [50] Y. Sakai, Y. Yoshiura, and K. Nakazawa, "Embryoid body culture of mouse embryonic stem cells using microwell and micropatterned chips," *Journal of Bioscience and Bioengineering*, vol. 111, pp. 85-91, 2011.
- [51] P. Mitchell, "A perspective on protein microarrays," *Nat. Biotechnol.*, vol. 20, pp. 225-229, 2002.
- [52] N. C. Andrews and D. V. Faller, "A rapid micropreparation technique for extraction of DNA-binding proteins from limiting numbers of mammalian cells," *Nucleic Acids Res.*, vol. 19, pp. 2499, 1991.
- [53] K. Ruscher, M. Reuter, D. Kupper, G. Trendelenburg, U. Dirnagl, and A. Meisel, "A fluorescence based non-radioactive electrophoretic mobility shift assay," *Journal of Biotechnology*, vol. 78, pp. 163-170, 2000.
- [54] D. F. Senear and M. Brenowitz, "Determination of Binding Constants for Cooperative Site-specific Protein-DNA Interactions Using the Gel Mobility-shift Assay," *The Journal of Biological Chemistry*, vol. 266, pp. 13661-13671, 1991.
- [55] R. E. Dodson, K. M. Goolsby, M. Acena-Nagel, C. Mao, and D. J. Shapiro, "RNA Gel Shift Assays for Analysis of Hormone Control of mRNA Stability," *Methods in Enzymology*, vol. 364, pp. 350-361, 2003.
- [56] Q. Liu, T. A. Rand, S. Kalidas, F. Du, H.-E. Kim, D. P. Smith, and X. Wang, "R2D2, a Bridge Between the Initiation and Effector Steps of the Drosophila RNAi Pathway," *Science*, vol. 301, pp. 1921-1925, 2003.
- [57] M. Fried and D. M. Crothers, "Equilibria and kinetics of lac repressor-operator interactions by polyacrylamide gel electrophoresis," *Nucleic Acids Res.*, vol. 9, pp. 6505-6525, 1981.
- [58] M. M. Garner and A. Revzin, "A gel electrophoresis method for quantifying the binding of proteins to specific DNA regions: application to components of the Escherichia coli lactose operon regulatory system," *Nucleic Acids Res.*, vol. 9, pp. 3047-3060, 1981.
- [59] Y. Liu, F. Wu, and G. Zou, "Electrophoresis mobility shift assay and biosensor used in studying the interaction between bleomycin A5 and DNA," *Anal. Chim. Acta*, vol. 599, pp. 310-314, 2007.
- [60] H. Schägger and G. v. Jagow, "Tricine-sodium dodecyl sulfate-polyacrylamide gel electrophoresis for the separation of proteins in the range from 1 to 100 kDa," *Analytical Biochemistry*, vol. 166, pp. 368-379, 1987.
- [61] J. D. Taylor, A. J. Ackroyd, and S. E. Halford, "The Gel Shift Assay for the Analysis of DNA-Protein Interactions," in *DNA-protein interactions: principles and protocols*, vol. 30, G. G. Kneale, Ed. Totowa, NJ: Humana Press Inc., 1994, pp. 263.
- [62] H. M. Shapiro, *Practical Flow Cytometry*. Hoboken, NJ: John Wiley & Sons, Inc., 2003.
- [63] D. W. Hedley, M. L. Friedlander, I. W. Taylor, C. A. Rugg, and E. A. Musgrove, "Method for Analysis of Cellular DNA Content of Paraffin-

- embedded Pathological Material Using Flow Cytometry," *The Journal of Histochemistry and Cytochemistry*, vol. 31, pp. 1333-1335, 1983.
- [64] B. L. Marrone, "Flow Cytometry: A Multipurpose Technology for a Wide Spectrum of Global Biosecurity Applications," *Journal of Laboratory Automation*, vol. 14, pp. 148-156, 2009.
- [65] N. F. Bence, R. M. Sampat, and R. R. Kopito, "Impairment of the Ubiquitin-Proteasome System by Protein Aggregation," *Science*, vol. 292, pp. 1552-1555, 2001.
- [66] P. O. Krutzik and G. P. Nolan, "Intracellular Phospho-protein Staining Techniques for Flow Cytometry: Monitoring Single Cell Signaling Events," *Cytometry Part A*, vol. 55A, pp. 61-70, 2003.
- [67] D. L. Roman, J. N. Talbot, R. A. Roof, R. K. Sunahara, J. R. Traynor, and R. R. Neubig, "Identification of Small-Molecule Inhibitors of RGS4 Using a High-Throughput Flow Cytometry Protein Interaction Assay," *Mol. Pharmacol.*, vol. 71, pp. 169-175, 2007.
- [68] R. I. Amann, B. J. Binder, R. J. Olson, S. W. Chisholm, R. Devereux, and D. A. Stahl, "Combination of 16S rRNA-Targeted Oligonucleotide Probes with Flow Cytometry for Analyzing Mixed Microbial Populations," *Applied and Environmental Microbiology*, vol. 56, pp. 1919-1925, 1990.
- [69] M. Díaz, M. Herrero, L. A. García, and C. Quirós, "Application of flow cytometry to industrial microbial bioprocesses," *Biochemical Engineering Journal*, vol. 48, pp. 385-407, 2010.
- [70] C. Sakamoto, N. Yamaguchi, M. Yamada, H. Nagase, M. Seki, and M. Nasu, "Rapid quantification of bacterial cells in potable water using a simplified microfluidic device," *Journal of Microbiological Methods*, vol. 68, pp. 643-647, 2007.
- [71] S. Joo, K. H. Kim, H. C. Kim, and T. D. Chung, "A portable microfluidic flow cytometer based on simultaneous detection of impedance and fluorescence," *Biosens. Bioelectron.*, vol. 25, pp. 1509-1515, 2010.
- [72] S. Jakobs, M. Andresen, and C. A. Wurm, "FlAsH Protein Labeling," in *Probes and Tags to Study Biomolecular Function: for Proteins, RNA, and Membranes*, L. W. Miller, Ed.: Wiley-VCH, 2008.
- [73] S. Balslev, et al., "Lab-on-a-chip with integrated optical transducers," *Lab Chip*, vol. 6, pp. 213-217, 2006.
- [74] M. C. Y. Huang, C. F. R. Mateus, J. E. Foley, R. Beatty, B. T. Cunningham, and C. J. Chang-Hasnain, "VCSEL Optoelectronic Biosensor for Detection of Infectious Diseases," *IEEE Photonics Technology Letters*, vol. 20, pp. 443-445, 2008.
- [75] O. Schmidt, M. Bassler, P. Kiesel, C. Knollenberg, and N. Johnson, "Fluorescence spectrometer-on-a-fluidic-chip," *Lab Chip*, vol. 7, pp. 626-629, 2007.
- [76] P. Dykstra, J. Hao, S. T. Koev, G. F. Payne, L. Yu, and R. Ghodssi, "An optical MEMS sensor utilizing a chitosan film for catechol detection," *Sensor. Actuat. B-Chem.*, vol. 138, pp. 64-70, 2009.

- [77] L. Jiang and S. Pau, "Integrated waveguide with a microfluidic channel in spiral geometry for spectroscopic applications," *Applied Physics Letters*, vol. 90, pp. 111108, 2007.
- [78] C. Liu, "Recent Developments in Polymer MEMS," *Advanced Materials*, vol. 19, pp. 3783-3790, 2007.
- [79] Z. Wang, A. Sekulovic, J. P. Kutter, D. D. Bang, and A. Wolff, "Towards a portable microchip system with integrated thermal control and polymer waveguides for real-time PCR," *Electrophoresis*, vol. 27, pp. 5051-5058, 2006.
- [80] M.-H. Wu, H. Cai, X. Xu, J. P. G. Urban, Z.-F. Cui, and Z. Cui, "A SU-8/PDMS Hybrid Microfluidic Device with Integrated Optical Fibers for Online Monitoring of Lactate," *Biomed. Microdevices*, vol. 7, pp. 323-329, 2005.
- [81] K.-H. Lee, Y.-D. Sua, S.-J. Chena, F.-G. Tseng, and G.-B. Lee, "Microfluidic systems integrated with two-dimensional surface plasmon resonance phase imaging systems for microarray immunoassay," *Biosens. Bioelectron.*, vol. 23, pp. 466-472, 2007.
- [82] S. T. Koev, et al., "Mechano-transduction of DNA hybridization and dopamine oxidation through electrodeposited chitosan network," *Lab Chip*, vol. 7, pp. 103-111, 2007.
- [83] N. Siwak, X. Z. Fan, D. Hines, S. Kanakaraju, N. Goldsman, and R. Ghodssi, "Indium Phosphide MEMS Cantilever Resonator Sensors Utilizing a Pentacene Absorption Layer," *Journal of Microelectromechanical Systems*, vol. 18, pp. 103-110, 2009.
- [84] S. T. Koev, W. E. Bentley, and R. Ghodssi, "Interferometric readout of multiple cantilever sensors in liquid samples," *Sensor. Actuat. B-Chem.*, vol. B146, pp. 245-252, 2010.
- [85] S. T. Koev, R. Fernandes, W. E. Bentley, and R. Ghodssi, "A Cantilever Sensor With an Integrated Optical Readout for Detection of Enzymatically Produced Homocysteine," *IEEE Transactions on Biomedical Circuits and Systems*, vol. 3, pp. 415-423, 2009.
- [86] H.-S. Kwon, K.-C. Han, K. S. Hwang, J. H. Lee, T. S. Kim, D. S. Yoon, and E. G. Yang, "Development of a peptide inhibitor-based cantilever sensor assay for cyclic adenosine monophosphate-dependent protein kinase," *Anal. Chim. Acta*, vol. 585, pp. 344-349, 2007.
- [87] F.-F. Chou and J.-S. Shih, "Electrochemical electrode/SAW system for metal ions and glucose in solutions," *Sensor. Actuat. B-Chem.*, vol. 129, pp. 176-183, 2008.
- [88] S. Krishnamoorthy, A. Iliadis, T. Bei, and G. P. Chrousos, "An interleukin-6 ZnO/SiO₂/Si surface acoustic wave biosensor," *Biosens. Bioelectron.*, vol. 24, pp. 313-318, 2008.
- [89] K. Länge, G. Blaess, A. Voigt, R. Götzen, and M. Rapp, "Integration of a surface acoustic wave biosensor in a microfluidic polymer chip," *Biosens. Bioelectron.*, vol. 22, pp. 227-232, 2006.

- [90] H. Cai, T. M.-H. Lee, and I.-M. Hsing, "Label-free protein recognition using an aptamer-based impedance measurement assay," *Sensor. Actuat. B-Chem.*, vol. 114, pp. 433-437, 2006.
- [91] R. Gomez, et al., "Microfluidic biochip for impedance spectroscopy of biological species," *Biomed. Microdevices*, vol. 3, pp. 201-209, 2001.
- [92] C. Iliescu, D. P. Poenar, M. Carp, and F. C. Loe, "A microfluidic device for impedance spectroscopy analysis of biological samples," *Sensor. Actuat. B-Chem.*, vol. 123, pp. 168-176, 2007.
- [93] S. B. Prakash and P. Abshire, "Tracking cancer cell proliferation on a CMOS capacitance sensor chip," *Biosens. Bioelectron.*, vol. 23, pp. 1449-1457, 2008.
- [94] A. Qureshi, Y. Gurbuz, S. Kallempudi, and J. H. Niazi, "Label-free RNA aptamer-based capacitive biosensor for the detection of C-reactive protein," *Phys. Chem. Chem. Phys.*, vol. 12, pp. 9176-9182, 2010.
- [95] A. Qureshi, J. H. Niazi, S. Kallempudi, and Y. Gurbuz, "Label-free capacitive biosensor for sensitive detection of multiple biomarkers using gold interdigitated capacitor arrays," *Biosens. Bioelectron.*, vol. 25, pp. 2318-2323, 2010.
- [96] N. Hu, "Direct electrochemistry of redox proteins or enzymes at various film electrodes and their possible applications in monitoring some pollutants," *Pure Applied Chemistry*, vol. 73, pp. 1979-1991, 2001.
- [97] T. Matsumoto, S. Saito, and S. Ikeda, "A multilayer membrane amperometric glucose sensor fabricated using planar techniques for large-scale production," *J. Biotechnol.*, vol. 122, pp. 267-273, 2006.
- [98] A. Yamaguchi, P. Jin, H. Tsuchiyama, T. Masuda, K. Sun, S. Matsuo, and H. Misawa, "Rapid fabrication of electrochemical enzyme sensor chip using polydimethylsiloxane microfluidic channel," *Anal. Chim. Acta*, vol. 468, pp. 143-152, 2002.
- [99] N. Nashida, W. Satoh, J. Fukuda, and H. Suzuki, "Electrochemical immunoassay on a microfluidic device with sequential injection and flushing functions," *Biosens. Bioelectron.*, vol. 22, pp. 3167-3173, 2007.
- [100] O. Frey, S. Talaei, P. D. v. d. Wal, M. Koudelka-Hep, and N. F. d. Rooij, "Continuous-flow multi-analyte biosensor cartridge with controllable linear response range," *Lab Chip*, vol. 10, pp. 2226-2234, 2010.
- [101] Y. Mao, W. Wei, H. Peng, and J. Zhang, "Monitoring for adsorption of human serum albumin and bovine serum albumin onto bare and polystyrene-modified silver electrodes by quartz crystal impedance analysis," *J. Biotechnol.*, vol. 89, pp. 1-10, 2001.
- [102] B. Menz, R. Knerr, A. Göpferich, and C. Steinem, "Impedance and QCM analysis of the protein resistance of self-assembled PEGylated alkanethiol layers on gold," *Biomaterials*, vol. 26, pp. 4237-4243, 2005.
- [103] H. Ogi, Y. Fukunishi, H. Nagai, K. Okamoto, M. Hirao, and M. Nishiyama, "Nonspecific-adsorption behavior of polyethylenglycol and bovine serum albumin studied by 55-MHz wireless-electrodeless quartz crystal microbalance," *Biosens. Bioelectron.*, vol. 24, pp. 3148-3152, 2009.

- [104] N. Saito and T. Matsuda, "Protein adsorption on self-assembled monolayers with water-soluble non-ionic oligomers using quartz-crystal microbalance," *Mat. Sci. Eng. C*, vol. 6, pp. 261-266, 1998.
- [105] T. T. Doan, M. L. Vargo, J. K. Gerig, C. P. Gulka, M. L. Trawick, J. D. Dattelbaum, and M. C. Leopold, "Electrochemical analysis of azurin thermodynamic and adsorption properties at monolayer-protected cluster film assemblies – Evidence for a more homogeneous adsorption interface," *J. Colloid Interf. Sci.*, vol. 352, pp. 50-58, 2010.
- [106] J. Hedlund, A. Lundgren, B. Lundgren, and H. Elwing, "A new compact electrochemical method for analyzing complex protein films adsorbed on the surface of modified interdigitated gold electrodes," *Sensor. Actuat. B-Chem.*, vol. 142, pp. 494-501, 2009.
- [107] Q. Xie, Y. Zhang, M. Xu, Z. Li, Y. Yuan, and S. Yao, "Combined quartz crystal impedance and electrochemical impedance measurements during adsorption of bovine serum albumin onto bare and cysteine- or thiophenol-modified gold electrodes," *J. Electroanal. Chem.*, vol. 478, pp. 1-8, 1999.
- [108] M. Farrell and S. Beaudoin, "Surface forces and protein adsorption on dextran- and polyethylene glycol-modified polydimethylsiloxane," *Colloid. Surface. B*, vol. 81, pp. 468-475, 2010.
- [109] C. Ma, Y. Hou, S. Liu, and G. Zhang, "Effect of Microphase Separation on the Protein Resistance of a Polymeric Surface," *Langmuir*, vol. 25, pp. 9467-9472, 2009.
- [110] M. Mrksich and G. M. Whitesides, "Using self-assembled monolayers to understand the interactions of man-made surfaces with proteins and cells," *Annu. Rev. Bioph. Biom.*, vol. 25, pp. 55-78, 1996.
- [111] E. Ostuni, L. Yan, and G. M. Whitesides, "The interaction of proteins and cells with self-assembled monolayers of alkanethiolates on gold and silver," *Colloid. Surface. B*, vol. 15, pp. 3-30, 1999.
- [112] K. E. Sapsford and F. S. Ligler, "Real-time analysis of protein adsorption to a variety of thin films," *Biosens. Bioelectron.*, vol. 19, pp. 1045-1055, 2004.
- [113] C. Gautier, C. Esnault, C. Cougnon, J.-F. Pilard, N. Casse, and B. Chenais, "Hybridization-induced interfacial changes detected by non-Faradaic impedimetric measurements compared to Faradaic approach," *J. Electroanal. Chem.*, vol. 610, pp. 227-233, 2007.
- [114] D. Li, X. Zou, Q. Shen, and S. Dong, "Kinetic study of DNA/DNA hybridization with electrochemical impedance spectroscopy," *Electrochem. Commun.*, vol. 9, pp. 191-196, 2007.
- [115] Y. Ma, K. Jiao, T. Yang, and D. Sun, "Sensitive PAT gene sequence detection by nano-SiO₂/p-aminothiophenol self-assembled films DNA electrochemical biosensor based on impedance measurement," *Sensor. Actuat. B-Chem.*, vol. 131, pp. 565-571, 2008.
- [116] G. D. McEwen, F. Chen, and A. Zhou, "Immobilization, hybridization, and oxidation of synthetic DNA on gold surface: Electron transfer investigated by electrochemistry and scanning tunneling microscopy," *Anal. Chim. Acta*, vol. 643, pp. 26-37, 2009.

- [117] J. J. Sumner, K. W. Plaxico, C. D. Meinhart, and H. Soh, "Development of an electrochemical biosensor without a sandwich assay," presented at SPIE, 2005.
- [118] D. Erickson, D. Li, and U. J. Krull, "Modeling of DNA hybridization kinetics for spatially resolved biochips," *Analytical Biochemistry*, vol. 317, pp. 186-200, 2003.
- [119] J. H.-S. Kim, A. Marafie, X.-Y. Jia, J. V. Zoval, and M. J. Madou, "Characterization of DNA hybridization kinetics in a microfluidic flow channel," *Sensor. Actuat. B-Chem.*, vol. 113, pp. 281-289, 2006.
- [120] L. M. Shamansky, C. B. Davis, J. K. Stuart, and W. G. Kuhr, "Immobilization and detection of DNA on microfluidic chips," *Talanta*, vol. 55, pp. 909-918, 2001.
- [121] V. R. Dukkipati and S. W. Pang, "Integrated Microfluidic System for DNA Analysis," presented at Nanotechnology, Cincinnati, OH, July 17-20, 2006.
- [122] T. H. Fang, et al., "Real-time PCR microfluidic devices with concurrent electrochemical detection," *Biosens. Bioelectron.*, vol. 24, pp. 2131-2136, 2009.
- [123] X. Xu, S. Zhang, H. Chen, and J. Kong, "Integration of electrochemistry in micro-total analysis systems for biochemical assays: Recent developments," *Talanta*, vol. 80, pp. 8-18, 2009.
- [124] V. N. Goral, N. V. Zaytseva, and A. J. Baeumner, "Electrochemical microfluidic biosensor for the detection of nucleic acid sequences," *Lab Chip*, vol. 6, pp. 414-421, 2006.
- [125] S. H. Lee and E. Ruckenstein, "Adsorption of proteins onto polymeric surfaces of different hydrophilicities—a case study with bovine serum albumin," *J. Colloid Interf. Sci.*, vol. 125, pp. 365-379, 1988.
- [126] J. S. Ko, H. C. Yoon, H. Yang, H.-B. Pyo, K. H. Chung, S. J. Kim, and Y. T. Kim, "A polymer-based microfluidic device for immunosensing biochips," *Lab Chip*, vol. 3, pp. 106-113, 2003.
- [127] J. Schwarz, H. Kaden, and U. Enseleit, "Voltammetric examinations of ferrocene on microelectrodes and microarrayelectrodes," *Electrochem. Commun.*, vol. 2, pp. 606-611, 2000.
- [128] M. K. Patel, P. R. Solanki, A. Kumar, S. Khare, S. Gupta, and B. D. Malhotra, "Electrochemical DNA sensor for *Neisseria meningitidis* detection," *Biosens. Bioelectron.*, vol. 25, pp. 2586-2591, 2010.
- [129] N. Zhou, T. Yang, C. Jiang, M. Du, and K. Jiao, "Highly sensitive electrochemical impedance spectroscopic detection of DNA hybridization based on Aunano-CNT/PANnano films," *Talanta*, vol. 77, pp. 1021-1026, 2009.
- [130] X. He, R. Yuan, Y. Chai, and Y. Shi, "A sensitive amperometric immunosensor for carcinoembryonic antigen detection with porous nanogold film and nano-Au/chitosan composite as immobilization matrix," *J. Biochem. Bioph. Meth.*, vol. 70, pp. 823-829, 2008.
- [131] J. P. Carr, N. A. Hampson, and R. Taylor, "A study of the electrical double layer at PbO₂ in aqueous KNO₃ electrolyte," *J. Electroanal. Chem.*, vol. 27, pp. 109-116, 1970.

- [132] P. T. Kissinger and W. R. Helneman, "Cyclic Voltammetry," *Journal of Chemical Education*, vol. 60, pp. 702-706, 1983.
- [133] A. Kueng, C. Kranz, and B. Miaikoff, "Imaging of ATP membrane transport with dual micro-disk electrodes and scanning electrochemical microscopy," *Biosens. Bioelectron.*, vol. 21, pp. 346-353, 2005.
- [134] D. Xu, D. Xu, X. Yu, Z. Liu, W. He, and Z. Ma, "Label-Free electrochemical detection for aptamer-based array electrodes," *Analytical Chemistry*, vol. 77, pp. 5107-5113, 2005.
- [135] P. M. S. Monk, *Fundamentals of Electroanalytical Chemistry*. Chichester: John Wiley & Sons LTD, 2001.
- [136] D. K. Gosser, *Cyclic voltammetry: Simulation and analysis of reaction mechanisms*. New York: John Wiley & Sons Inc., 1993.
- [137] F. Patolsky, M. Zayats, E. Katz, and I. Willner, "Precipitation of an insoluble product on enzyme monolayer electrodes for biosensor applications: Characterization by faradaic impedance spectroscopy, cyclic voltammetry, and microgravimetric quartz crystal microbalance analyses," *Analytical Chemistry*, vol. 71, pp. 3171-3180, 1999.
- [138] O. Fontaine, G. Trippe, C. Fave, J.-C. Lacroix, and H. N. Randriamahazaka, "Microstructured electroactive surface based on binary self-assembled monolayer," *J. Electroanal. Chem.*, vol. 632, pp. 1-7, 2009.
- [139] F. Ricci, R. Y. Lai, A. J. Heeger, K. W. Plaxico, and J. J. Sumner, "Effect of molecular crowding on the response of an electrochemical DNA sensor," *Langmuir*, vol. 23, pp. 6827-6834, 2007.
- [140] Y. Song, Y. Liu, M. Yang, B. Zhang, and Z. Li, "Diluting thiol-derivatized oligonucleotide monolayers on Au(1 1 1) by mercaptohexanol replacement reaction," *Applied Surface Science*, vol. 252, pp. 5693-5699, 2006.
- [141] R. Popovtzer, T. Neufeld, E. z. Ron, J. Rishpon, and Y. Shacham-Diamand, "Electrochemical detection of biological reactions using a novel nano-bio-chip array," *Sensor. Actuat. B-Chem.*, vol. 119, pp. 664-672, 2006.
- [142] V. Studer, G. Hang, A. Pandolfi, M. Ortiz, W. F. Anderson, and S. R. Quake, "Scaling properties of a low-actuation pressure microfluidic valve," *Journal of Applied Physics*, vol. 95, pp. 393-398, 2004.
- [143] M. A. Unger, H.-P. Chou, T. Thorsen, A. Scherer, and S. R. Quake, "Monolithic microfabricated valves and pumps by multilayer soft lithography," *Science*, vol. 288, pp. 113-116, 2000.
- [144] C.-H. Wang and G.-B. Lee, "Automatic bio-sampling chips integrated with micro-pumps and micro-valves for disease detection," *Biosens. Bioelectron.*, vol. 21, pp. 419-425, 2005.
- [145] S. Bhattacharya, Y. Gao, V. Korampally, M. T. Othman, S. A. Grant, K. Gangopadhyay, and S. Gangopadhyay, "Mechanics of plasma exposed spin-on-glass (SOG) and polydimethylsiloxane (PDMS) surfaces and their impact on bond strength," *Applied Surface Science*, vol. 253, pp. 4220-4225, 2007.
- [146] L. H. He, C. W. Lim, and B. S. Wu, "A continuum model for size-dependent deformation of elastic films of nano-scale thickness," *International Journal of Solids and Structures*, vol. 41, pp. 847-857, 2004.

- [147] J. Marquez-Velasco, M.-E. Vlachopoulou, A. Tserepi, and E. Gogolides, "Stable superhydrophobic surfaces induced by dual-scale topography on SU-8," *Microelectronic Engineering*, vol. 87, pp. 782-785, 2010.
- [148] H.-Y. Wang, N. Bao, and C. Lu, "A microfluidic cell array with individually addressable culture chambers," *Biosens. Bioelectron.*, vol. 24, pp. 613-617, 2008.
- [149] C. L. Gilleland, C. B. Rohde, F. Zeng, and M. F. Yanik, "Microfluidic immobilization of physiologically active *Caenorhabditis elegans*," *Nature Protocols*, vol. 5, pp. 1888-1902, 2010.
- [150] S. Satyanarayana, R. N. Karnik, and A. Majumdar, "Stamp-and-Stick Room-Temperature Bonding Technique for Microdevices," *Journal of Microelectromechanical Systems*, vol. 14, pp. 392-399, 2005.
- [151] K.-S. Yun and E. Yoon, "Fabrication of complex multilevel microchannels in PDMS by using threedimensional photoresist masters," *Lab Chip*, vol. 8, pp. 245-250, 2008.
- [152] B.-H. Jo, L. M. VanLerberghe, K. M. Motsegood, and D. J. Beebe, "Three-dimensional micro-channel fabrication in polydimethylsiloxane (PDMS) elastomer," *Journal of Microelectromechanical Systems*, vol. 9, pp. 76-81, 2000.
- [153] S. J. Konopka and B. McDuffie, "Diffusion Coefficients of Ferri- and Ferrocyanide Ions in Aqueous Media, Using Twin-Electrode Thin-layer Electrochemistry," *Anal. Chem.*, vol. 42, pp. 1741-1746, 1970.
- [154] P. G. Gross, E. P. Kartalov, A. Scherer, and L. P. Weiner, "Applications of microfluidics for neuronal studies," *Journal of Neurological Sciences*, vol. 252, pp. 135-143, 2007.
- [155] K. Ziolkowska, E. Jedrych, R. Kwapiszewski, J. Lopacinska, M. Skolimowski, and M. Chudy, "PDMS/glass microfluidic cell culture system for cytotoxicity tests and cells passage," *Sensor. Actuat. B-Chem.*, vol. 145, pp. 533-542, 2010.
- [156] K. L. Prime and G. M. Whitesides, "Adsorption of Proteins onto Surfaces Containing End-Attached Oligo(ethylene oxide): A Model System Using Self-Assembled Monolayers," *Journal of American Chemical Society*, vol. 115, pp. 10714-10721, 1993.
- [157] B. D. Ratner, A. S. Hoffmann, F. J. Schoen, and J. E. Lemons, *Biomaterials Science. An Introduction to Materials in Medicine*. New York: Academic Press, 1996.
- [158] M. Alkan, Ö. Demirbaş, M. Doğan, and O. Arslan, "Surface properties of bovine serum albumin – adsorbed oxides: Adsorption, adsorption kinetics and electrokinetic properties," *Micropor. Mesopor. Mat.*, vol. 96, pp. 331-340, 2006.
- [159] M. E. Price, R. M. Cornelius, and J. L. Brash, "Protein adsorption to polyethylene glycol modified liposomes from fibrinogen solution and from plasma," *Biochim. Biophys. Acta*, vol. 1512, pp. 191-205, 2001.
- [160] E. A. Scott, M. D. Nichols, L. H. Cordova, B. J. George, Y.-S. Jun, and D. L. Elbert, "Protein adsorption and cell adhesion on nanoscale bioactive coatings

- formed from poly(ethylene glycol) and albumin microgels," *Biomaterials*, vol. 29, pp. 4481-4493, 2008.
- [161] L. Yang, "Dielectrophoresis assisted immuno-capture and detection of foodborne pathogenic bacteria in biochips," *Talanta*, vol. 80, pp. 551-558, 2009.
- [162] Z. Dai, S. Serban, H. Ju, and N. E. Murr, "Layer-by-layer hydroxymethyl ferrocene modified sensor for one-step flow/stop-flow injection amperometric immunoassay of α -fetoprotein," *Biosens. Bioelectron.*, vol. 22, pp. 1700-1706, 2007.
- [163] Z. Yang, J. A. Galloway, and H. Yu, "Protein Interactions with Poly(ethylene glycol) Self-Assembled Monolayers on Glass Substrates: Diffusion and Adsorption," *Langmuir*, vol. 15, pp. 8405-8411, 1999.
- [164] J. S. Krakow and I. Pastan, "Cyclic Adenosine Monophosphate Receptor: Loss of cAMP-Dependent DNA Binding Activity after Proteolysis in the Presence of Cyclic Adenosine Monophosphate," *P. Natl. Acad. Sci. USA*, vol. 70, pp. 2529-2533, 1973.
- [165] R. J. Meagher, A. V. Hatch, R. F. Renzi, and A. K. Singh, "An integrated microfluidic platform for sensitive and rapid detection of biological toxins," *Lab Chip*, vol. 8, pp. 2046-2053, 2008.
- [166] B. Aggarwal and S. Reddy, *Guidebook to Cytokines and Their Receptors*. New York: Oxford University Press, 1994.
- [167] Y. Xiao, A. A. Lubin, B. R. Baker, K. W. Plaxico, and A. J. Heeger, "Single-step electronic detection of femtomolar DNA by target-induced strand displacement in an electrode-bound duplex," *PNAS*, vol. 103, pp. 16677-16680, 2006.
- [168] K. Arinaga, U. Rant, M. Tornow, S. Fujita, G. Abstreiter, and N. Yokoyama, "The Role of Surface Charging during the Coadsorption of Mercaptohexanol to DNA Layers on Gold: Direct Observation of Desorption and Layer Reorientation," *Langmuir*, vol. 22, pp. 5560-5562, 2006.
- [169] J. J. Gooding, A. Chou, F. J. Mearns, E. L.-S. Wong, and K. L. Jericho, "The ion gating effect: using a change in flexibility to allow label free electrochemical detection of DNA hybridisation," *Chem. Comm.*, pp. 1938-1939, 2003.
- [170] S. Pan and L. Rothberg, "Chemical Control of Electrode Functionalization for Detection of DNA Hybridization by Electrochemical Impedance Spectroscopy," *Langmuir*, vol. 21, pp. 1022-1027, 2005.
- [171] R. Lenigk, H. Zhu, T.-C. Lo, and R. Renneberg, "Recessed microelectrode array for a micro flow-through system allowing on-line multianalyte determination in vivo," *Journal of Analytical Chemistry*, vol. 364, pp. 66-71, 1999.
- [172] H. J. Lee, C. Beriet, R. Ferrigno, and H. H. Girault, "Cyclic voltammetry at a regular microdisc electrode array," *J. Electroanal. Chem.*, vol. 502, pp. 138-145, 2001.
- [173] S. T. Koev, P. H. Dykstra, X. Luo, G. W. Rubloff, W. E. Bentley, G. F. Payne, and R. Ghodssi, "Chitosan: an integrative biomaterial for lab-on-a-chip devices," *Lab Chip*, vol. 10, pp. 3026-3040, 2010.

- [174] X. Luo, A. T. Lewandowski, H. Yi, G. F. Payne, R. Ghodssi, W. E. Bentley, and G. W. Rubloff, "Programmable assembly of a metabolic pathway enzyme in a pre-packaged reusable bioMEMS device," *Lab Chip*, vol. 8, pp. 420-430, 2008.
- [175] H. Yi, L.-Q. Wu, W. E. Bentley, R. Ghodssi, G. W. Rubloff, J. N. Culver, and G. F. Payne, "Biofabrication with Chitosan," *Biomacromolecules*, vol. 6, pp. 2881-2894, 2005.
- [176] H. Chang and J. Li, "Electrochemical impedance probing of transcriptional TATA binding protein based on TATA box site-specific binding," *Electrochem. Commun.*, vol. 11, pp. 2101-2104, 2009.
- [177] R. Meunier-Prest, A. Bouyon, E. Rampazzi, S. Raveau, P. Andreoletti, and M. Cherkaoui-Malki, "Electrochemical probe for the monitoring of DNA-protein interactions," *Biosens. Bioelectron.*, vol. 25, pp. 2598-2602, 2010.
- [178] K. Dill, D. D. Montgomery, A. L. Ghindilis, K. R. Schwarzkopf, S. R. Ragsdale, and A. V. Oleinikov, "Immunoassays based on electrochemical detection using microelectrode arrays," *Biosens. Bioelectron.*, vol. 20, pp. 736-742, 2004.
- [179] J. A. D. Wattis, "Nonlinear breathing modes due to a defect in a DNA chain," *Phil. Trans. R. Soc. Lond. A*, vol. 362, pp. 1461-1477, 2004.
- [180] T. Ambjörnsson, S. K. Banik, O. Krichevsky, and R. Metzler, "Breathing Dynamics in heteropolymer DNA," *Biophys. J.*, vol. 92, pp. 2674-2684, 2007.